Hörler Bianca, BSc

CHARACTERIZATION of METALLIC MULTILAYER STRUCTURES

MASTER´S THESIS

to achieve the university degree of

Diplom Ingenieurin

Technical Chemistry

submitted at

University of Technology Graz

Supervisor

Ao. Univ.- Prof. Dipl.- Ing. Dr. Tech Klaus Reichmann

Institute for Chemistry and Technology of Materials

University of Technology

Ing. Hartmuth Schröttner

Graz, December 2018

Statutory Declaration

I declare that I have authored this thesis independently, that I have not used other than the declared sources / resources, and that I have explicitly marked all material which has been quoted either literally or by content from the used sources.

_____	_____	_____
Place	Date	Signature

1 Abstract

A specially developed measurement method for the characterization and quantification of *sputtered metallic single- and multi-layer systems* is described. Therefore, the sputtered substrates were prepared by two conventional polishing methods and broad ion beam milling. The investigations were performed with *scanning electron microscopy* in combination with *energy dispersive* X-ray *spectroscopy*. The quantitative analysis of the untreated surface of the single layers (components of the multi-layer system) shows partially deviations from the AAS reference values. Large amounts of lead in the metal alloy films are responsible for absorption of electrons and geometry effects, which cause systematic errors. The results of the single- and multi-layer systems in polished cross-section deviate less from the reference but lead still causes problems. However, SEM-EDS is an appropriate characterization method for single and graduated metallic layer systems, if the layer preparation is optimized and correction modes are applied.

2 Content

3 Introduction

Various components of engines are coated with thin films deposited with magnetron sputtering to improve the properties and the performance of the base material, such as steel. In this study a graduated layer system consisting of four different alloy films (CuPb23Sn3, CuPb27, CuSn6 and Cu9Pb) on a steel substrate is investigated. Since an accurate composition of the single layers within the multi-layer system is required to achieve certain surface properties, a suitable quantitative chemical characterization method is necessary. It should be possible to monitor the average composition of the layers in series production to maintain a constant quality of the multi-layer system. Scanning electron microscopy in combination with energy dispersive X-ray spectroscopy was chosen as a characterization method and several layer preparation methods was evaluated.

First, the untreated surface and the polished cross-section of each single layer of the graduated layer system on the steel substrate was studied and quantified to assess the accuracy of the method by comparing the results with reference values from AAS analysis.

To investigate the multi-layer system large areas within each layer were scanned and analyzed with SEM-EDS to primarily determine the average composition of each film. In this context also the problematic of diffusion between the layers within the multi-layer structure and the adjustment of the sputter equilibrium after the start of the coating was investigated. Therefore, several horizontal line spectra at a certain distance between the CuSn6 and CuPb23Sn3 film were recorded and analyzed.

Additional to the conventional polishing preparation method, a steel substrate with a CuPb25 film was prepared with the broad-ion-beam method to illustrate the problems and difficulties of layer preparation.

4 Theoretical Background

4.1 Surface Engineering

According to Donald M. Mattox **[1]** surface engineering deals with the change of a surface or near-surface region and, hence, the properties of the material. This involves either a coating process, where the surface itself is modified. In an overlay process the surface of a substrate is completely covered with a desired material by various process methods. A surface modification process changes the properties of the substrate surface without adding any additional materials, so the components present in the substrate remain still in place on the surface.

The modification of surfaces can be performed prior to a film deposition or a coating process, e. g. by hardening steel with plasma nitriding before the deposition of a material which is harder than the untreated steel by physical vapor deposition. Furthermore, the surface modification process can be used to modify the properties of the overlay. For example, the density of a sputtered coating on an aircraft turbine blade improved by shot peening and compression.

In an overlay process (atomistic deposition process) the desired material is deposited atom by atom. The film can vary in its properties from single crystal to amorphous, high density to low density and pure to impure. The deposited layers can range from thin film, which usually means a thickness of less than one micrometer to thicker layers of thousand nanometers.

In general, the properties of thin films depend on the underlying substrate and vary with the thickness of the layer. The overlay process (atomistic deposition) can be performed in vacuum, plasma, gaseous or electrolytic environment.

4.2 Physical Vapor Deposition Processing

In physical vapor deposition processes materials are vaporized from a solid or liquid target in the form of molecules or atoms and then transported through low pressure, plasma or vacuum to the substrate to be coated, where it condenses.

Physical vapor deposition, which is also known as thin film processes, is used for the deposition of films with the thickness between a few nanometers and thousands of nanometers. This process is also used for the formation of multi-layer coatings, very thick depositions, graduated compositions layers and freestanding structures. The substrate to be coated can vary in size from very small parts to very large glass panels of about 10 m^2 for example. Also the shape can range from flat (metal plates, slices or glass panels) to very complex objects (watchbands). Per second about 1 to 10 nm can be deposited by using PVD depositions processing.

The process is used to deposit films of different thickness made of elements and alloys. However, it is also used to produce compounds using reactive deposition processes. This means that the compounds are generated by the reaction between the deposition material and the gas environment such as nitrogen to form for example TiN or with co-depositing material to form TiC.

Quasi-reactive deposition means the deposition of a compound material from a compound source. In this deposition process a loss of the more volatile species or less reactive species during the transport and condensation process occurs. This loss is compensated by having a partial pressure of reactive gas in the deposition environment. The deposition of indium-tin oxide from an ITO sputtering target supplying the proper partial pressure of oxygen in the plasma environment is an example for quasi-reactive deposition.

There are four main classes of PVD processing vacuum deposition (evaporation), sputter deposition, arc vapor deposition and ion plating (Fig. 1).

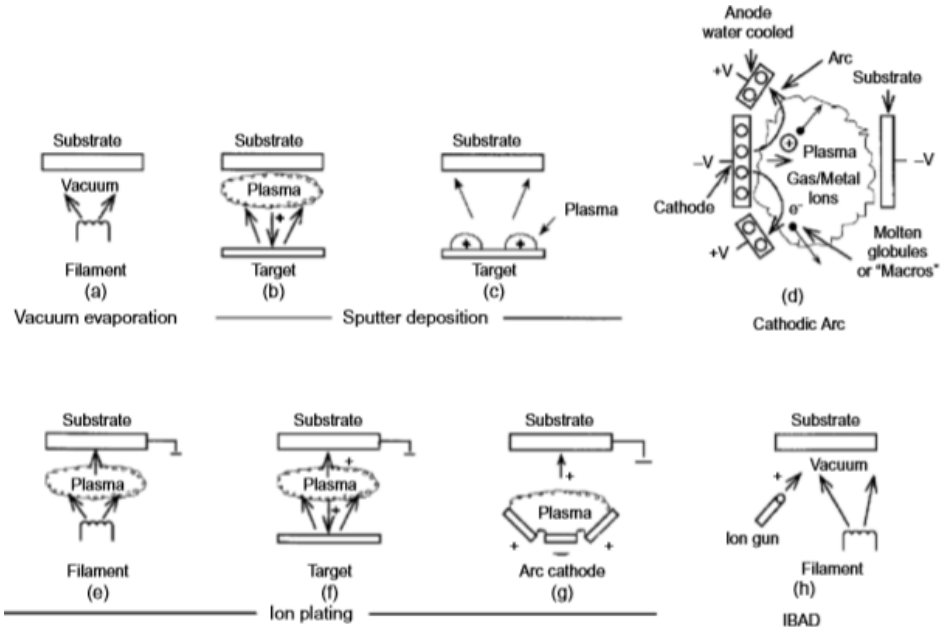

*Figure 1 – Physical vapor deposition techniques: a) Vacuum evaporation, b) and c) Sputter deposition in a plasma environment, d) Sputter deposition in a vacuum, e) Ion plating in a plasma environment with a thermal evaporation source, f) Ion plating with a sputtering source, g) Ion plating with an arc vaporization source and h) Ion beam-assisted deposition (IBaD) with thermal evaporations source and ion bombardment from an ion gun.**[1]***

4.2.1 Vacuum Deposition

In a vacuum deposition process the thermally vaporized material is transported with little or no collision with gas molecules to the substrate to be coated. Further benefit of vacuum environment is that the gas contamination in the deposition system can be minimized to a low amount. In general, the deposition occurs in the pressure range of 1.3^{-5} to 1.3^{-9} mbar. Depending on the pressure the level of gaseous contamination can be controlled, which means the lower the pressure the lower are the contaminants in the deposition system.

The thermal vaporization rate is very similar to other vaporization methods. The composition of the vaporized material from the target is proportional to the relative vapor pressures of the substances in the molten target material. Generally, the vaporization is done thermally by heated sources like tungsten wire coils or with high electron energy beam heating the target material itself. The substrates to be coated are placed at relatively large distance to minimize radiant heating of the substrate by the vaporized material.

Vacuum deposition is very versatile, and it is used to generate single and multilayers, optical interference coatings, mirror coatings, decorative coatings, electrically conducting films, wear resistant coating and corrosion protective coatings.

4.2.2 Arc Vapor Deposition

The principle of arc vapor deposition is to use a high current, low voltage arc to vaporize a cathode (cathodic arc) or an anode (anodic arc) and to deposit the evaporated source on the substrate. The highly

ionized vaporized material (film ions) is accelerated to the biased substrate surface. This method of PVD is used to generate decorative and hard coatings.

4.2.3 Ion Plating

Ion plating also known as ion-assisted deposition (IAD) or ion vapor deposition (IVD) uses atomic-sized energetic particles (ions) to alter and control the properties of deposition. Therefore, the depositing film is concurrently or periodically bombarded with those generated high energetic particles mentioned before. Important processing features are energy, flux and mass of the bombarding species along the ratio of bombarding particles to depositing particles. The vaporization of the material to be coated takes place by evaporation, sputtering, arc erosion or by decomposition of a chemical vapor precursor.

Generally, ions of inert gas or reactive gas are used for the bombardment. In some cases, ions of the condensing film material (film ions) are used. The ion plating process occurs either in plasma or in vacuum environment. In plasma the ions for bombardment are extracted from the plasma and in vacuum the ions form a separate "ion gun."

The ion beam-assisted deposition (IBAD) is the latter ion plating method and uses reactive gas in plasma to deposit films of composite materials. Relatively high gas pressure of ion plating yields in dense coatings, where gas scattering can improve the surface coverage.

Generally, this method of PVD is used to generate hard and dense coatings of compound material, optical coatings with high densities, adherent metal coatings and conformal coating on complex surfaces.

4.2.4 Sputter Deposition

In the sputter deposition process particles, which are vaporized from a target surface, are deposited on a substrate. Compared to other PVD processes it is a non- thermal vaporization process. This means that the surface atoms are physically ejected from a solid surface by the transfer of momentum from atomic-sized energetic bombarding particles. These are gaseous ions accelerated through the plasma current. The distance between target and substrate is short compared to the vacuum deposition mentioned above. A sputter layer arises when a solid surface (sputtering target) is bombarded with energetic ions in vacuum or low-pressure plasma environment (< 5 mTorr) using an ion gun. Thereby, a collision of sputtered particles with the gas phase between target and substrate can be minimized or even eliminated. However, sputter deposition can also be performed at higher pressure (5- 30 mTorr). In this case, the energetic particles sputtered or reflected from the target are thermalized by the collision in the gas phase before they arrive at the substrate surface to be coated.

The plasma used for the sputtering process can be constrained close to the target surface or fills the space between the source and the substrate. The target can be an element, alloy, mixture or a compound and the material is vaporized with the bulk composition of the source. The sputtering target supplies vaporization source for a long time that can be in any direction, where vaporization is required.

Composite materials like TiN and ZrN are generated by using a reactive gas phase in the plasma called reactively sputter deposition. Due to the plasma activation, the reactive gas gets more chemically reactive.

Sputter deposition is preferably used to coat semiconductor materials with thin film metallization, but it is also used for the deposition of architectural glass and for reflective coatings on compact discs (CDs), for magnetic film, dry film lubricants, hard coatings and for decorative coatings.

4.2.5 Impact Factors on Film Properties

The properties of thin films and coatings are unique in comparison with bulk materials and cannot be easily looked up in a handbook. However, it is confirmed that the nature of substrate surface and the conditions during the deposition process are decisive for final properties of the deposit layers.

Five main factors are responsible for the properties of a film made by atomic layers deposition process:

a) The *surface of the substrate*, which means the morphology like roughness or contaminations in the film and the chemistry of the surface like the chemical composition and mechanical properties.

b) The *deposition process* and *system parameter*, which includes the temperature, the deposition rate and the particle bombardment (mass, energy...) for example.

c) Kind of *film growth* on the substrate like condensation or nucleation of the atoms or the formation of interfaces

d) *Intermediate processing* steps like oxidation between the layers or polishing between the layers

e) *Post- deposition processing and reactions*, which includes chemical reaction of the surface with the environment, for example corrosion.

For the understanding of the film growth on surfaces a prior investigation of the real surface, which is always different to the bulk material, is necessary. The morphology of the substrate surface strongly affects the properties and morphology of the emerging film. The mechanical properties of the substrate material are responsible for the quality of the film structure and the adhesion of the film on the substrate.

4.2.6 Real Surface Substrates

The aim of a PVD process is to generate a reproducible product, which is only possible if a reproducible substrate surface is available. Generally, the real surface differs from the bulk material due to adsorbed contaminations and the reaction with oxygen or hydrocarbons from the environment. The homogeneity of the substrate surface is also important to obtain a homogeneous film. Therefore, sometimes the surface has to be prepared by various cleaning steps or chemical, mechanical or thermal process methods to give a reproducible surface.

The adhesion, the film growth and the resulting film properties strongly depends on the chemistry, the surface and the mechanical properties of the substrate surface. However, also the bulk material plays an important role for the capability of the surface. Thus, it is difficult to deposit a hard coating on a smoother

substrate because the film might be damaged if the underlying material is deformed. Diffusion and outgassing from the bulk material also have influence on the deposition process and the surface formation.

4.2.6.1 Metal Substrates

Metals are often used as substrates for physical vapor deposition processes. Thereby, it is important to consider that metals except gold are usually covered by an oxide layer, which forms the real surface of the substrate. Depending on the desired result and process, the deposition either directly takes place on the oxide layer or it has to be removed before the coating process. A problem of the oxide layer poses its high surface energy, which leads to the absorption of molecules with lower surface energy like hydrocarbons. These contaminants have to be eliminated from the surface before the physical deposition process because these adsorbates can influence the film growth negatively.

The preparation of the metal can be accomplished by cutting it into shapes or by deformation. The cutting is done by machining or sawing using lubricants, which might remain as contaminants at the metal surface. The deformation process includes rolling, drawing or shear forming. Thereby, lubricants can be used, which are integrated into the surface or even below the surface. Especially solid particulates can be pressed into the surface due to deformation processes and become inclusions of the substrate, which may affect the thin film growth on the metal.

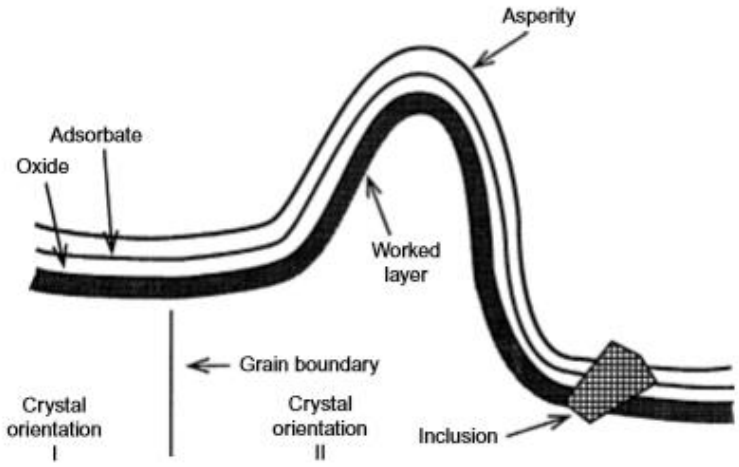

Figure 2 - Surface of a deformed metal substrate ***[1]***

Metals can be protected by oils or rust preventative to decrease the reaction of the surface with the environment. Oxide-free steel, for example, immediately forms ´flash rust´, when it is exposed to the atmosphere. This phenomenon can be minimized by using ´flash rust inhibitors´. Therefore, the inhibitor is put on the cleaned surface before drying. These ´flush rust inhibitors´ are either tolerated as contaminants in further processes or removed by in-situ cleaning directly in the deposition system.

4.2.7 Characterization of the Surface

The analysis of the substrate surface prior the deposition processing is important to determine characteristics and the properties of the item, which may influence the film growth during deposition. Therefore, the characterization method has to be precise, but not necessarily accurate. The method should give information about the morphology of the surface, the microstructure, the mechanical properties like strength and elasticity and the elemental composition of the surface. The investigation of the layers below the surface (near-surface and bulk) is accomplished to get information about the near-surface and bulk properties like outgassing and diffusion possibly influencing the film deposition.

The comprehension of the atomic and molecular nature of matter and the interaction between probing and atoms or molecules are of major importance to characterize the surface.

The chemical composition could be responsible for the nucleation and interface formation of the growing film. Contaminates like hydrocarbons on the substrate surface can lead to minimized nucleation density during the film growth because of decreased chemical interactions. Furthermore, it can be the reason for reduced adhesion of deposited film.

Since only the first few atomic layers are important to the film growth, elemental analysis techniques like Auger electron spectroscopy (AES) probing electrons, ion scattering spectroscopy (ISS) and secondary ion mass spectroscopy (SIMS) probing ions or X-ray photoelectron spectroscopy (XPS) probing photons are used. For the investigation of the near- surface region that might be important for the interface formation methods like Rutherford backscattering spectroscopy (RBS), electron probe X-ray microanalysis (EPMA) and scanning electron microscopy (SEM) in combination with energy dispersive spectroscopy (EDS) are used. The SEM-EDS technique will be further discussed in detail in Chapter 4.3.

A disadvantage of the analytical methods mentioned above is that only relatively small areas of the surface can be investigated. Hence, surface inclusions could be overlooked, which consequently leads to holes in the deposited film.

The morphology of the substrate is defined by the roughness of the surface and affects the morphology of the deposited film, the surface coverage and the properties of the film. The roughness is specified by the R_{max} value, which indicates the distance between upper and lower profiles. The investigation of the roughness is of major importance to be able to assess whether the valleys on the surface can be filled by the deposited film.

Instruments used for the investigation of the surface roughness are called profilometers, for example atomic force microscope (AFM) or scanning tunneling mode (STM).

In addition to the chemical composition of the surface and near-surface region, also knowledge about the mechanical properties is important. That means that the adhesion between surface and film is low if the substrate fractured easily. The surface energy to define solid surfaces is also of major importance and indicates the surface contamination. The higher the surface energy the higher is the ability to adsorb lower energy molecules like hydrocarbons to lower their energy.

4.2.8 Bulk Properties

Outgassing and out-diffusion are typical bulk properties, which influences the growth of the deposited film and its properties. Outgassing means the diffusion of a mobile phase through the bulk to the surface, where it vaporizes. In metals hydrogen typically gasses out. In an out-diffusion process the mobile phase reaches the surface without vaporization and remains there as contaminants.

4.2.9 Low Pressure Plasma Processing Environment

Plasma is a gaseous environment usually established in low pressure that contains many ions and electrons to be a good electrical conductor. To achieve a good plasma a good vacuum system is required. In plasma processing systems the conductance of the pump system is reduced compared to a vacuum processing system to diminish the flow of the processing gasses through the PVD system. The minimized conductance in the plasma environment leads to a reduced pump away of contaminants, which result from the process or the system during the deposition process. Furthermore, plasma is responsible for the activation of the contaminants to become more chemically reactive.

In general, plasma environment contains more contaminates than vacuum systems. In addition, the uniformity of plasma depending on the system geometry, the arrangement of the electrodes and the fixturing also poses a problem.

To generate a plasma atmosphere high DC voltage is applied between two electrodes in a vacuum system. The electrical conductance depends on the gas pressure in the system. If the pressure is very low ions occurring from naturally radiation are caught. With rising gas pressure, the current increases due to the generation of ions by electron-atom collision and the acceleration of the electron and ions. If the pressure rises, a normal glow discharge will build a bright spot on the cathode, called cathode spot. Further increasing pressure leads to a larger spot, but the current density remains the same. However, when the spot covers the whole cathode the current density becomes a function of gas pressure. This region will be called abnormal glow discharge region. The region between cathode and anode will be filled with plasma, although most of the potential drop happens near the cathode (Fig. 3)

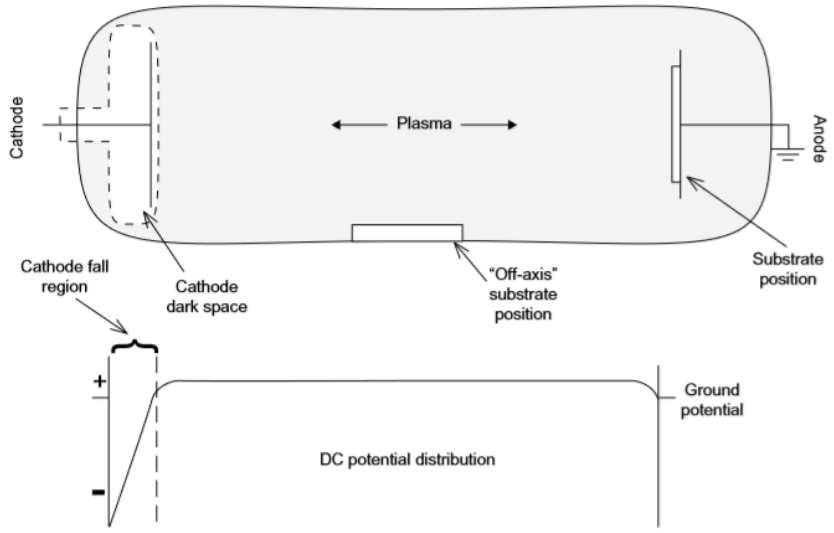

Figure 3 - Generation of plasma. Direct current diode discharge showing the potential distribution across the discharge. ***[1]***

Increasing gas pressure leads to better electrical conductance until finally an arc is build and the potential drop and the current density increases.

In plasma environment electron-atom collisions are responsible for chemical processes. The electrons are accelerated through an electrical field. Electrons are generated by thermal emission from a hot cathode, from an ion- or electron- bombarded surface, from ionizing collision or from a hollow cathode. **[1]**

4.2.10 Magnetron Sputtering

In traditional sputtering processes, the cathode (target) is bombarded with ionized particles, which were generated in a glow discharge plasma directly in front of the target. Thus, atoms from the target are removed and condense on a substrate surface as a thin film. To maintain the plasma in the system the secondary electrons emitted from the target by the ion bombardment are as well very important.

Nevertheless, the basic sputtering process has disadvantages like low deposition rates, low ionization efficiency in the plasma and high substrate heating effects.

Since the development of magnetron sputtering, especially unbalanced magnetron sputtering, these limitations have been overcome.

Magnetron systems use magnetic fields, which are parallel formed to the target surface to constrain secondary electron motion to the nearness of the cathode. One magnetic pole is placed at the central axis of the target and the other pole is generated by ring magnets around the outer edge of the target. **[2]**

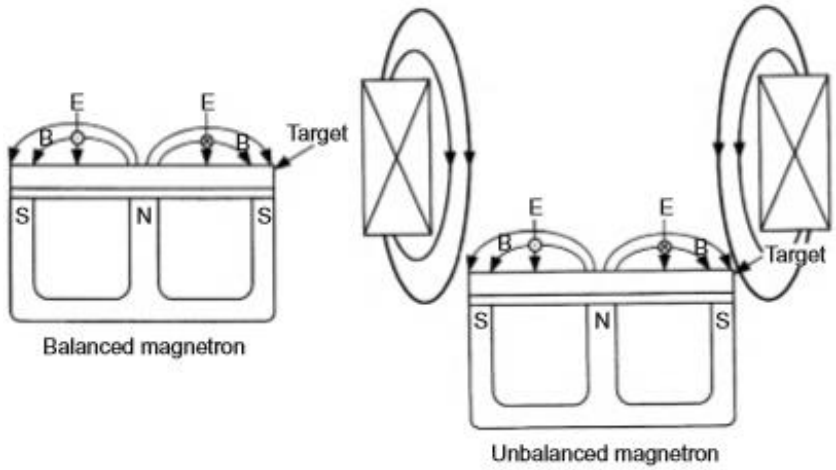

Figure 4 – Schematic drawing of balanced and unbalanced magnetron ***[3]***

Due to that assembly of magnets mentioned above, electrons are trapped and thus the number of ionized electrons and atom collisions (ionization efficiency) increases. This leads to a dense plasma in the target region, which results in an increased ion bombardment of the target. This in turns leads to higher sputtering rates and subsequently to higher deposition rates at the substrate. Even at lower operating pressure (10^{-3} mbar) and operating voltage (500 V), the discharge remains due to the increased ionization efficiency in magnetron sputtering systems.

The design of a basic sputtering magnetron compared to an unbalanced magnetron is minimal but the difference in performance is very significant.

In a conventional magnetron dense plasma reaches about 60 mm from the target surface. The film grow in this region is influenced by a concurrent ion current and subsequently can affect the thin film properties and structure.

The ion bombardment onto a substrate in regions of low-density plasma is generally insufficient to modify the deposited film. The energy of the ion current can be increased by applying a negative bias to the substrate. However, this can result in defects or increased film stress, which negatively influences the

For unbalanced magnetron systems the outer ring of magnets is enhanced relative to the central pole. Due to that, not all field lines are closed between the central and the outer poles. Some are aligned towards the substrate and some secondary electrons can follow these magnetic field lines and escape from the cathode region. Subsequently, the plasma is no longer limited to the near target region, but it flows out towards the substrate film properties. Thus, it is challenging to coat large or complex items by using a conventional magnetron system.

4.2.11 Unbalanced Magnetron

Thus, a high ion bombardment can be achieved without the need of externally bias the substrate. Due to the modified arrangement of the magnets in unbalanced magnetron systems a current density of about 5 mA/cm^2 and larger can be achieved.

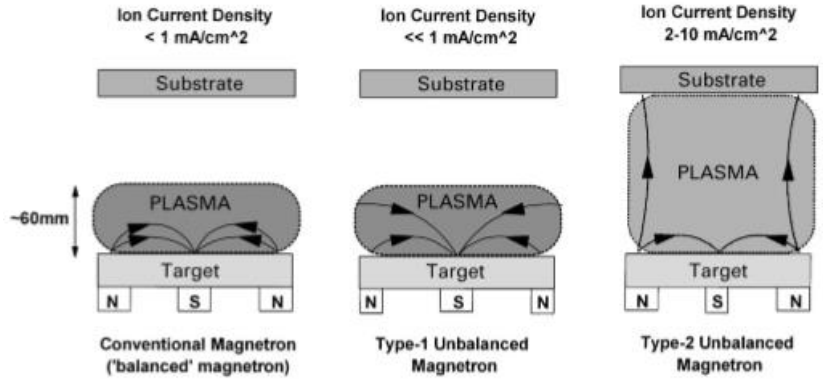

Figure 5 - The plasma confinement of conventional and unbalanced magnetrons. ***[2]***

The unbalanced magnetron mode enables a high flux of coating atoms and works as a very effective ion source. The ion current bombarding the substrate surface is directly proportional to the target current and the deposition rate is directly proportional to the target current. Due to that fact that the ion-to-atom arrival ratio at the substrate stays constant with increasing deposition rate.

There are two types of unbalanced magnetron systems. ´Type-2´ was discussed in the text above. In ´type-1´ the central pole is enhanced to the outer pole as opposed to the central pole. Thus, the open field lines are aligned towards the walls of the chamber, which results in a low plasma density region near the substrate. This mode is rather rarely used, due to the low ion current at the substrate surface. **[2]**

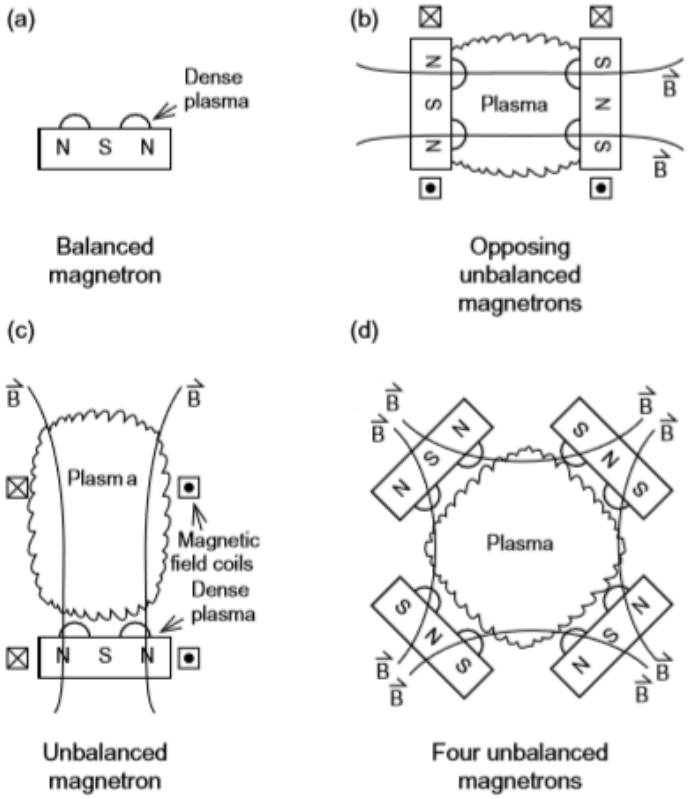

Figure 6 - Various arrangements of planar magnetron sputtering targets. ***[1]***

4.2.12 Film Growth

The film growth near the surface or interface is strongly influenced by the substrate surface. Just after a certain thickness a particular film growth mode is developed. The further film increase can be described by the structure zone model (SZM) for sputter deposition processes (Fig. 7).

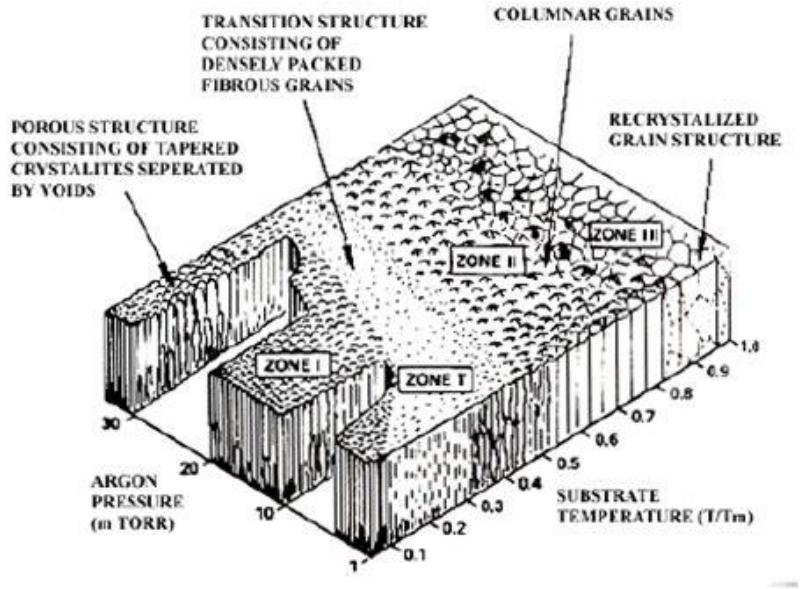

Figure 7 - Structure Zone Model (SZM) for sputter deposition processes. ***[1]***

In Zone 1 of SZM model, separated columns are built due to the irregular surface morphology and the insufficient surface diffusion. This results in a film with high surface and a mossy visual appearance.
Zone T exhibits a fibrous morphology because of the bombardment of high energy neutrals from the target at low gas pressure. Thereby, the valleys from Zone 1 are filled up.
In Zone 2 the columnar structure remains, but the dominating surface diffusion is responsible for the densification of the boundaries between the columns. Furthermore, the grain size rises.
In Zone 3 bulk diffusion dominates and allows grain growth, recrystallization and further densification of the boundaries between the columns. These columns often appear as single crystals of the deposited material.

4.2.13 Sputtering of Alloys

With sputtering deposition, it is possible to deposit elemental materials and alloy materials. Therefore, layer-by-layer is deposited, which means that each single atomic layer has to be completely removed from the target before the next layers can be sputtered. The composition of the bombarding atoms is the same as the composition of the bulk. However, if the materials of the target alloy or mixture have significantly different masses or sputtering yields, the deposited film does not have the same composition as the target material. **[1]**

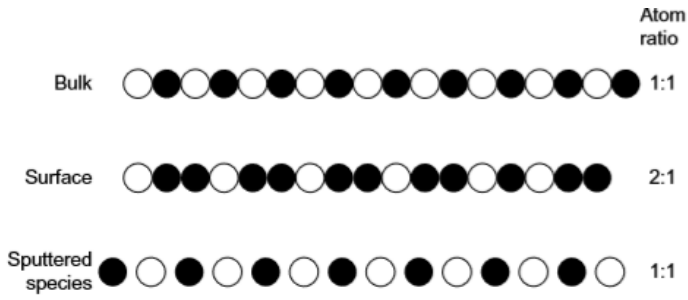

Figure 8 - Layer- by- layer- sputtering. ***[1]***

4.2.13.1 Preferential Sputtering and Sputtering Yields

The phenomenon that the different components of a multicomponent target are not sputtered in the proportion to the concentration of the surface material is called preferential sputtering. This is caused due to different effects like mass differences of the target atoms, different surface binding energies and chemical bonding or thermal or radiation induced segregation. Preferential sputtering leads to the formation of an altered layers near the surface region. This layer is different to the composition of the bulk. At relatively low temperatures, when thermal diffusion can be neglected, the thickness of the altered layers stays finite and the steady-state condition can be achieved, where the concentration of the evaporated material is almost the same as the concentration of the bulk composition.

For multicomponent materials, three types of sputtering yield are defined, the total sputtering yield, the partial sputtering yield and the component sputtering yield. The relationship between the total and the partial sputtering yield is:

Equation 1 – Total sputtering yield ***[6]***

$$Y = \sum_i Y_i$$

Y *…total yield*

Y_i *…partial sputtering yield*

The total sputtering yield is defined for single element target and it is the average number of sputtered atoms per incident particle, whereas the partial sputtering yield is defined for multicomponent materials and means the average number of sputtered atoms of component i per incident ion.

The component sputtering yield is defined as the partial sputtering yield divided by the concentration of each component during sputtering. This means that the partial pressure becomes zero when the concentrations get zero. **[6]**

Equation 2 – Component sputtering yield ***[6]***

$$Y_i^c = {Y_i}/{c_i^s}$$

Y_i^c *...component sputtering yield*

Y_i *...partial sputtering yield*

c_i^s *...concentration of each component*

4.2.14 Surface Preparation

Accurate surface preparation is very essential regarding to the nucleation and interface formation during the deposition process. Thus, the surface is responsible for the adhesion of the film and the overall surface coverage. Furthermore, the surface determines the structure of coating and the properties. Surface preparation does not only mean the cleaning of the surface, but it also includes the modification of the surface, like morphology or chemical properties. It is distinguished between external cleaning, which happens external to the deposition chamber and in-situ cleaning, which is done directly in the process chamber. External cleaning includes ultraviolet-ozone (UV/O_3) oxidative cleaning and sputter (physical) cleaning. Reactive plasma cleaning was the first method for in-situ cleaning. Chlorine containing or hydrogen containing plasma is used for this cleaning technique.

Another method is ion-scrubbing, which is performed just before the physical vapor deposition in plasma environment. The surface in contact with plasma receives a negative voltage of only several volts with respect to the plasma. Thus, positive ions are accelerated to the surface. When the ions hit the surface, electrons are generated, and the ions release their ionization energy of about 5 to 20 eV. Due to this, smooth bombardment of argon ions remaining contaminates such as water vapor can be knocked off. **[7]**

4.2.15 Multilayer Systems

It can be distinguished multilayers systems with small number of single layers, with high number of single layers and with isostructural single layers.

Nowadays, the most common type of multilayer systems belongs to the group of coatings with a small number of single layers.

The idea of depositing layers on various materials is mostly to improve the toughness to prevent cracks and fractures and to reduce the crack propagation. Studies show that wear and material properties depend on the ratio of toughness to the hardness of the material (strength). Interfaces in multilayer systems are in charge of toughening the material by energy dissipation through the interfacial site and crack deflection. Furthermore, multilayer systems are applied for grain size and texture adjustment. Thus, such systems have a functional and structural purpose.

For a functional design, different materials with different tribological functions are combined in the deposited films to reduce wear. Structural design includes the adjustment of grain size, the shape of the

grains and the thickness of the layers to improve the properties of the substrate material to hardness and toughness. **[8]**

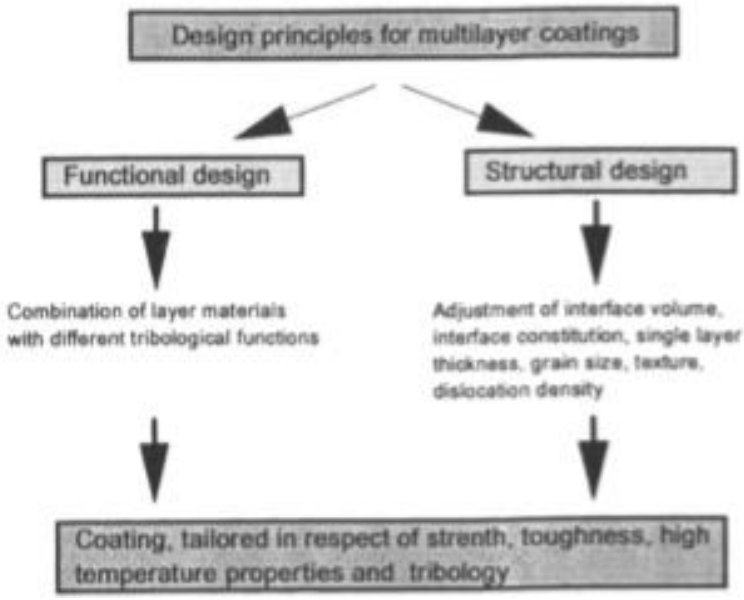

*Figure 9 - Design principles of multilayer PVD coatings for wear protection **[8]***

Additional, adherent layers are often very important to establish a basis for a further constitution of layers on a substrate material.

4.3 Scanning Electron Microscopy

4.3.1 Principle of Scanning Electron Microscopy

Scanning electron microscopy (SEM) is widely used for the observation and characterization of various bulk specimen on nanometer to micrometer scale. This method delivers topographic three-dimensional images of the surface of organic and inorganic materials. However, the scanning electron microscope with a magnification range of 10- 10000 × can be used more versatile.

The area of investigation is irradiated with an electron beam for an analysis of the position. Different types of signal are produced during the electron beam scans the sample, which are used to obtain an image. This signals like secondary electrons, backscattered electrons, characteristic X-rays and other photons with different energies are generated due to the interaction of the primary electrons with the sample. Due to the different emission volumes with the sample the obtained signals give information about topography, composition, etc.

For the topographic analysis of a surface secondary and backscattered electrons are detected because this kind of electrons are generated due to differences in the topography.

Characteristic X-rays are also generated due to the electron bombardment of the sample. These signals are used for qualitative analysis and to gain quantitative information about the material. The interaction volume of the primary electrons is about 1 µm in depth and 1 µm in diameter under normal measuring conditions.

The SEM consists of two major parts, the electron column and the control console. The electron column includes an electron gun and two or more electron lenses, which determine the path of the generated electrons down to the sample in an evacuated system. Vacuum pumps positioned at the base of the column generate a vacuum about 10^{-4} Pa. The constituents of a control console are a cathode ray tube (CRT), a viewing screen and the buttons and the computer keyboard to control the electron beam.

With an electron gun, electrons are produced and accelerated to an energy of 0.1 to 30 keV. For a tungsten hair gun electron lenses are used to generate a sufficient small spot size of the electron beam. For most SEMs a spot size of less than 100 nm can be achieved and, nevertheless, contains enough probe current to generate an acceptable image. The electron beam reaches the specimen chamber after going through the final lens and interacts with the sample in a depth of approximately 1 µm.

To generate an image the sample is scanned point by point with the focused electron beam. With the deflection system it is possible to move the electron beam across the sample along a line and then along another line little below the previous line and so on. Thus, a raster is obtained, which is simultaneously transferred with the same scan generator to a viewing screen. Two pairs of scan coils (electromagnetic) are used to raster the electron beam across the sample. The of the image results from the ratio of the length of raster on the viewing screen to the length of the raster of the specimen. To obtain an increased magnification the scan coils are excited less strongly, so the electron beam deflects across a smaller distance on the sample. The magnification also depends on the working distance.

When an electron beam interacts with a sample various signals are generated, which are detected to obtain an image. The electronics of the detector convert these signals to changes in intensity on a viewing screen. Mostly secondary and backscattered electrons are detected. Therefore, the standard detector Everhart-Thornley (E-T) is used. The electrons are captured due to the applied positive voltage on the collector screen in front of the E-T detector. Only backscattered electrons can be captured if a negative voltage is applied to the collector because secondary electrons with lower energies are repelled. In the last steps the electrons are captured with a scintillator or a photomultiplier to strengthen the signal and display it on a viewing cathode ray tube. The images are finally stored in digital form in a computer.
The first task of the operator is to control the generation of the electron beam by acceleration voltage and emission current. Then the condenser and objective lenses must be controlled. The condenser lenses define the amount of beam current and the size of the beam. The objective lens further reduces the beam and focuses the electron probe exactly onto the sample surface. **[9]**

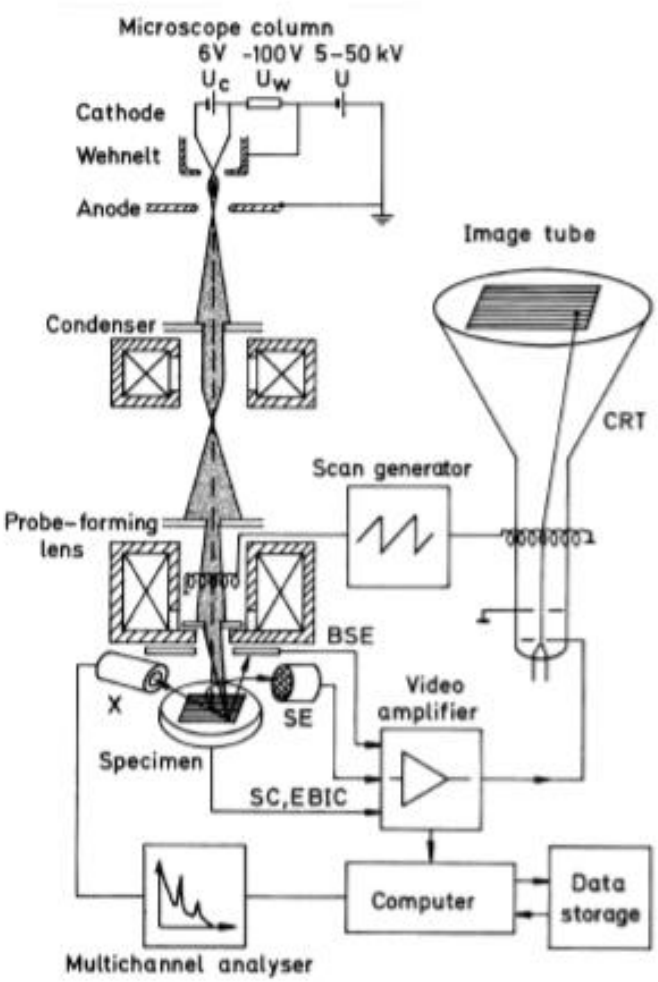

Figure 10 - Schematic drawing of a scanning electron microscope consisting of the electron gun, lenses, the deflection system and the electron detector. ***[10]***

4.3.2 Imaging Modes

For the interpretation of the images and to gain as much information as possible out of it, it is important to understand the measuring conditions. The sharpness of the image and the visibility of features depends on electron probe size, the electron probe current, the electron probe convergence angle and the electron beam accelerating voltage. Each of these parameters are responsible for the four imaging modes: resolution mode, high-current mode, depth-of-focus mode and low-voltage mode.

In the resolution mode the probe size must be as small as possible but must contain sufficient beam current at the same time to obtain an image, where features of interest can be displayed. To image fine features the probe size must be the same or even smaller as the features of interest. This mode is only senseful at high magnification, where these small details can be depicted. Resolution is defined as the size of the finest detail that can be monitored.

With the high-current mode the best image visibility and quality can be achieved. A problem is that even at small spot sizes, the contrast between image features and background cannot be distinguished. High current is necessary for the X-ray microanalysis because only a few electrons results from the interaction with the specimen in form of X-ray emission.

To obtain the best depth of focus the convergence angle must be kept as low as possible. Thus, the different heights on the surface will all appear sharp at the same time.

The low-voltage mode (lower than 5 keV) is used to image the surface near region. These images are very rich in information about the surface. The higher the accelerating voltage (15 – 30 keV) the deeper the electrons penetrate the sample and deliver information about the bulk of the specimen.

4.3.3 Electron Guns

The task of the electron gun is to offer a stable and adjustable primary electron beam. Thermionic emitters (tungsten and LaB_6) were preferable used in older scanning electron microscopes. Nowadays, cold, thermal or Schottky filed emission sources are available. These methods promise longer lifetime and excellent performance.

The tungsten hair electron gun is one of the most common electron sources in SEMs. The electron gun consists of a tungsten wire filament, which serves as cathode, the grid cap or Wehnlet which serves as control electrode and an anode. To generate an electron beam the high voltage in the range of 0.1- 30 keV is applied. The grid cap is used to focus the beam by applying a more negative voltage compared to the filament.

The lanthanum hexaboride (LaB_6) electron guns emit more electrons at the same heating temperature meaning that the material has a lower work function. Furthermore, it offers a longer lifetime and higher brightness compared to the tungsten hair electron gun. The tiny block of single-crystal LaB_6 is heated by carbon or rhenium. If the applied current is high enough to raise the temperature emission takes place.

The advantages of these thermionic sources are the relatively low costs and that no special vacuum must be supplied. However, the low lifetime, the limited brightness and the huge energy spread were the reasons to search for another electron source.

The field emission is another way to generate an electron beam without the problems mentioned above. The field emission gun consists of a wire (cathode) with a sharp point and is supported by a tungsten hair. The wire is made of tungsten, carbon or silicon nanotubes. To generate an electron beam a negative potential is applied to the cathode until the tip reaches a potential magnitude of about 10 V/nm. Consequently, the potential barrier gets lower in height and becomes so narrow at the same time that the electrons tunnel through it and leave the cathode.

Two classes of field emission sources are commonly used in SEMs, the cold field emitter and the Schottky/ thermal field emitter. For cold field emitters a high voltage is applied to generate electron tunnel. The magnitude of the emission does not depend on the temperature of the tip, so the type of field emission is called cold field emission.

The second class of field emission methods include thermal and Schottky field (TFE and SFE) emitters. The thermal field emitter only differs from the cold field emitter in a higher operating temperature. This leads to less impurities residues at the tip, and, thus less noise and instability. Furthermore, the tip is sharpened in the extraction field and an enhanced performance can be achieved.

The electrical field at the tip generated from Schottky emitters is used to reduce the work function barrier. To further reduce the work function, ZrO_2 is deposited on the flattened tip. Thereby, high brightness and emission density comparable to cold field emission can be achieved although the Schottky field emitter is a thermionic source. The SFE includes a suppressor to eliminate the thermionic emission generated from outside the regions of the tip. **[9]**

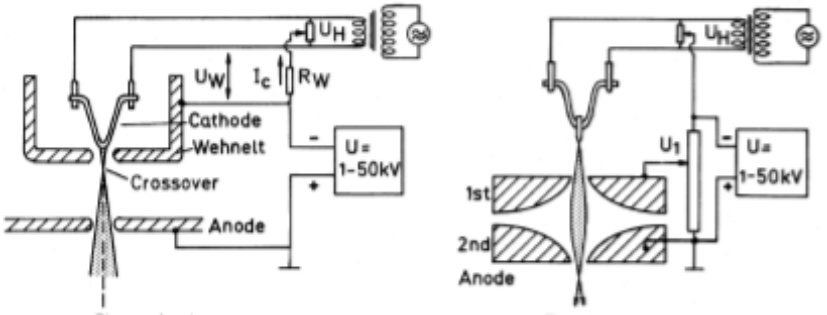

Figure 11 - Thermionic electron gun consisting of cathode, Wehnelt cup and anode (left). Field-emission gun of the Butler triode field emission source consisting of a wire (cathode) and two anodes (right). ***[10]***

4.3.4 Electron Lenses

The purpose of electron lenses is to make the electron beam smaller by focusing and demagnifying it. Therefore, electrostatic or electromagnetic fields are used. SEMs only use electromagnetic lenses due to the minor aberrations. Two different types of magnetic lenses are distinguished, the condenser and the objective lens. The condenser lens is used to control the demagnification of the beam. The objective lens focuses the electron beam onto the surface of the sample and as well contributes to demagnification.

Since more current flows through the objective lens, it must be water-cooled. There are three types of objective lenses, hole lens, immersion lens and snorkel lens. For hole lenses the sample is positioned outside the lens and its magnetic field. For immersion lenses the specimen is placed inside the lens and the magnetic field. For snorkel lenses the magnetic field reaches out the sample below the physical lens. **[9]**

4.3.4.1 Gemini lens system

The Gemini lens system ZEISS described in the following chapter was used for all investigations and measurements of the master thesis. The Gemini Optics (Fig. 12) consist of three major components.
The Gemini- objective lens design combines electrostatic and magnetic fields to enhance the optical performance and to eliminate the field impacts to the sample. This enables excellent imaging of complex samples like magnetic materials. The Gemini-beam booster-technology, which means an integrated deceleration of radiation (electron beam), enables a small spot size and high signal-noise-ratio. The InLens-detection system of the Gemini technology ensures an efficient signal detection due to the parallel detection of secondary and backscattered electrons at a minimized image capturing time. The Gemini lens system gains information only from the top layers of the samples. The InLens-SE-detector generates images with real surface sensitive SE1- electrons. Due to the optic, which is almost free of magnetic fields, distortion- free and high-resolution imaging is possible. Furthermore, an excellent material contrast at very low acceleration voltage with the InLens EsB (energy selective backscattered) detector can be achieved. **[10]**

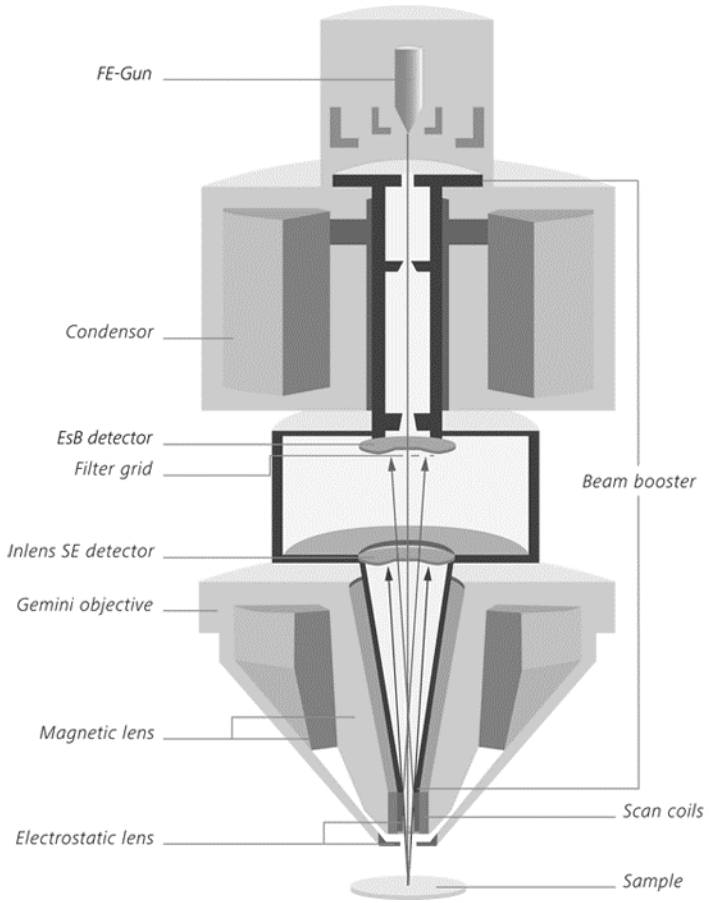

Figure 12 - Schematic drawing of Gemini Optics with SE InLens detector. ***[11]***

The Gemini angle selective backscatter electron detection (AsB or HDAsB for high definition angel selective electron detection) system (Fig. 13) is used to detect the low angle backscattered electrons. This detector arrangement in the Gemini system enables to separate between low angle BSE and high angle BSE. With the AsB detection system compositional contrast and crystal orientation are investigated. **[12]**

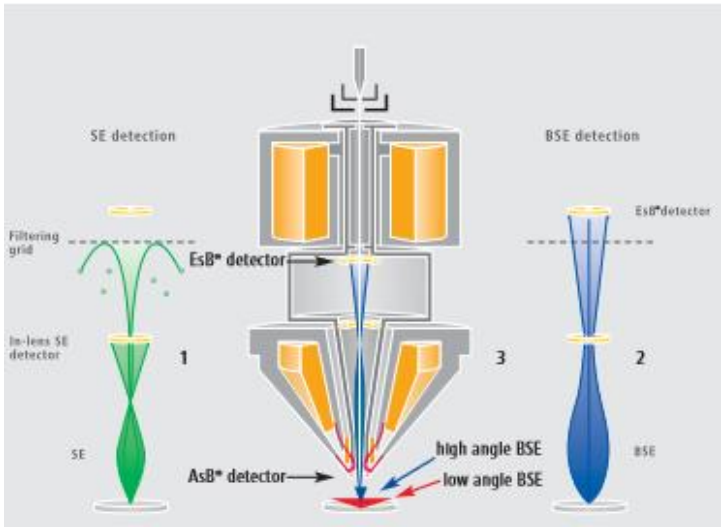

Figure 13 – Schematic drawing of Gemini AsB detection system. This lens systems enables the separate detection of high angle BSE with EsB detection and low angle BSE with AsB detection system. ***[12]***

4.3.5 Electron Specimen Interaction

The interaction processes taking place when the primary electron beam hits a specimen are called elastic and inelastic scattering. The final signal used for imaging does not arise from single scattering processes but from the complete electron diffusion, which is caused by the loss of energy and by lateral spreading from multiple elastic scattering. This gradual loss of the energy of the primary electrons depends on the electron energy and density of the specimen. The signal intensity varies with the depth. The deeper the electrons penetrate the specimen the lower is the received signal for image formation. The electrons emitted from the sample consist of secondary electrons (SE), backscattered electrons (BSE) and Auger electrons (AE).

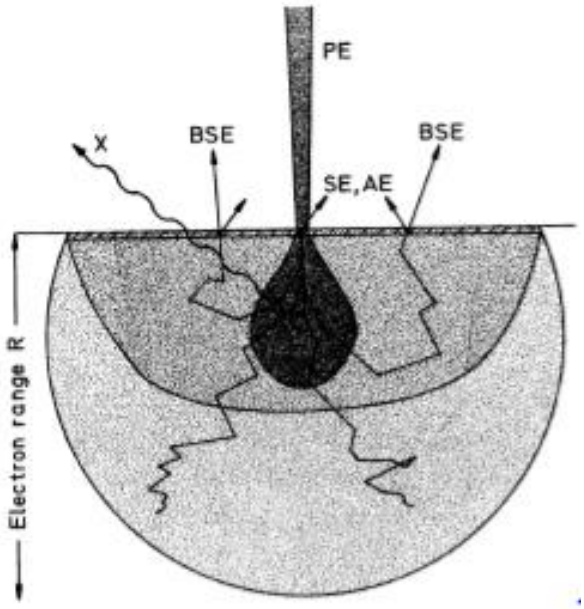

Figure 14 - Electron-specimen-interaction of the primary electron beam. Origin and information depth of secondary electrons, backscattered electrons, Auger electrons and X-rays. ***[10]***

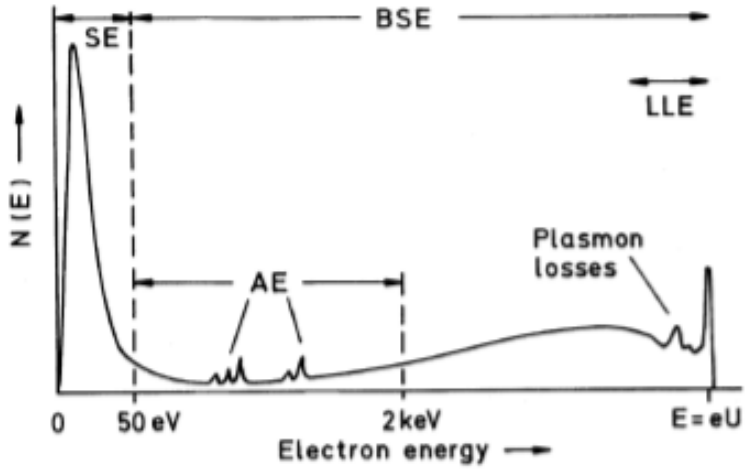

Figure 15 - Schematic energy spectrum of emitted secondary electrons (<50 eV), low-loss electrons (a few hundreds of eV), backscattered electrons (>50 eV) and Auger electrons. ***[10]***

The signal of SE generated by inelastic collision is at energies between 2 and 50 eV (Fig. 15). The spectrum of BSE electron reaches from 50 eV to the primary electron energy E= eU. This is caused due

to the deceleration of the electrons that undergo multiple energy losses caused by multiple scattering through large angles. Auger electrons are generated after ionization of an inner shell and build an alternative to characteristic X-ray emission. Either the energy, which is released when an electron from an outer shell fills the electron hole in the ionized shell is converted to X-ray quantum, or the energy is transferred to another electron in the atom and gets knocked out of the specimen as an Auger electron.
Secondary electrons and Auger electrons preferable undergo elastic and inelastic scattering, thus these electrons can leave the sample only from the near-surface region, which is a few nanometers thick. This kind of electrons can also be generated by backscattered electrons on their way back through the surface region.
The energy of the backscattered electrons corresponds to the broad part in the spectrum shown in Figure 15. The elastic peak followed by plasmon losses depends on the primary energy, the tilt of the sample and the take-off angle. The mean electron energy decreases continuously with the increasing path of trajectory of the electrons inside the sample. Generally, electrons with higher losses of energy and lager paths of trajectory originate from deeper regions of the sample.
The so called low-loss electrons (LLE) show an elastic peak between the energy range of 10- 100 eV below the primary energy and leave the specimen only from near-surface region like secondary and Auger electrons.
The characteristic X-rays originate from the depth, in which the energy of the electrons get higher than the ionization energy of the inner shell involved. X-rays, which are excited in an atom of element x can be absorbed by element y if the energy of the characteristic X-rays is higher than the ionization energy of the atoms of element b. This absorption leads to secondary X-ray or X-ray fluorescence formation.
These generated signals illustrate that different electron-specimen interactions deliver a lot of information in form of particles and quanta emission, which can be used for different imaging and operating modes of a scanning electron microscope. **[10]**

4.3.5.1 Interaction Volume

The interaction volume shows the electron trajectories inside the target and can be simulated by Monte Carlo simulations (Chapter 4.3.5.2). Various beam and specimen parameters significantly influence the size and shape of the Interaction volume.

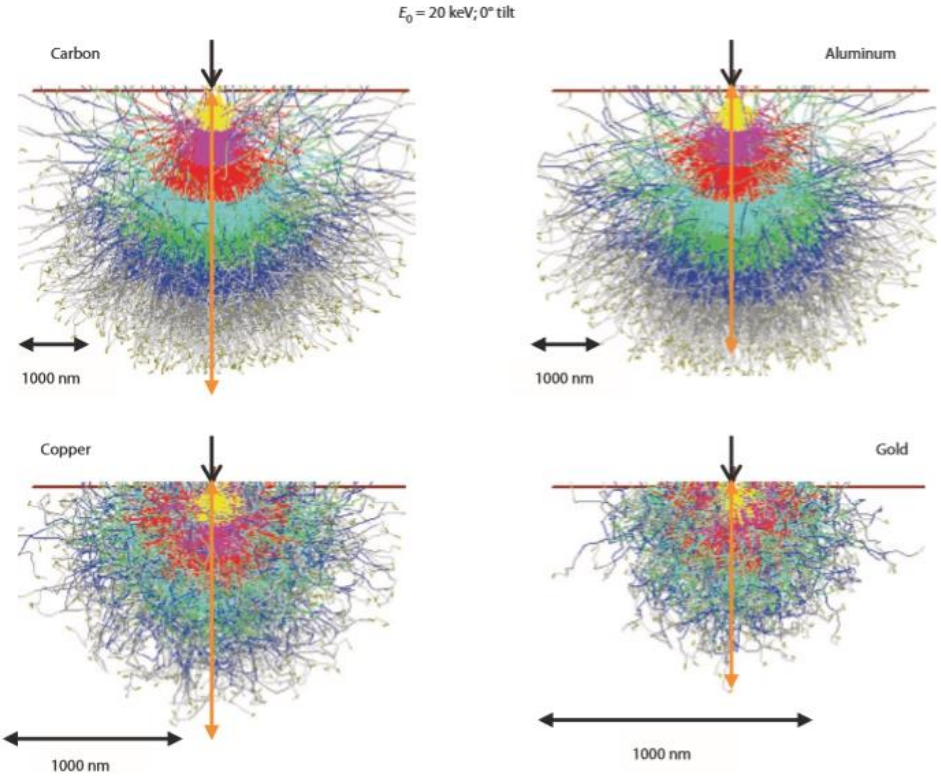

Figure 16 - Interaction volume and electron trajectories of different elements simulated by Monte Carlo simulations. ***[13]***

Thus, the size of the interaction volume strongly depends on the energy, with which the beam electrons interact with the sample. The higher the beam energy (eV), the larger is the corresponding interaction volume. This can be explained by Equation 3. The cross-section for elastic scattering is indirectly proportional to the square of the energy (Eq. 3).

Equation 3 -Cross-section in dependence of energy ***[9]***

$$Q \sim 1/E^2$$

Q…cross-section

E…energy

This means when the beam energy increases, the path of the electrons close to the surface become straighter and, thus, the electrons can penetrate deeper into the target before elastic scattering leads some electrons back through the solid to generate a detectable signal. Furthermore, the rate of energy loss with the travelled path is inversely related to the energy (Eq. 4).

Equation 4 – Rate of energy loss with travelled path of the electrons ***[9]***

$$dE/ds \sim 1/E$$

dE…rate of energy
ds…travelled path

The higher the electron beam energy, the deeper is the path the electrons penetrate the solid because they hit the specimen with larger energy and this, consequently, leads to a lower rate of energy loss.
Summarizing, the lateral dimension of the interaction volume is influenced by the beam energy, but the shape of the interaction volume does not significantly vary with the beam energy.
The atomic number is another feature, which influences the interaction volume. At a fixed beam energy, the linear dimension of the interaction volume decreases with increasing atomic number (Eq. 5).

Equation 5 – Cross-section in dependence of atomic number ***[9]***

$$Q \sim Z^2$$

Q…cross-section
Z…atomic number

The cross section for elastic scattering is directly proportional to the atomic number. In specimen with high atomic number more elastic scattering occurs and the average scattering angle is larger than for solids with lower atomic number. Thus, the electrons tend to escape from initial path of electrons more quickly, which leads to increasing backscattering and reduced penetration of the electrons into the target (smaller interaction volume). However, the loss of energy increases with rising atomic number, which also leads to a reduced size of interaction volume. Electrons in low atomic number materials tend to less elastic scattering. Thus, the electrons less escape from the initial path of electron beam, which leads to a deeper penetration into the material (larger interaction volume).
The shape of the interaction volume also depends on the atomic number. For lower atomic number materials the dense region of the electron paths resembles a pear shape, whereas for higher atomic number materials the shape of the electron trajectories builds an almost hemispherical shape cut by the horizontal plane of the specimen surface.
The tilt of the target surface has also a significant influence on the interaction volume. That means when the angle of the incoming beam relative to the surface decreases the interaction volume gets smaller and asymmetric. For a tilted sample surface, some electrons expand close to the surface region. Thus, the electrons can escape directly through the specimen surface and will not penetrate deeply into the material (small and asymmetric interaction volume). **[9]**

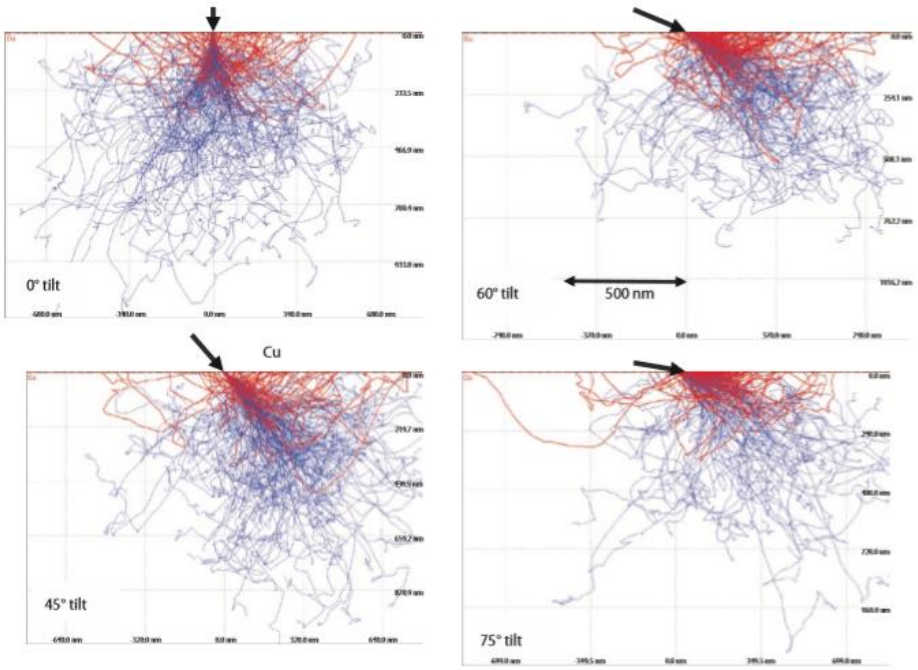

Figure 17 - The influence of the target tilt on the interaction volume of Cu. ***[13]***

4.3.5.2 Monte Carl Simulation

Monte Carlo simulations (CASINO simulation) are performed to visualize the electron interaction volume (Fig. 16), to show, where electrons travel and deposit energy within a specimen for an accurate interpretation of scanning electron microscopy images.

The effect of elastic scattering of electrons from incident electron beam is very complex. So any individual elastic scattering process can result in a wide range of scattering angle up to 180° resulting in a three- dimensional cone. Small scattering angles between 5- and 10° are more frequent than larger angles. The consecutive elastic scattering processes lead to the deviation of path of involved electrons and result in complex electron trajectories within the interaction volume. With Monte Carlo electron trajectory simulation the electron´s behavior including elastic and inelastic scattering can be illustrated. Therefore, several simplifications are performed.

a) All changes in path of the beam electrons are attributed to elastic scattering. For elastic scattering a mathematically model, which uses a random number to choose a properly weighted value for the elastic scattering angle in the range of 1 to 180°. Another random value is used to choose the azimuthal angle in the base of the scattering cone.
b) The distance between two elastic scattering processes is calculated from the mean free path.
c) The inelastic scattering events are calculated by the loss of energy (Eq. 4).

Monte Carlo simulations give a visual depictions and numerical results of beam- specimen interactions, which simplifies the study of this complex phenomenon.

The CASINO Monte Carlo simulation gives detailed information about the energy deposition, as illustrated in Figure 18. It shows that the energy deposition is largest close to the incidence of electron beam and decreases down to the bottom of the interaction volume.

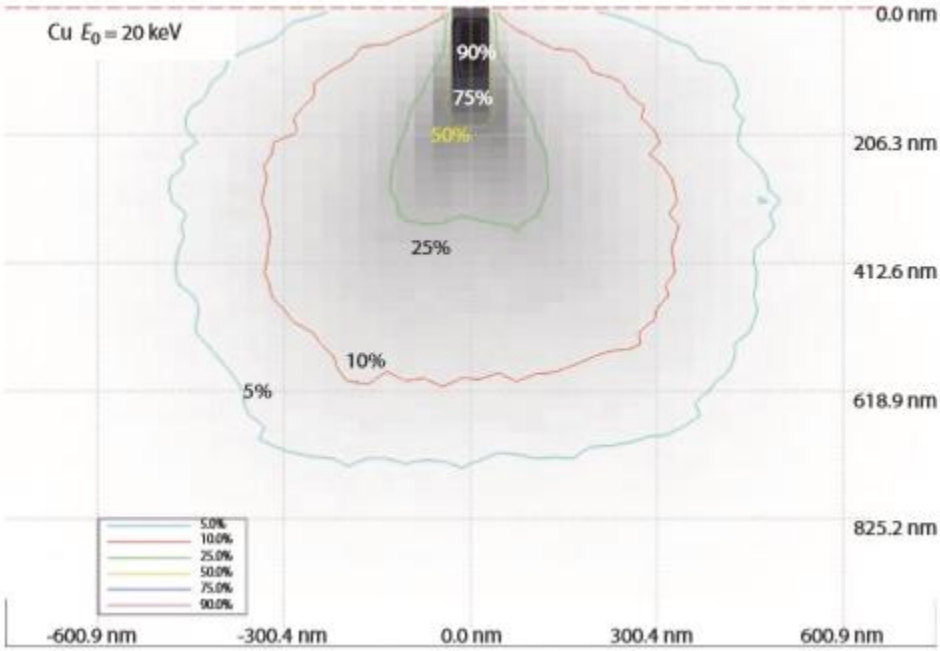

Figure 18 - Detailed information about the energy depositions. ***[13]***

4.3.5.3 Backscattered Electrons

The study of the trajectories of Monte Carlo simulations shows that a significant part of the incident beam electrons undergoes scattering processes and completely change their initial direction of travelling into the specimen. Thus, the electrons return to the surface and leave the specimen. These electrons are called backscattered electrons (BSE) and contain a lot of important information on material characteristics, like composition, topography, mass thickness and crystallography.

The backscattering is quantified by the backscatter coefficient η, which is defined by Equation 6.

Equation 6 – Definition of the backscatter coefficient ***[9]***

$$\eta = \frac{\eta_{BSE}}{\eta_B} = \frac{i_{BSE}}{i_B}$$

η_{BSE} *...number of backscattered electrons*

η_B *...number of incident beam electrons*

i_{BSE} *...current of incident electron beam*

i_B *...current of backscattered electrons*

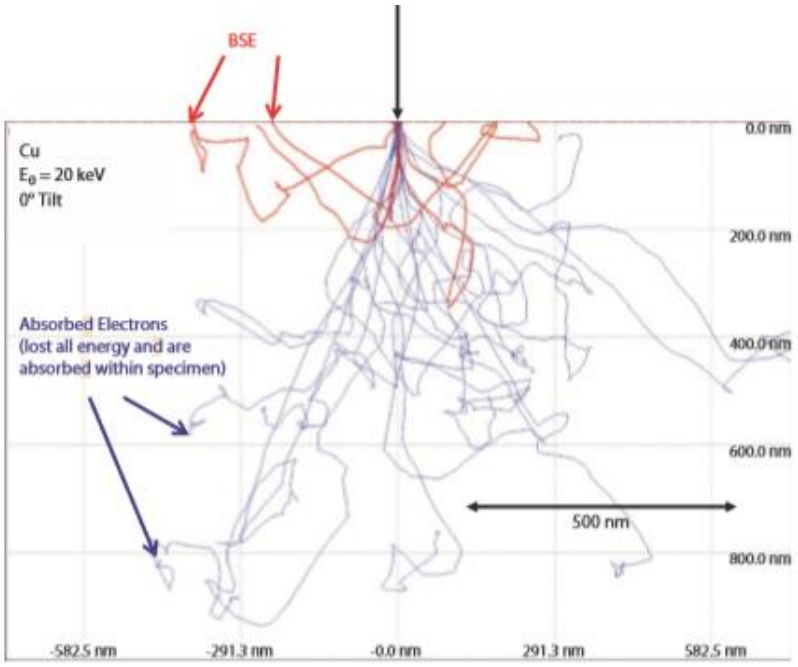

Figure 19 - Copper, E_0= 20 keV, 0° tilt, 25 trajectories, Monte Carlo simulation (CASINO). ***[13]***

Monte Carlo simulations show that the number of backscattered electrons increases with increasing atomic number (Fig. 20). This relationship is used to show the atomic number or also called compositional contrast. The slope of backscattered electrons versus atomic number is relatively steep at the beginning and decreases with increasing Z. Thus, the curve becomes very flat above Z=50. This can be explained by the fact that the atomic number contrast between adjoining elements is strong for low atomic number elements and weaker for high atomic number.

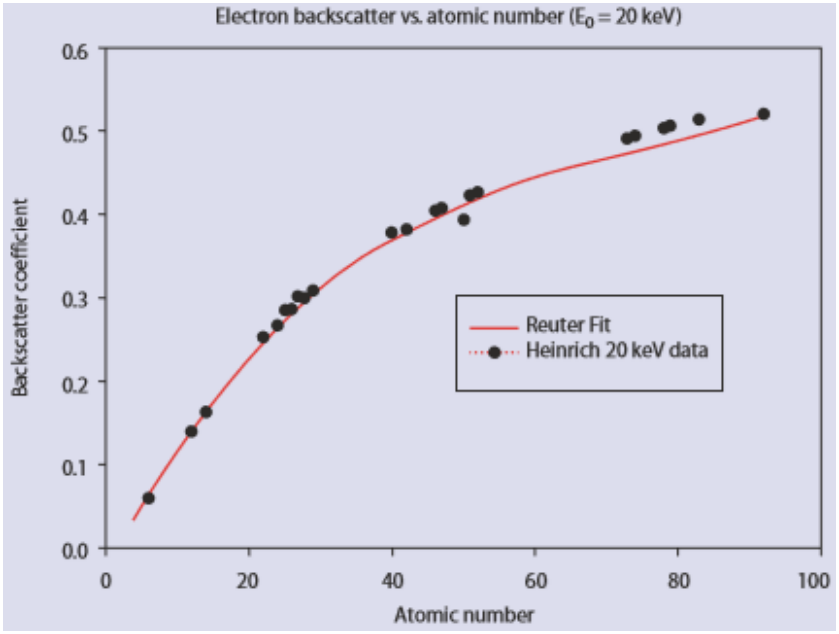

Figure 20 - Electron backscatter coefficient as a function of atomic number for pure elements. ***[13]***

Although the size of the interaction volume strongly depends on the beam energy, the backscattering coefficient does not depend on the acceleration potential. There is only a small change of less than 10%, which cannot be measured with conventional SEM.

The tilt angle, which means the angle between the beam and the surface plane, smoothly influences the backscattering (Fig. 21). Initially, the slop is relatively flat, but becomes steeper with increasing tilt angle (from about 45°). The relationship between backscattering and tilt angle is very important for the investigation of the shape of the specimen. Thereby, the topographic contrast of the object can be represented with SEM.

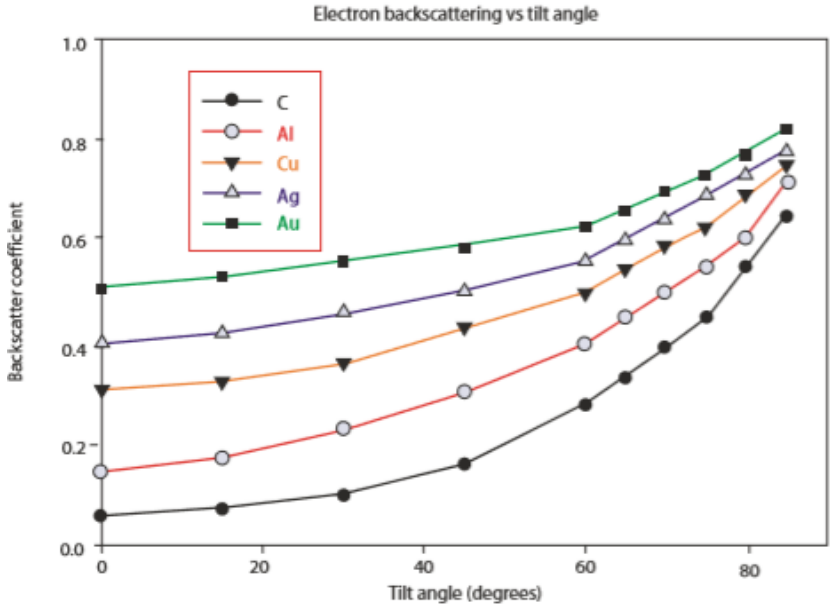

Figure 21 - Monte Carlo calculations of electron backscattering from different tilted pure element bulk targets. ***[13]***

4.3.5.4 Secondary Electrons

Secondary electrons (SE) are generated due to inelastic scattering of the beam electrons, which leads to the ejection of weakly bound valence electrons (ionically or covalent bonded materials) or conduction band electrons (metals). These binding energies are about 1 to 15 eV. The secondary electron coefficient is quantified by δ, which is defined by Equation 7.

Equation 7 – Definition of secondary electron coefficient ***[9]***

$$\delta = \frac{\eta_{SE}}{\eta_B} = \frac{i_{SE}}{i_B}$$

η_{SE} *...number of secondary electrons*

η_B *...number of incident beam electrons*

i_{SE} *...current of incident electron beam*

i_B *...current of secondary electrons*

One main characteristic of secondary electrons is their extremely low kinetic energy. Due to the large difference in relative velocities between the primary beam electron (1-30 keV) and the weakly bound atomic electrons (1-15 keV), only a small amount of kinetic energy is transferred from the primary electron to the SE. Thus, the SEs are ejected at low kinetic energies. When the electron is ejected, the SE must move through the specimen and undergoes inelastic scattering, which leads to further decrease in kinetic energy. Thus, only a few SEs reach the surface with enough energy to escape the specimen and deliver a detectable signal for SEM, the others remain in the material. The energy spectrum of SEs (Fig. 22) illustrates a peak maximum of intensity at very low energy. Above the maximum the intensity rapidly sinks with increasing kinetic energy.

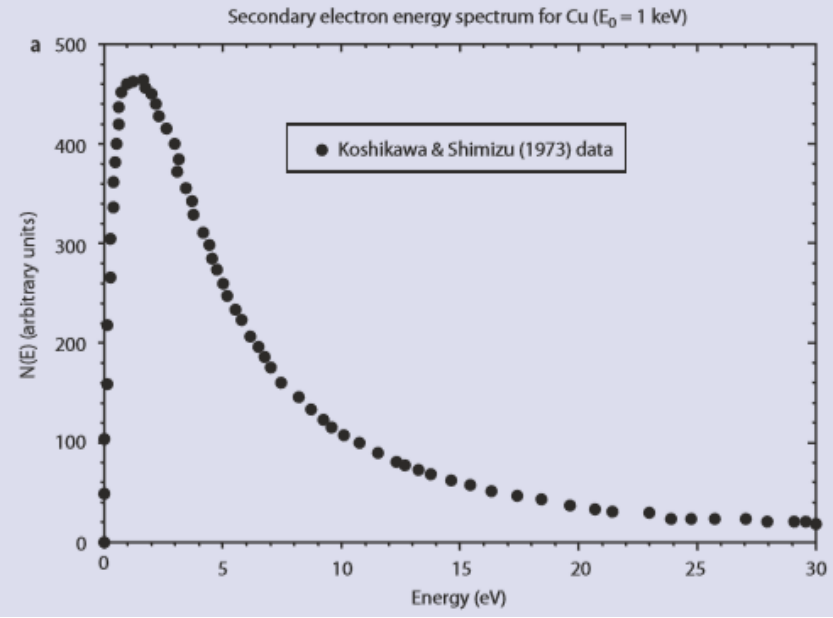

Figure 22 - Energy spectrum of secondary electrons. Measurement of copper target at beam energy of 1 keV. ***[13]***

The low kinetic energy of SE results in a limiting range, from which the SEs can escape from the material of a few nanometers compared to thousands of nanometers for beam electrons or backscattered electrons.

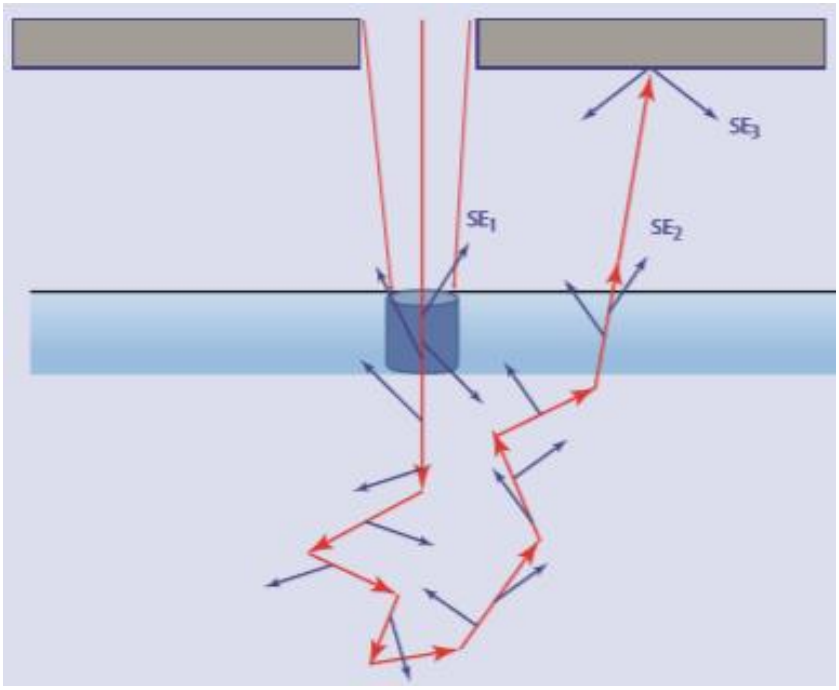

Figure 23 - The origins of the SE_1, SE_2, and SE_3 classes of secondary electrons. SE_1 gives information about the lateral and near-surface region. SE_2 and SE_3 carry backscattered electron information. The blue area shows the escape depth for SE_1 and the cylinder represents the SE_1 escape volume. ***[13]***

There are two different sources of secondary electron generation in a sample, which contributes to the total secondary electron emission. At that moment when the electron beam hit the sample, secondary electrons SE_1 are generated. These electrons give the laterals spatial resolution information defined by the dimension of the incident beam and contains information about the properties of the near surface region. The SE_2 class is generated by backscattered electrons while exciting the sample. BSE electrons, which leave the specimen interact with components of the specimen chamber and generate SE_3. While SE_1 and SE_2 give information about the inherent properties of the material, SE_3 depends on the features of the SEM specimen chamber. These three SEs are responsible for compositional and topographic structures shown on SEM images. The image formation strongly depends on the secondary electron emission and the detector system.

4.3.6 Information of SEM Images

Scanning electron microscopy images give information about specimen properties when differences in the interaction of the beam electrons between a specimen feature and its surroundings create a contrast in the BSE and/or SE signals. This is possible due to a variety of contrast mechanism.

The number effect means the contrast generated by different numbers of electrons leaving the sample at different locations due to the changes in the specimen characteristics at those positions. The trajectory effect gives information about the contrast resulting from differences in the paths the electrons travel after escaping from the specimen. The energy effects are of interest when the contrast is generated BSE and SE energy distribution. High-energy BSE are used to image contrast mechanisms such as atomic number contrast or crystallographic contrast whereas low-energy SE escape from a flat near surface region and contain information about the surface.

4.3.7 Interpretation of SEM Images of Compositional Microstructure

The dependence of electron backscattering upon atomic number (Fig. 20) leads to a number effect, which gives information about the compositional microstructure of a sample. To produce an unaltered atomic contrast image, the sample should be as flat as possible so that the topography of the specimen does not modify the backscattering. The generated image will illustrate different regions with progressively higher grey levels, which indicates the different components of the sample. The higher the atomic number, the lighter gets the grey levels.

With the Everhart-Thornley detector secondary electrons and backscattered electrons, which are directly emitted into the solid angle defined by the scintillator are captured. The higher the atomic number of the component in the sample, the brighter the locations appear in the SEM image.

Imaging the topography of specimens is very useful to gain information on the size and shape of topographic features.

A focused electron beam scans the specimen and a mixture of BSE and SE signals are generated, which are displayed in a grey-scale image. Even an untrained observer can understand the shape of the three-dimensional sample due to the pattern of highlights and shading in the SEM/E-T (positive bias) image. The appearance of the 3D image produced with SEM/E-T is very similar to the view that would be obtained if the object was viewed with a simple light source and the human eye. This is called the light-optical analogy. This is very important to understand to avoid incorrect image interpretation of topography. The E-T detector is placed on the wall of the specimen chamber asymmetrically positioned to the beam axis (Fig. 24). The interaction of the electron beam with the sample results in BSE and SE signals. SE_1 are produced by the beam electrons entering the specimen, and SE_2 are produced by the exiting BSEs. BSE that strike the scintillator are always detected with E-T detector. A small positive bias on the cage attracts SEs with high efficiency to the detector. **[13]**

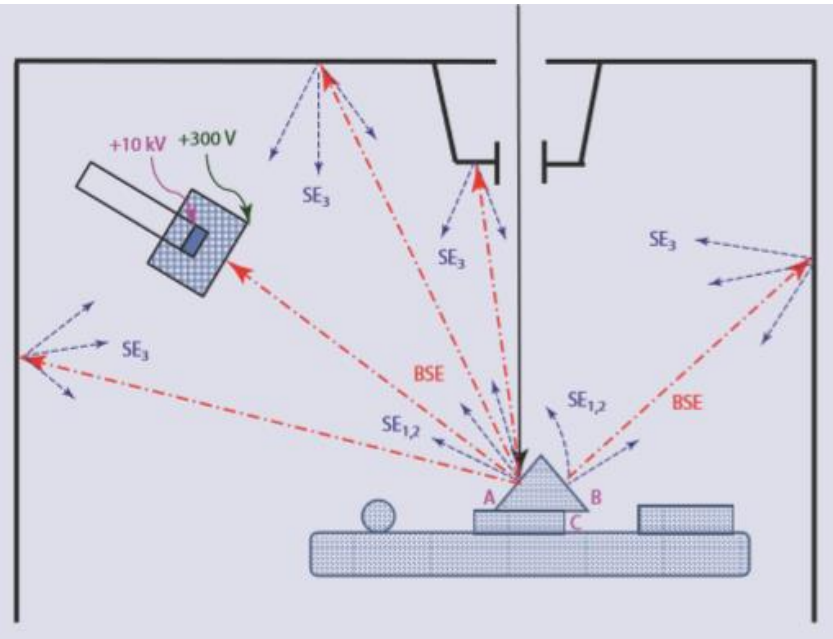

Figure 24 - Various sources of signals generated from topography are illustrated: BSEs, SE_1 and SE_2, and remote SE_3 are collected by the Everhart– Thornley detector. ***[13]***

4.3.7.1 Resolution Problems

The resolution means the minimum spacing, at which two features of the specimen can be observed as distinct and separate. The lower limit of the resolution is defined by the size of the beam. Thus, it is necessary to adjust the beam diameter to the size of the features of interest. Not all SE and BSE signals have the same spatial properties. There are different classes of BSE and SE as already mentioned above. SE_1 are generated when the beam enters the sample and the electrons are localized within a few nanometers around the impact sites. The electrons carry high energies and give information about fine scale features. These are only the true secondary electron signals and represent a high-resolution signal. Some electrons from the electron beam, which scatter and travel within the specimen result in backscattered electrons. The low-loss component BSE_1 constitutes to another high-resolution signal. Secondary electrons, which are generated due to BSE are also high- resolution SEs and are called SE_2. However, BSE electron, which loose more and more energy by traveling through the sample get delocalized and are not able to give information about the specimen in the beam impact area (low resolution signal). To generate useful high-resolution signals it is important to separate low and high-resolution signals from each other.

4.3.8 Generation of X-rays in the SEM Specimen

X-rays are generated beneath the surface in the beam-specimen interaction volume when the electron beam hit the sample. The energies from the X-ray photons are specific for the elements inside the sample. These are characteristic X-rays and are used in scanning electron microscopy for elemental investigations. The X-rays, which are analyzed in SEM are usually between 0.1 and 20 keV. Photons, which do not contain information about the specimen elements constitute to the continuum spectrum. Thus, there are existing two different types of X-rays, which are generated, when the specimen is irradiated with an electron beam: the continuum X-ray (Bremsstrahlung) and the characteristic X-rays.

4.3.8.1 The Production of Continuum X-rays

The continuum X-rays are also known as bremsstrahlung or braking radiation. This type of radiation arises due to the deceleration of the beam electrons in the Coulombic field of the specimen atoms. The Coulombic field is formed due to the modification of the positive field of the nucleus by the negative field of the bound electrons. In other words, the beam electrons experience repulsion due to the negative charge cloud around the atomic electrons. The loss of electron energy ΔE due to the deceleration of the beam electrons results in the emission of photons (Eq. 8).

Equation 8 – Definition of electron energy loss ***[9]***

$$\Delta E = h\nu$$

ΔE *…loss in electron energy*
h *…Planck's constan*
ν *…frequency of electromagnetic radiation*

Due to the random interaction of the beam electrons with the specimen the bremsstrahlung can have any energies from zero up to the energy of the incident beam (Duane-Hunt-limit) resulting in a continuous spectrum. An X-ray spectrum contains continuous and characteristic components, which are generated inside the interaction volume of the specimen.

For the analytical X-ray spectroscopy the intensity of the continuum radiation is very important. It forms a background under the characteristic radiation. Generally, the intensity of continuum rises with increasing beam current, atomic number of the element and beam energy. The rise in intensity due to atomic number occurs because of the increased Coulombic field of the nucleus.

When a photon with specific energy is generated it is not possible anymore to distinguish between continuous or characteristic radiation. Hence, the background intensity occurring from the continuum process happening at the same energy as the characteristic radiation, is used as a limit for the minimum amount of an element that can be detected. However, the continuum contains information about the average atomic number of the specimen and, therefore, about the overall composition because different elements in the specimen generate different amount of continuum intensity at all X-ray energies.

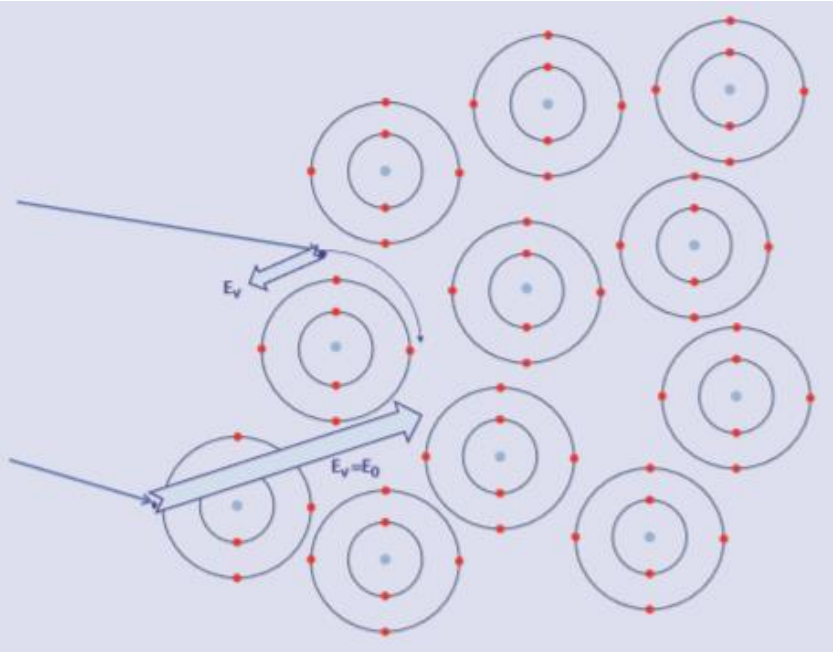

Figure 25 - Breaking radiation process (Bremsstrahlung) giving rise to X-ray continuum. ***[13]***

4.3.8.2 Production of Characteristic X-rays

An incident beam electron interacts with an inner shell electron of the specimen and ejects an electron from a shell. The incident electron leaves the atom at lower energy. The lost energy called E_k is the binding energy of the electron to the K shell and the ejected electron carries a kinetic energy of a few eV to several keV depending on the interaction. Thus, the atom is left in an excited state due to the missing inner electron, but only for about 1 ps. Then, the atom is converted to its ground state due to the filling of the electron hole in the inner shell with electrons from outer shells. The energy emitted in form of photos in this step is characteristic for specific elements. However, the excess energy can be released in two different ways (Fig. 26). In the Auger process the excess of energy leads to the ejection of another outer shell electron with specific energy. In the characteristic X-ray process the excess of energy is released as photon of electromagnetic radiation. **[9]**

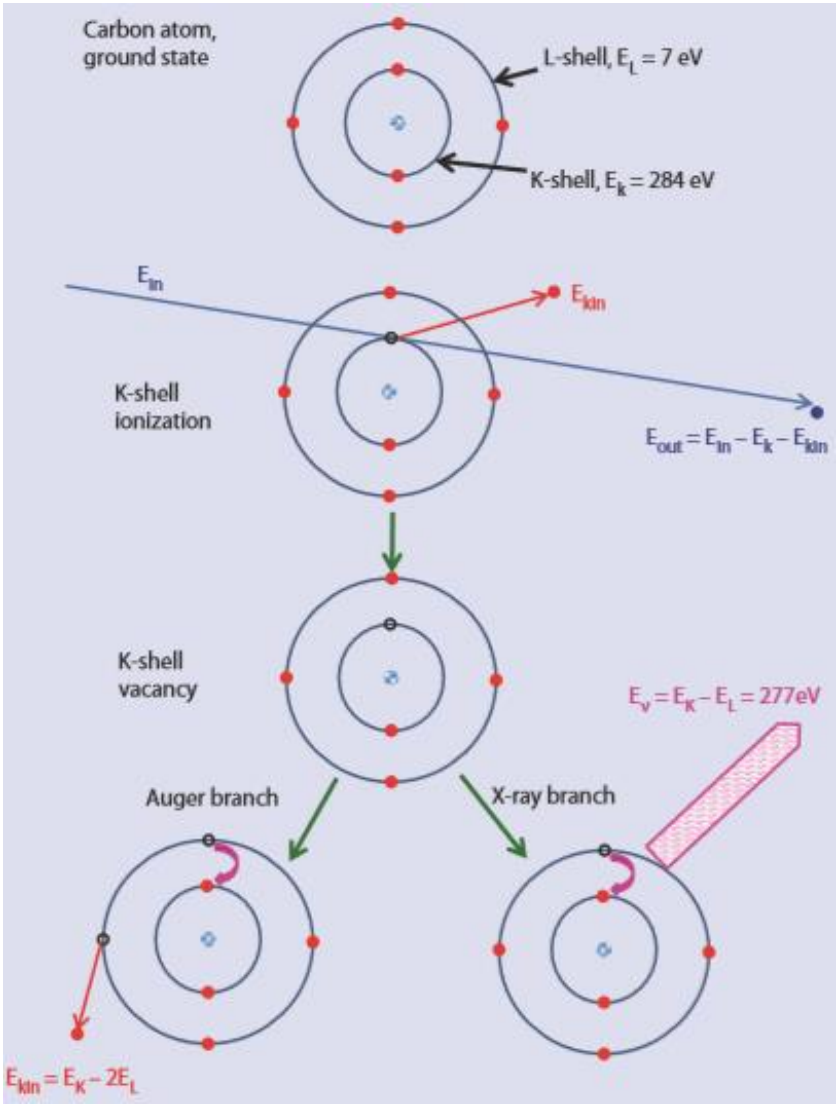

Figure 26 - X-ray generation process. ***[13]***

4.3.9 Energy-Dispersive X-ray Spectrometry Process

For the chemical analysis in scanning electron microscopy the energy and intensity distribution of the generated X-rays are detected and measured.

The first step of the energy dispersive X-ray spectroscopy (EDS) process with a semiconductor detector is the photoelectric absorption of an X-ray photon in the active mass of the silicon semiconductor. The energy of the incident photon is transported to a bound inner shell electron of the atom which is ejected. The resulting kinetic energy is the difference of the photon energy and the binding energy (shell ionization energy) of Si.

The ejected photon is inelastically scattered within the semiconducting material silicon. This energy loss leads to the promotion of bound outer shell electrons to the conduction band of the semiconductor and, subsequently, to the formation of positively charged holes in the valence band. The free electrons in the conduction band move between the entrance surface electrons and the rear surface electrode across the silicon crystal due to the applied potential. In the same time the positive holes move to the opposite side,

which leads to the collection of electrons at the positive electrode of the back surface of the EDS detector. The generation of one electron hole pair requires approximately 3.6 eV. Thus, the number of charge carries is proportional to the original energy of the photon (Eq. 9).

Equation 9 – Energy of photons ***[13]***

$$n = E_p/3.6\ eV$$

E_p *…energy of photon*

eV *…electron volt*

The name energy dispersive spectrometry is based on the capability of the detector to respond to any photon energy form 50 eV to 30 keV and more.

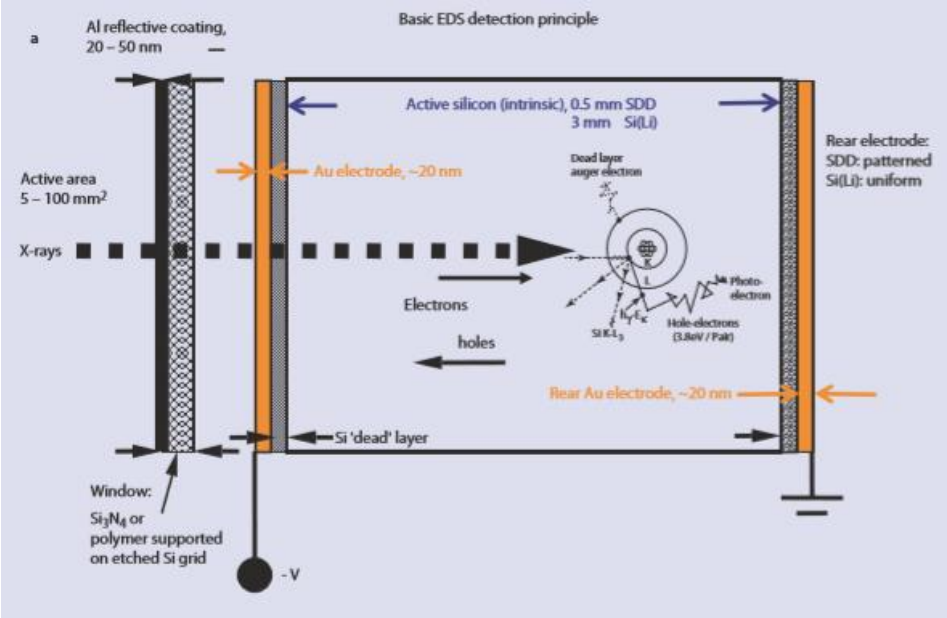

Figure 27 - Principle of photon measurement with Si (Li) detector (SSD-EDS). ***[13]***

The first type of EDS was the lithium-drifted silicon detector containing a uniform front and back surface. Nowadays, the silicon drift detector (SSD-EDS) is preferable used (Fig. 28).

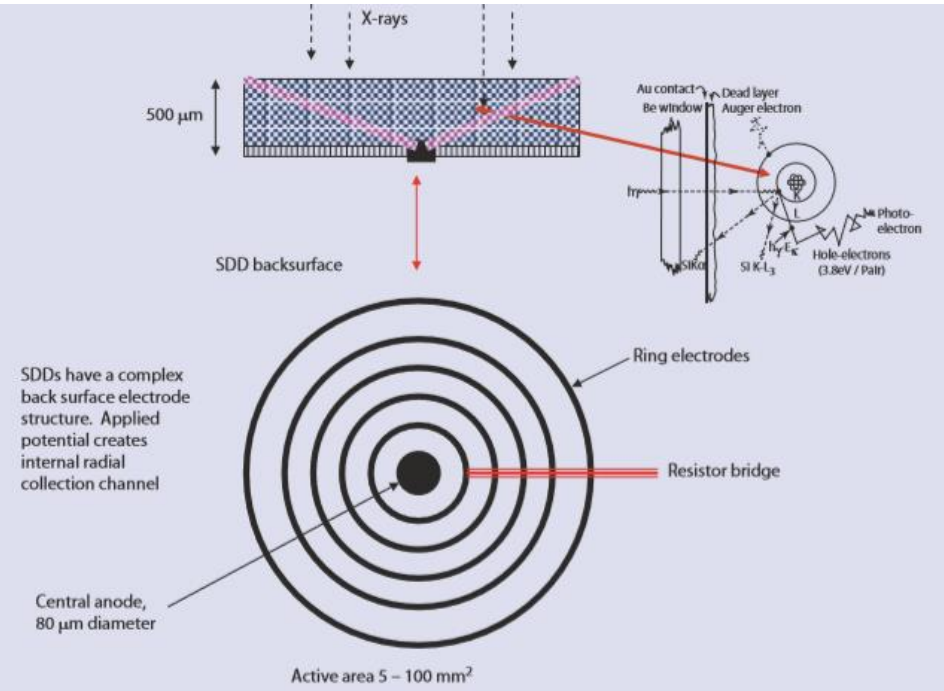

Figure 28 - Silicon-drift detector design for EDS. ***[13]***

The SDD-EDS uses the same detection principle with a uniform front surface, but the backsurface electrode consists of a complex pattern of nested rind electrons with small central anodes. Various potentials are applied to the ring electrodes, which generate an internal collection channel. This channel is responsible for bringing the electrons, which are deposited anywhere in the detector to the central anode, where they are collected. For the determination of the photon energy a sensitive and sophisticated electronic system is used to measure the charge deposited in the detector, which works automatically with computer control. There are only a few numbers of parameters, which can be adjusted by the user. **[13]**

4.3.10 Qualitative X-ray Analysis

The first step of the investigation of an unknown specimen is to identify the elements which are present. This process refers to the qualitative analysis. The detection limit of EDS systems in bulk materials is about 0.1 w%. The spatial resolution for SEM-EDS systems is about 2 µm.

Due to the short time of measurement (10-100 s) of the total spectrum from 0.1 to the beam energy a rapid evaluation of the components in the specimen is possible. The entire X-ray spectrum is recorded at every specimen location and, thus, a qualitative analysis at every measured location is possible. The poor energy resolution of EDS leads to frequent spectral interferences and makes it impossible to separate the members of X-ray families at low energies.

For the identification of unknown elements it is necessary to consider the appearance of K, L and M families in the EDS spectrum as a function of the position in the energy range of 0.1 to 15 eV. A useful method to identify unknown EDS spectra is to study spectra from pure elements.

For photon energies larger than 3 eV the energy separation of the members of a family of X-ray peaks is high enough that more than one peak can be observed even if they are not completely resolved (Cu and Sn). If the photon energy is between 2 and 3 keV the family members α and β results in one peak. This happens when the energy difference falls below the resolution of the EDS system (Si K family).

If the beam energy is high enough to exceed the critical excitation energy all X-ray peaks will be observable on the spectrum. Thus, for a qualitative analysis all peaks for each element must be in the ED spectrum. So if a high-energy K- peak is recorded also a low-energy L- peak must be observed for this element and if a high-energy L- peak can be seen in the spectrum also a low-energy M- peak corresponding to the element must be present.

Most modern energy-dispersive X-ray spectroscopy are based on a routine for automatic qualitative analysis. The qualitative analysis means a series of conditional test for recognizing and classifying peaks. In general, four basic steps are performed for the qualitative investigation. First, the background is removed by spectral filtering and background modeling software. In the next step the peak positions are determined, and the elements are assigned to the corresponding peaks from look-up tables. At last the peak stripping is performed. Therefore, the intensity for the determined elements including small and artefact peaks is stripped from a candidate peak to show if there are other elements present in this peak region (overlapping peaks). Naive automatic qualitative analysis systems report all possible elements peak within an energy range of for example 25 eV of a candidate peak. Peak stripping is not available for all EDS systems, so the analyst has to set guidelines manual.

4.3.11 Quantitative X-ray Analysis

The first step for the quantitative analysis with EDS is to define the problem. If the aim of the measurement is clear the correct analysis procedure including measurement parameters like current beam, acceleration potential and analysis time can be selected.

In the next step, the qualitative analysis is performed to determine the elements present in the sample. If not all elements can be found, an accommodation must be performed in the correction schemes of the system. Then, the necessary samples and standards have to be selected. The specimen of interest must be conductive, otherwise, the electron beam is not stable and moves from the selected position. For the standard a homogeneous substance with known composition is used.

Afterwards, the sample must be prepared for the measurement. A flat polish with scratches less than 0.1 µm to avoid height differences is produced. Furthermore, surface layers like oxide layers have to be removed to obtain a trustful result of the measurement. To ensure the conductivity the sample is mounted in a conductive material or coated with a conductive material. Then, the sample is placed onto the sample holder.

For the quantitative analysis the X-ray intensities are measured. Therefore, the X-ray spectrum of the specimen and standard under defined conditions is recorded. Then, the background must be removed from the measured characteristic X-ray intensities that the analyst can use the ratio of the measured intensities of the sample and the standard (k ratio) to determine the composition of the specimen. For minor and trace elements the background is a significant part of the characteristic peak intensities, which results in inaccurate quantification (detection limit 0.1 w%). To determine the value of the background, a linear interpolation is placed between two measured background positions A and B. The relatively poor resolution of the EDS is a problem for the determination of trace elements after subtracting the background.

The intensity of the recorded peaks is determined from the number of counts present in a region of interest (ROI) located around the peak centroid. The ROI contains counts from characteristic lines and background. Thus, the background must be removed to determine the k ratio.

The matrix effects, atomic number (Z), X-ray absorption (A) and X-ray fluorescence (F) are important for the correction for X-ray analysis.

For the atomic number correction the backscattering and the stopping power component must be considered. The number of backscattered electrons increases with the increasing atomic number. The problem is that the electrons are ejected from the specimen and do not generate X-rays. Thus, a correction must be made if the sample has a different mean atomic number than the standard to measure the correct X-ray intensity.

The stopping power means the loss of energy by the incident beam electrons per unit of mass entered in the sample. The mass, which is penetrated by the incident beam rises with increasing atomic number and, thus, more X-rays are generate from higher Z. This correction type has the opposite sense of the backscattering correction. The sum of these two corrections is the atomic number correction Z.

X-rays, which are produced in the specimen move everywhere within the sample and could be absorbed. For that reason, the X-ray absorption correction is necessary.
A second generation of X-rays can be produced by the X-rays generated from the primary electron beam. This process is called fluorescence. It occurs when the characteristic X-rays from one element have an energy higher than the ionization energy of an electron shell in another element present in the sample. Therefore, fluorescence correction is necessary.

4.3.12 Sample Preparation of Metals

A proper sample preparation is fundamental for an accurate analysis of the specimen. The preparation must be adjusted to the aim of the measurement. For the topographic investigation only little or no preparation steps are necessary. However, the sample must be carefully cut into smaller pieces to fit into the measurement chamber if necessary and it could be cleaned with solvents or with an ultrasonic cleaner. Thereby, the real surface may not be damaged.
For the microstructural and microchemical analysis the samples are sectioned by any sort of saw. Thereby, it is also important not to damage the sample. If the selected part of the sample is too small or difficult to fix on the sample holder, they are embedded in a mounting material. It must be kept in mind that the sample has to be conductive for the measurement and that the mounting materials should not smear across the sample surface while polishing. However there are some conductive mounting materials, but they are more expensive, and it is more difficult to work with it. Also the height of the polish must be considered (maximum of 1- 2 cm).
Then, the final polishing steps start. First, the sample is grinded with relatively coarse abrasive papers. Thereby, the particle size of the grinding papers gets continuously smaller. These grinding steps are performed under water to prevent heating of the sample. The final grinding ends at a particle size smaller than 1 µm. At last, a thin layer of a conductive material must be coated onto the sample. Common methods are gold or carbon sputtering.
It must be kept in mind that there is no general sample preparation, which can be applied for any materials. It must be adjusted to the properties of the material (hard/soft or rough/flat). **[9]**

4.3.12.1 Focused-Ion-Beam Sample Preparation

For the focused-ion-beam preparation a narrow beam of positively charged particles raster across the sample surface and generate secondary and backscattered electrons, ions, photons and neutrons. These particles can be used for imaging and investigation of the sample. A typical FIB machine uses a gallium liquid-metal as ion source operating at 2-30 kV, 1 pA- 20 nA beam current, a minimal spot size of 5 nm and a spatial resolution of 5-7 nm. **[14]**
One advantage of the FIB method is that it enables a precise cut or cross section with the ion beam (1- 200 µm width and 10-30 µm depth). Furthermore, due to the generation of secondary and backscattered electrons immediate imaging is possible. This method is best used for the structural

investigation of metals and alloys. Grain boundaries, film growth, voids and other defects can be revealed by FIB sample preparation. **[9]**

4.4 Binary Phase Diagrams of Alloys

For the correct interpretation it should be known that the designation of the different phases in binary phase diagrams is based on the crystal structure. It was decided to use Greek letters for the phases with different composition and to name certain crystal structures with certain letters like β for b.c.c and γ for γ-brass type of structure. For phases with defined or nearly defined composition the chemical formulas are used as designation. Solid solutions are named after the base element with the chemical symbol in parentheses.

For better understanding only the one-phase fields are lettered. Characteristic composition like eutectics or solid solutions are specified by atomic and weight percent. Dashed curves mean that the phase boundary is not reliably or investigated at that time. **[15]**

4.4.1 Copper-Lead

The phase diagram of copper-lead shows a miscible gap in the liquid state.

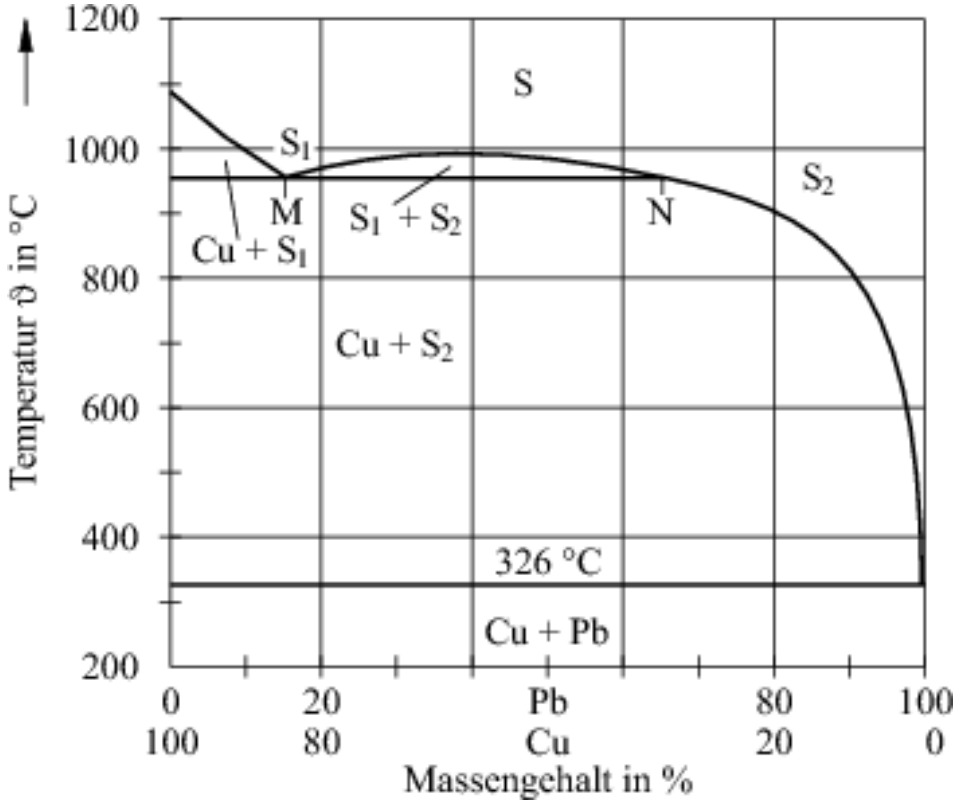

Figure 29 - Binary phase diagram of copper-lead alloy. ***[16]***

Between M and N the melt decomposes into two melts of different composition. At the monotectic point these two melts have a composition of M and N. At the monotectic point following reaction happens.

$$S_1 \rightarrow S_2 + copper\ crystals$$

The melt S_1 changes due to the precipitation of elemental Cu to S_2. Further cooling leads to an enrichment with Pb of the melt until 326 °C. There, the melt solidifies with 0.06w% Cu (copper-lead eutectic). In the solid-state no solubility exists.

Alloys with a composition left from M primarily precipitate copper primary crystals while the melt is enriched with Pb until the weight percent M (monotectic point) is achieved. Above N no monotectic reaction occurs anymore.

Copper-lead alloy with 2-25% Pb content are preferable used as bearing metal. Lead is embedded in the copper skeleton. **[16]**

4.4.2 Copper-Tin

Figure 30 shows the phase diagram of the binary system copper-tin. At liquid state Cu and Sn are completely miscible (798 to 520 °C). At solid state at 520 °C the solubility of Sn in Cu is about 15.8 wt%. Further cooling leads to a reduced solubility of Sn in Cu. This means at 170°C the solubility in not higher than 0.74 wt% Sn and practically zero at 100 °C. This results in the ability to precipitate the copper-tin alloy. However, this has only theoretical meaning at temperatures below 525 °C due to the diffusion inertia of Sn. Therefore, cold forming and long annealing times of 1000 to 2000 h would be necessary. The solubility of tin below 520°C remains constant with about 15.8 wt%. Thus, commercial copper- tin alloys of maximum 9 wt% Sn are available in form of α- mixed crystals (solid solution). Copper-tin alloys with a tin content >6 % show an α- phase and an α+δ- eutectoid. **[17]**

In the range of 15.8 to 39.9 wt% Sn above 500°C β,γ, δ and ε phases are existing. β and γ phases are crystallographically very similar (b.c.c). The crystal structure of δ is analogous to γ-brass ($D8_2$) and the ε phase is orthorombic. The solid solubility of copper in tin at the eutectic temperature is 0.006 wt% Cu. **[15]**

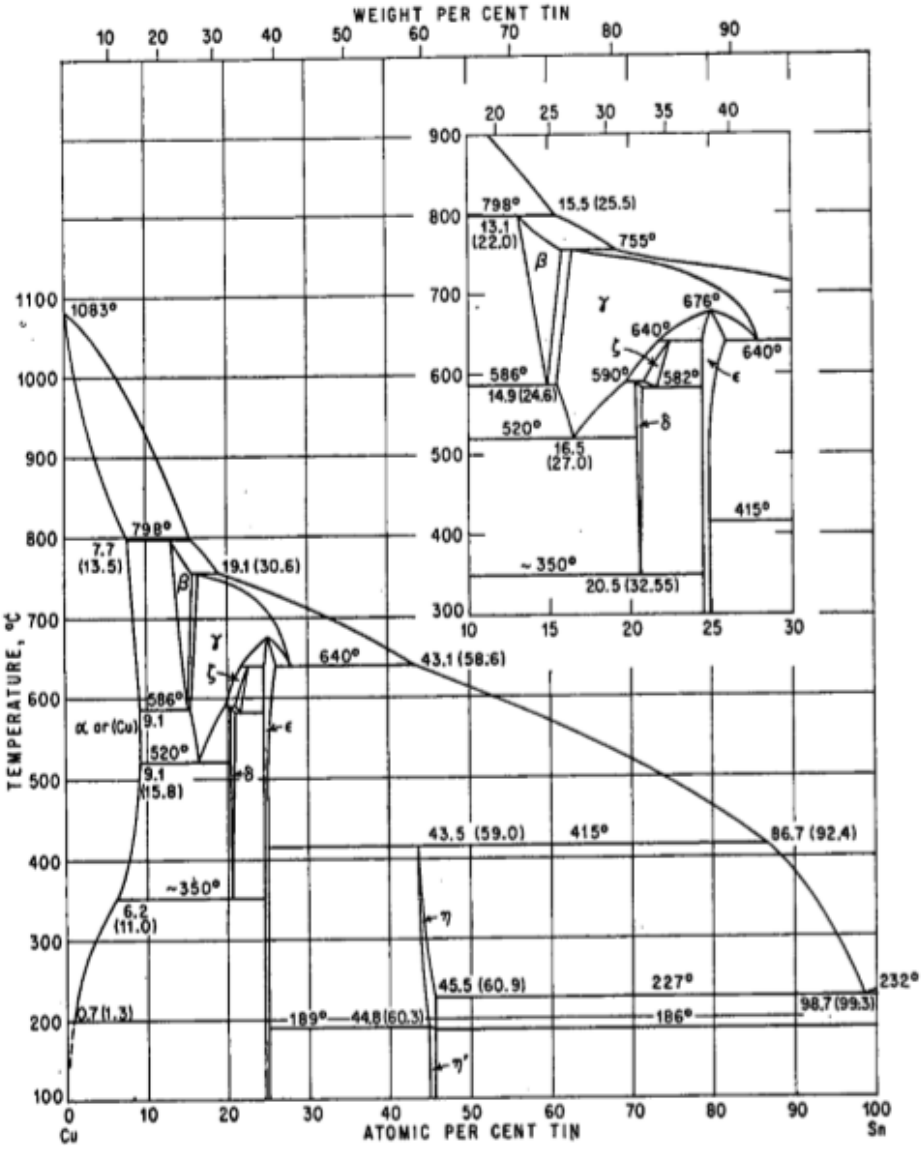

Figure 30 - Binary phase diagram of copper-tin alloy. ***[15]***

5 Experimental Part

In Table 1 the used chemicals and equipments for layer preparation and investigation are listed.

Table 1 -Chemicals and Equipment used for the preparation and analysis of the metallic single and multilayer structures.

Cutting equipment	Sectom-50, Struers
Embedding media (Method 1)	EpoFix Hardener and Resin, Struers
Polishing equipment	Tegramin-25, Struers
Polishing plates (Method 1)	Waterproof SiC, FEPA P #180, grain size 82 µm, Struers MD- Largo, Struers MD- Dac, Struers MD- Nap, Struers MD- Chem, Struers
Polishing agent (Method 1)	DiaPro Allegro/Largo 9 µm, Struers DiaPro Dac 3 µm, Struers DiaPro Nap B 1 µm, Struers OP-S NonDry, 0.04 µm, Struers DP- Lubricant- Blue, Struers DP- Spray ¼ µm, Struers
Embedding media (Method 2)	Caldofix Hardener and Resin, Struers
Polishing plates (Method 2)	Waterproof SiC, FEPA P #800, 22 µm Waterproof SiC, FEPA P #1200, 15 µm Waterproof SiC, FEPA P #2000, 10 µm Waterproof SiC, FEPA P #4000, 5 µm MD- Mol, Struers
Polishing agent (Method 2)	DiaDuo-2, 3 µm DiaDuo-2, 1 µm DP-Suspension P, 0.1 µm
SEM-EDS	Zeiss Ultra™ 55 with Gemini technology, Software Smart SEM- [Ultra] Octane Elite EDS System, Amatek Silicon Drift Detector (active area 70 mm^2), Amatek Software EDX Genesis
Method for Monte Carlo simulation	Casino v2.42
Broad-ion beam milling	Gantan

The task was to develop a measurement method for the qualitative and quantitative analysis of single and multilayer structures deposited by physical vapor deposition with an unbalanced magnetron system. The focus was the investigation of the quantitative composition of each single layer within the multilayer system with high depth resolution. For the investigation CuPb23Sn3, CuPb2, CuSn6 and Cu9Pb films were measured as single layers deposited on a stainless-steel sheet and within the graduated layer system with SEM-EDS. Atomic absorption spectroscopy measurements (AAS) of selected single layers were used as reference values to assess the accuracy of the EDS results and to possibly optimize the EDS analysis by various correction modes.

Table 2 - Investigated layers of the single layers CuPb23Sn3, Cu9Pb, CuSn6 and CuPb27 deposited on stainless steel sheets. The table shows whether the deposition was performed on a preheated ("warm start") or cold ("cold start" at room temperature) substrate and which targets were used to deposit the desired alloy film.

Sample name	*Layer composition*	*Substrate temperature when deposition starts*	*Targets for sputter process*
PVD03-206	CuSn6	warm start	alloy target of CuSn6
RR60	CuSn6	warm start	alloy target of CuSn6
RR32	Cu9Pb	cold start	two elemental targets of copper and lead
RR28	CuPb27	cold start	two elemental targets of copper and lead
RR69	CuPb25	warm start	two elemental targets of copper and lead
RR27	CuPb23Sn3	cold start	alloy target of CuSn6 and two elemental targets of copper and lead
RR29	CuPb23Sn3	cold start	alloy target of CuSn6 and two elemental targets of copper and lead
RR34	CuPb23Sn3	warm start	alloy target of CuSn6 and two elemental targets of copper and lead
RR57	CuPb23Sn3	warm start	alloy target of CuSn6 and two elemental targets of copper and lead

For the investigation of the graduated layer system deposited on M42 steel slices with a diameter of 30 mm and 3 mm thickness, sample *RR43*, *RR44* and *HTC-877* were measured. The deposition of these graduated layer systems was started on a preheated substrate and each single layer of the graduated system was successively sputtered by using the targets corresponding to the single layer deposition shown in Table 2.

5.1 Deposition Process of Single Layer Films

For the manufacturing of the single layers, stainless steel sheets were coated by physical vapor deposition with an unbalanced magnetron system with the desired alloys (CuPb23Sn3, CuSn6, CuPb27 and Cu9Pb). The stainless-steel sheets were cleaned within the magnetron system by argon ion scrubbing before starting the sputtering process. The deposition was performed in a plasma environment of argon at 1 to 5 x 10^{-3} mbar and at temperatures between 150 and 250°C.

The deposition of some layers was performed on a preheated substrate (PVD03-206, RR34, RR57, RR60, RR43 and RR44). In this case the deposition started at a substrate temperature of about 200°C. The other layers were deposited on cold (room temperature) substrates (RR27, RR28, RR29, RR32), thereby the temperature during the deposition process increases to about 150°C. The layer thickness was regulated by the time of deposition and was for the single layers between 8 and 12 µm.

To obtain the desired composition of the alloy films elemental and alloy targets were used for the sputtering process. To generate the CuSn6 alloy an alloy target of the desired composition was used. For the deposition of CuPb27 and Cu9Pb two targets were used, an elemental target of copper and an elemental target of lead. To obtain the CuPb23Sn3 film an alloy target of CuSn6, an elemental target of copper to reduce the Sn content and an elemental target of lead was used.

5.2 Investigation of Single Layers

The analysis with SEM-EDS was performed by measuring the untreated surface of the deposited film and preparing a polished cross-section of the layer with Method 1 (Chapter 5.3).

In the first step, the untreated surface of the single layers PVD03-206, RR60, RR32, RR28, RR69, RR27, RR29, RR34 and RR57 was investigated by SEM- EDX. Therefore, a small piece of each coated sheet was fixed with an adhesive carbon tape onto the sample holder of the SEM. Then, the electron beam (7 keV and 15 keV) was focused directly on the surface of the coated sample. Due to various morphologies and shadings, from light grey to dark grey, different areas of the sample were selected and investigated by SEM-EDS to illustrate the local differences in composition. Furthermore, a relatively large area was scanned to obtain an average composition of the alloy system.

In the next step the polished cross-section of the single layers PVD03-206, RR60, RR32, RR28, RR69, RR34 and RR57 was investigated and quantified with SEM-EDS to reduce geometry effects. Therefore, the electron beam (7 keV and 15 keV) was focused on the polished cross-section. To maintain the electrical conductivity between sample and sample holder the hole cross-section was coated with approximately 7 nm of carbon and fixed onto the sample holder with an adhesive carbon tape.

All the layers were measured with Zeiss Ultra^{TM} 55 with Gemini technology at different magnifications, different acceleration potentials (7 and 15 keV) and by using different detector systems (HDASB, SE and InLens detector). To quantify the chemical composition of the deposited alloys the EDS System Octane Elite EDAX^{TSL} Lambda Spec (EDAX genesis) was used. Following correction modes were applied to improve accuracy: underground correction, Phi-Roh-Z and ZAF mode.

5.3 Sample Preparation of the Single Layers with Method 1

To generate a polished cross-section of the single layers, the coated stainless-steel sheets were cut carefully into small pieces and embedded with Epofix Struers (5:3 mixture of resin and hardener). Therefore, the small piece of the coated sample was fixed between a clip and placed in the middle of a plastic ring, where the embedding agent was carefully funneled and dried for 12 hours at room temperature. Then the coated sample was pulled out of the plastic ring and, finally, grinded with Tegramin 25 using different polishing sheets and lubricants as shown in Table 3. After the last step the polish was carefully rinsed with water and ethanol and finally dried (Fig. 31).

Table 3- Polishing steps of single layer preparation with Method 1.

	Polishing plate/ polishing agent	*Rotating speed/ rotational direction*	*Force*	*Time*
1st step	SiC Foil #180 and water	300 U/min and synchronous	25 N	2 min
2nd step	MD-Largo and DiaPro All/Lar.9	150 U/min and synchronous	35 N	5 min
3rd step	MD-Dac and DiaPro Dac3	150 U/min and synchronous	30 N	4 min
4th step	DP-Nap and DiaPro nap-B1	150 U/min and synchronous	15 N	1.5 min
5th step	MD-Chem and OP-S NonDry	150 U/min and counter rotation	15 N	1.5 min

Figure 31 - Polished cross- section of a single (above) and multilayer system (below).

5.4 Deposition Process of Graduated Layers

The deposition process of the graduated film system follows the same principle as for the single layer deposition. The layers (CuPb27, Cu9Pb, CuPb23Sn3 and CuSn6) were successively sputtered on a M42

(1.3247/ HS2-9-1-8) steel slice with 30 mm diameter and 3 mm thickness. Before the deposition the steel platelets were carefully cleaned within the unbalanced magnetron system by argon ion scrubbing. The thickness of each layer was controlled by the time of deposition.

Figure 32 - A graduated layer system deposited on a M42 steel slice (top view on graduated layer).

5.5 Investigation of Graduated Layers

For the investigation of the multi-layer system a polished cross-section of the coated slice was prepared with two different polishing methods (Chapter 5.6 and 5.7). To illustrate the morphology and structure of each layer different detection systems like HDASB, SE and InLens detector of the scanning electron microscope were used. An area of about 1 cm^2 each layer was scanned to determine the average composition of the film by EDS system. For these investigations an electron beam of 7 keV and 15 keV was scanned across the area of interest. To maintain the electrical conductivity between sample and sample holder the whole polish was coated with approximately 7 nm of carbon.

For the layer of HTC-877, additional to the large area scan for the average composition determination, line spectra were recorded. Therefore, horizontal lines were placed in a defined distance of each other from the beginning of the CuSn6 layer into the middle of the CuPb23Sn3 layer (Fig. 33). This measurement was performed to show the transition from one layer to another and if diffusion between the layers occurs. To visualize these results for an easier interpretation diagrams were created.

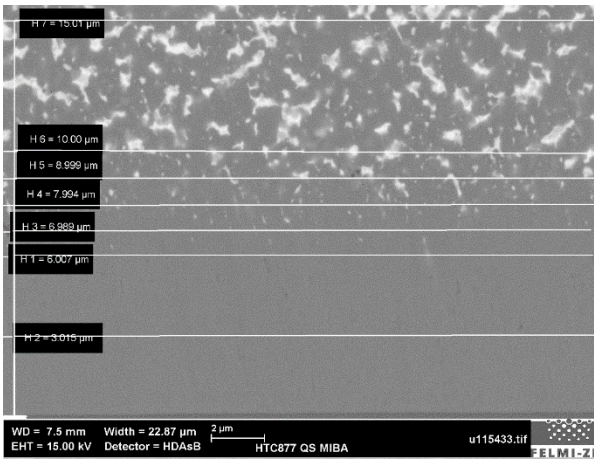

Figure 33 - Line spectra recording. Positions of the scanned lines starting from the beginning of the CuSn6 layer to the middle of the CuPb23Sn3 layer, 20 µm long lines. HDAsB- detection and 15 keV.

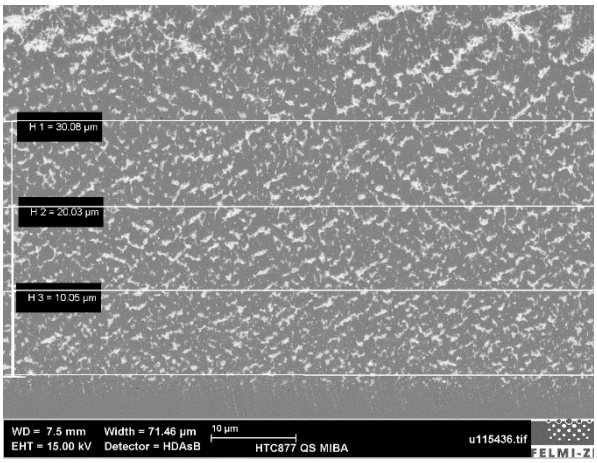

Figure 34 - Line spectra recording. Positions of the scanned lines within the CuPb23Sn3 layer, 70 µm long lines, HDAsB- detection and 15 keV.

5.6 Sample Preparation of Graduated Layer System with Method 1

First, the coated slices were cut with Sectom-50, Struers into smaller pieces to enable embedding the parts of interest for the investigation with SEM-EDS. Then the part of RR43 was cold embedded with Epofix, Struers (5:3 mixture of resin and hardener). Therefore, the coated sample was placed in the middle of a plastic ring with the side of interest facing the bottom of the ring and then the embedding media was carefully filled into the ring form uniformly around the sample to prevent moving of the part and bubbles. After 12 hours of drying at room temperature the embedded sample was pulled out of the ring form. In the next step, the prepared sample was grinded to obtain a planar measuring area, which is not oxidized or tarnished. The following five grinding steps are already described for single layer preparation in Table 3 (Chapter 5.3).

Before starting the polishing of the sample, it must be grinded with hand to remove supernatants and to deburr the sharp edges not to destroy the polishing plates.

It must be noted that the sample-head was carefully rinsed with water between the single grinding steps. After the mechanical grinding steps, the sample must be polished manually to avoid smearings and scratches across the whole multi-layer system. Therefore, the sample was slightly pressed onto the rotating polishing plate MD- Chem, Struers rinsed with some ethanol while moving the polish in the opposite direction. Then the polished sample is firstly rinsed with sufficient water, then with a detergent solution while wig across the probe with the fingers. In the next step, ethanol is used to clean the surface also by using the fingers. Finally, the sample is consecutively held under the flowing water and ethanol before being carefully dried with an air dryer (Fig. 31).

Then the prepared polish was examined under the light microscope. Due to some scratches from polishing and an oxide film on the Cu9Pb the polishing process of Method 1 starting from grinding step 2 (Table 3) was repeated.

5.7 Sample Preparation of Graduated Layer System with Method 2

The cut parts from the coated slices interesting for the investigation with SEM-EDS were cold embedded with Caldofix, Struers (1:3 mixture of hardener and resin) and dried for 1.5 h at 75 °C. Then the coated sample was grinded with Tegramin 25, Struers with different polishing sheets and lubricants in the following sequence: SiC foil 800, 1200, 2000 and 4000, Struers using water at 25 N for two minutes each. In the next step MD- Mol, Struers with DiaDuo 3, Struers, MD- Nap, Struers with DiaDuo 1, Struers and MD Nap 0.1µm, Struers with Diamant Suspension P, Struers at 15 N for 5 min each and MD- Chem, Struers with OP-S NonDry, Struers at 10 N for 5 minutes were used. In the last step the polish was carefully rinsed with water and ethanol and dried.

5.8 Sample Preparation with Broad-Ion Beam Milling

Layer RR69 with the desired composition of CuPb25 was prepared with broad-ion beam milling (Gatan). Therefore, the M42 steel substrate with the deposited film was cut (about 100x100x1 mm) and stick onto a tungsten blade (protection) with a silver adhesive (conductivity). Two ion guns are placed substantially perpendicularly to the edge of interest on specimen to be milled. Then the unprotected surface of the layer was successively removed with the argon ion beams to gain a smooth measuring area. Thus, the polishing preparation Method 1 and 2 and the broad ion beam milling preparation (BIB cut) can be compared.

5.9 Monte Carlo Simulations

Monte Carlo Simulations were performed to get an estimation how deep the electrons focused on the sample penetrate each layer. It also shows how much of the electrons are backscattered and the tread depth of the characteristic X-ray radiation. The simulation was carried out for Pb, Cu, Sn, CuSn6, CuPb27, Cu9Pb and CuPb23Sn3 with the program Casino v2.42. Therefore, 10.000 electrons were simulated, whereas for the presentation of the interaction volume 600 electrons were used.

6 Results and Discussion

The aim was the characterization and quantification of metallic single and multilayer structures. To better understand the multilayer structure, each single layer of the system was separately precipitated and carefully investigated.

6.1 Monte Carlo Simulation

The simulations show the difference in interaction volume of the primary electrons with the layer and the depth of origin of the backscattered electrons between the different elements and alloys of interest. The electrons of the incoming electron beam penetrate almost pear-shaped into the metal film (Fig. 35). Most of the electrons remain in the layer, the others are backscattered or generate characteristic X-rays for the characterization of the layer. These backscattered electrons do not arise from the lower part of the electron interaction volume but from the upper part. The higher the acceleration voltage of the incoming electron beam, the deeper is the depth of penetration of the primary electrons and the origin of the backscattered electrons. The simulations further illustrate that the penetration depth of primary electrons and the origin of the backscattered electrons depends on the atomic number of the elements. The higher the atomic number is, the heavier is the element and the lower is the depth of penetration of the electrons. Moreover, the density of the element influences the interaction volume (Chapter 4.3.5.1). The interaction volume of the primary electrons in elemental *copper* is smaller compared to the interaction volume in elemental *tin*. The origin of the backscattered electron is for both metals roughly the same of about 100 nm at 15keV. There the intensity of the generated characteristic X-ray radiation is the highest (75 to 100 nm). The origin of the backscattered electrons at an acceleration volume of 7 keV is closer to the surface than expected. Although tin has a higher atomic number, the interaction volume of Sn is higher compared to Cu. The reason could be the higher density of copper compared to tin.

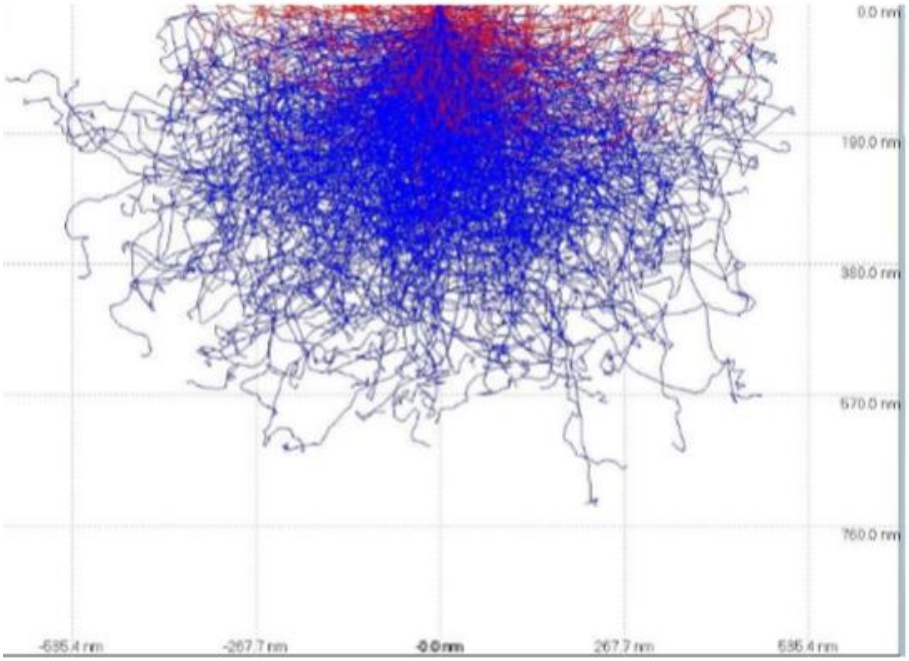

Figure 35 - Interaction volume of copper at 15 keV. The red lines show the backscattered electrons and the blue lines the primary electrons remaining in the copper layer.

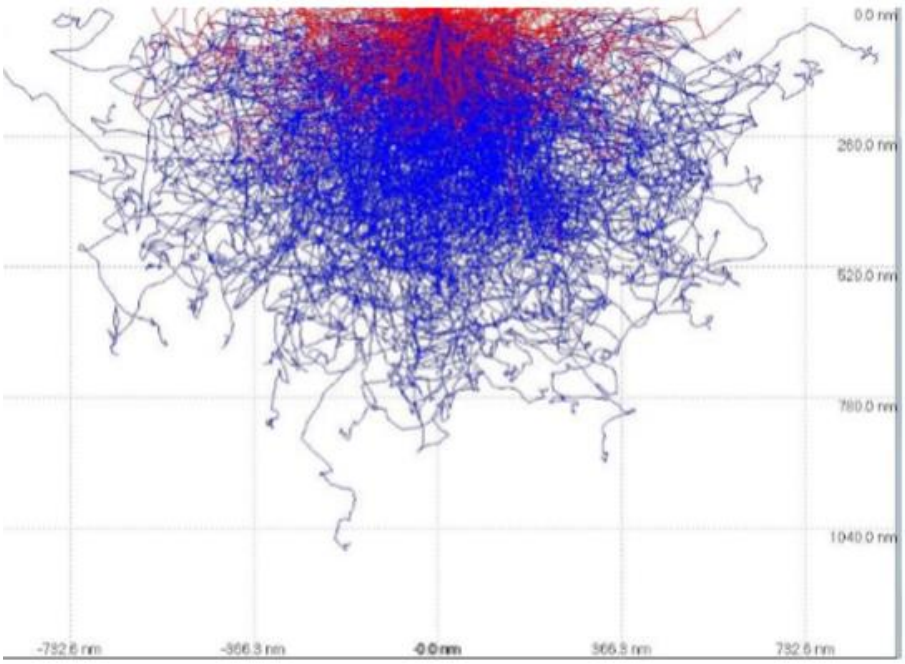

Figure 36 - Interaction volume for tin at 15 keV. The red lines show the backscattered electrons and the blue lines the primary electrons remaining in the tin layer.

For *lead* the electrons cannot penetrate as deep into the material as into copper or tin, because Pb is heavier than Cu and Sn and has a significantly higher density. The signal of the characteristic X-ray radiation with highest intensity comes from about 40 nm at 15 keV and about 17 nm at 7 keV. Nevertheless, compared to copper and tin the maximum of contribution of the number of backscattered electrons is a little broader.

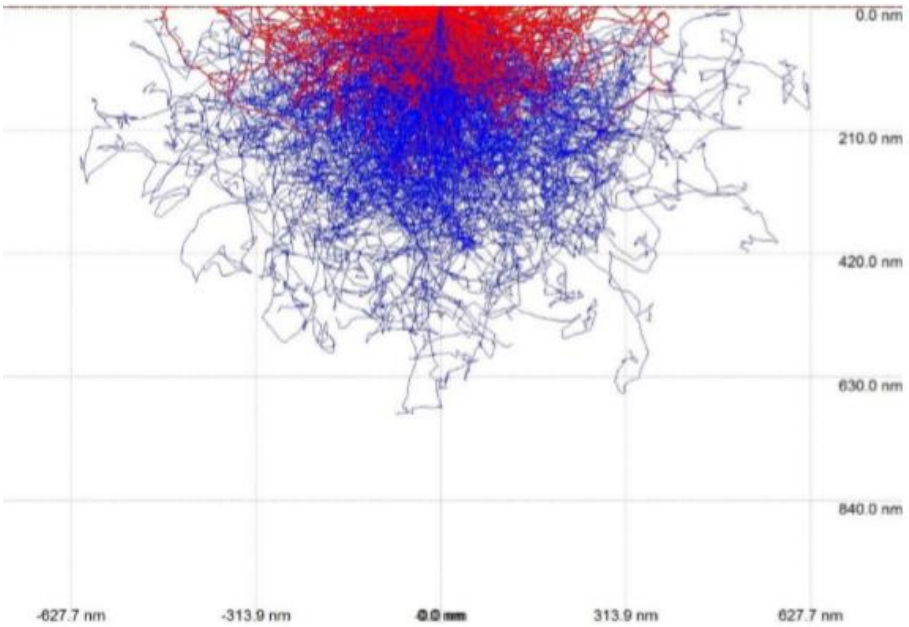

Figure 37 - Interaction volume of lead at 15 keV. The red lines show the backscattered electrons and the blue lines the primary electrons remaining in the lead layer.

Monte Carlo simulation also illustrates that the K- shell (K- shell doublet Kα and Kβ) is mostly excited due to its intensities. It shows from what depth and in which intensity the X-ray radiation from different shells is received. For copper signals from K and L- shell can be excited, depending on the excitation energy. The higher the atomic number of the element the higher is the required excitation energy. Elements heavier than tin already need an energy of more than 25 keV to excite the K-lines. However, acceleration energies of maximum 20-30 keV are enough to knock out electrons from the L- or M- shell. Thus, for tin electrons only from L- shell are excited with an excitation energy of 7 and 15 keV and for lead electrons from L and M shell are generated with an acceleration potential of 15 keV. With 7 keV only electrons from M-shell are excited (Table 4).

Table 4 – Energy of copper, tin and lead ***[18]***

Element	*Atomic number*	*Spectral line*	*Energy [keV]*
Copper	29	*Kα*	8.046
		Lα	0.928
Tin	50	*Kα*	25.271
		Lα	3.444
Lead	82	*Lα*	10.551
		Mα	2.342

For the *CuPb23Sn3* alloy most of the backscattered electrons arise from a depth between 70 and 80 nm at 15 keV. For 7 keV the maximum of contribution of generated backscattered electrons is broader compared to those of 15 keV.

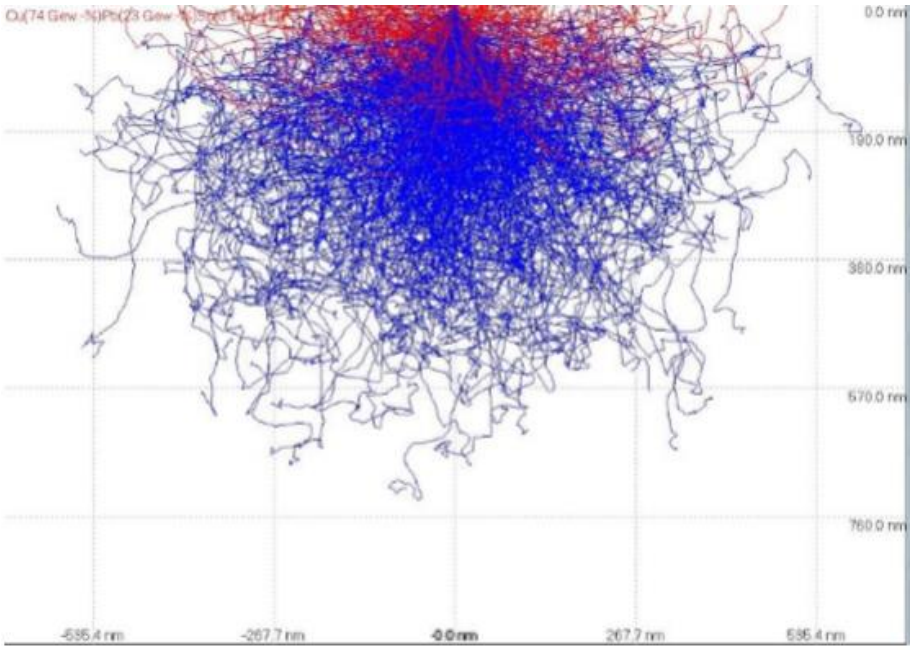

Figure 38 - Interaction volume of CuPb23Sn3 at 15 keV. The red lines show the backscattered electrons and the blue lines the primary electrons remaining in the CuPb23Sn3 layer.

Primary electrons penetrate deeper into the *CuSn6* film compared to the CuPb23Sn3 film due to the missing heavy lead in the alloy. The backscattered electrons arise from a depth of about 100 nm with 15 keV and 25 nm at 7keV. Thus, it is very similar to the elemental copper and tin. However, the maximum of contribution of the origin of the backscattered electron is broader compared to elemental Cu and Sn.

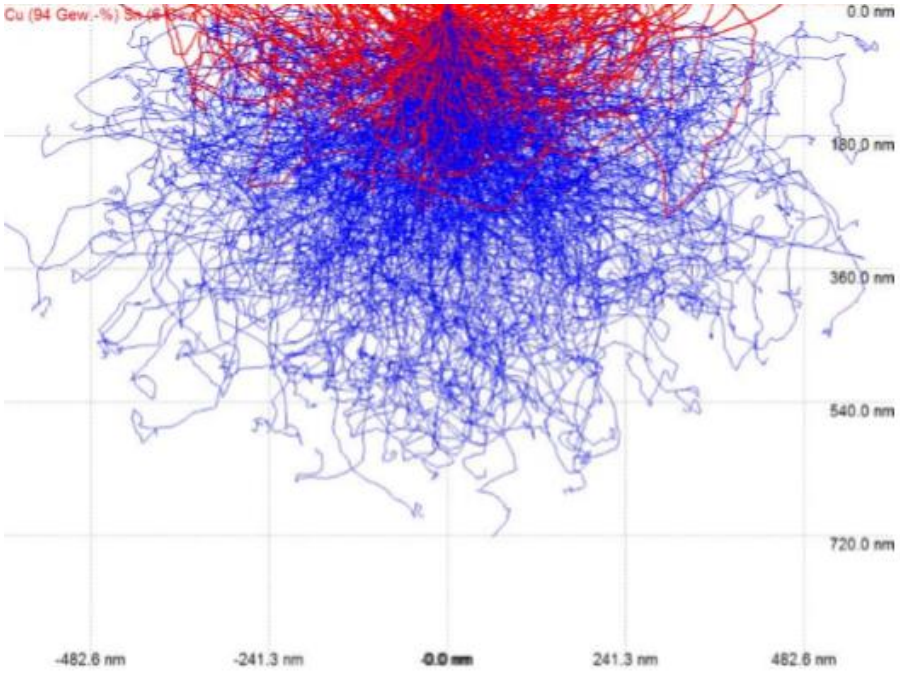

Figure 39 - Interaction volume of CuSn6 at 15 keV. The red lines show the backscattered electrons and the blue lines the primary electrons remaining in the CuSn6 layer.

The depth of the backscattered electrons for *Cu9Pb* at 15 keV is about 60 nm and for 7 keV about 20 nm and thus very similar to elemental lead, but the curve of the maximum distribution of backscattered electrons is broader.

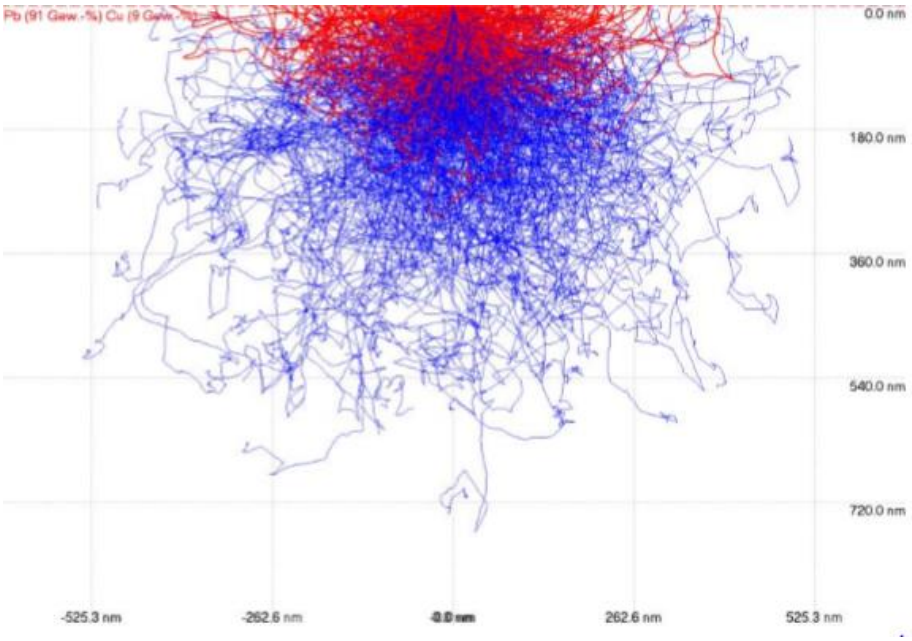

Figure 40 - Interaction volume of Cu9Pb at 15 keV. The red lines show the backscattered electrons and the blue lines the primary electrons remaining in the CuPb9 layer.

For *CuPb27* the backscattered electrons arise from about 80 to 90 nm depth with an acceleration potential of 15 keV and with 7 keV from 15 to 30 nm deep. The origin of backscattered electrons for CuPb27 is less deep compared to elemental copper due to the amount of Pb in the alloy.

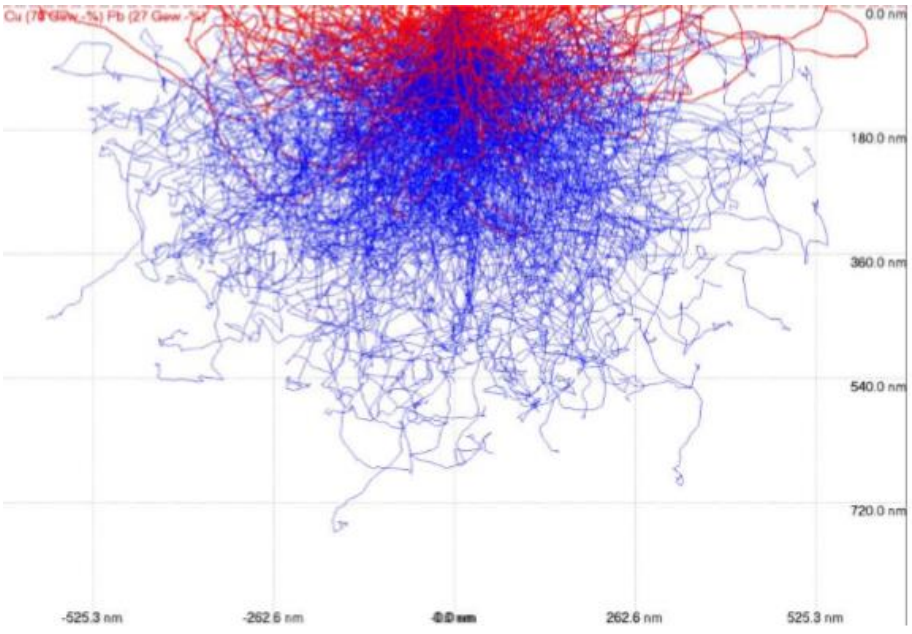

Figure 41 - Interaction volume of CuPb27 at 15 keV. The red lines show the backscattered electrons and the blue lines the primary electrons remaining in the CuPb27 layer.

6.2 Investigation of Single Layers

First, the untreated surface of the single layers deposited on a stainless-steel band PVD03-206, RR60, RR32, RR28, RR27, RR29, RR34 and RR57 was characterized and quantified by SEM-EDS at different magnifications and by using different detector systems. Layer RR69 was prepared with broad-ion-beam method to compare the results with conventional polishing methods. As correction modes the underground correction, the Phi-Rho-Z and ZAF mode were used to improve the accuracy of the measured results. In a second step a polished cross-section of the selected layers PVD03-206, RR60, RR32, RR28, RR34 and RR57 was equally investigated and compared with the results of the untreated surfaces. Moreover, the deposited films were quantitative analyzed with AAS and provided for reference values.

6.2.1 CuSn6 (PVD03-206)

The layer of sample PVD03-206 should ideally have the composition CuSn6, this means 94 wt% copper and 6 wt% tin. Unfortunately, the AAS measurements of the film are missing. Nevertheless, the layer was investigated in detail.

The deposition process was started on a cold (room temperature) stainless-steel sheet. This means that the temperature during the sputtering process starts at room temperature and reaches about 150 °C. However, the coating was quickly deposited, thus an amorphous and crystalline structure is expected.

6.2.1.1 Investigation of the Untreated Surface

At small magnification (Fig. 42) the film appears very uniformly and homogenous, however some smaller and larger precipitations, which resembles dots growing out of the surface are already detected. At higher magnification a granular structure, consisting of smaller and larger grains, is shown in Figure 43. Moreover, Figure 42 and 43 illustrate fine lines, which are aligned in one direction across the whole layer piece. These structures arise from the rolling process in the production of the stainless- steel band and are depicted trough the thin layer of CuSn6.

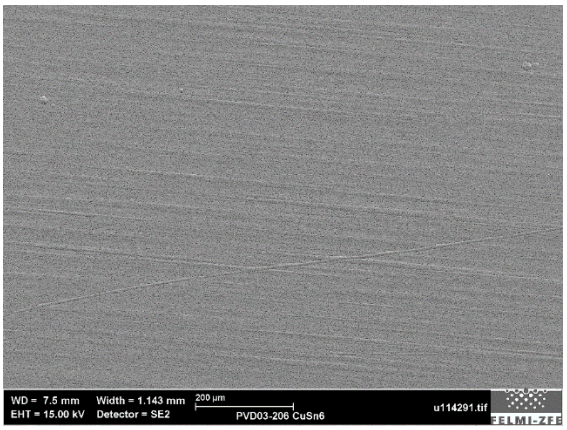

Figure 42 - CuSn6 (PVD03-206). This image shows the resulting lines from the production process of the stainless—steel band, which are depicted trough the thin layer of CuSn6. 15.00 keV and SE detection system.

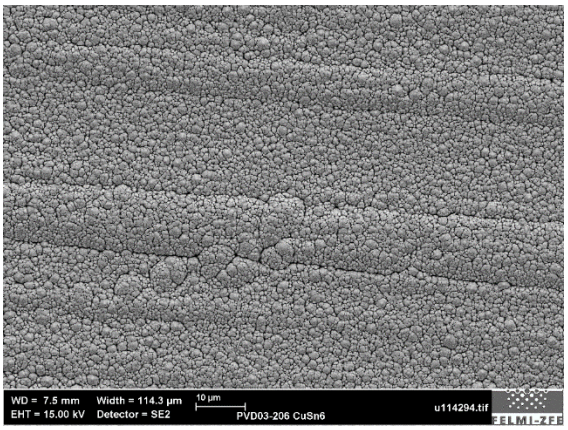

Figure 43 - CuSn6 (PVD03-206). Image of CuSn6 film, which illustrates smaller and larger grains. The lines resulting from the production process of the stainless-steel substrate are still visible. 15 keV and SE detection system.

In Figure 44 recorded at lower acceleration potential of 7 keV, the larger grains resemble the structure of layered pyramids or Romanesco broccoli. In contrast, the smaller dots have a smooth surface. Around the smaller and larger precipitation, grain boundaries are clearly recognizable.

According to the Cu-Sn phase diagram (Chapter 4.4.2), the deposited film consists of α-mixed crystals. The relatively homogenous solid solution of tin in copper crystallizes in a face-centered cubic lattice **[16]**.

Due to the fact, that the temperature of the plasma atmosphere during magnetron sputtering cannot be exactly determined, it is difficult to interpret the quantitative analysis of the deposited layer according to the phase diagram. The deposition of PVD03-206 was started on a cold substrate, therefore the temperature should not exceed 150 °C during the sputtering process. However, the layer was relatively quick deposited, thus, on the one hand a very crystalline and amorphous structure was expected. On the other hand, it was even more difficult to exactly determine the deposition temperature. For that reason, another layer of CuSn6 was prepared and investigated.

For the standard phase diagram of Cu-Sn the maximum solubility of Sn in Cu is about 15.8 wt%. At 170 °C the solubility is not higher than 0.74 wt% tin. The solubility of 6 wt% tin in copper is possible at temperatures of about 280 °C (Chapter 4.4.2). With magnetron sputtering process a solubility of 4 to 7 wt% of tin in copper at about 150 °C is possible.

It must be noticed, that these standard Cu-Sn- phase diagrams are valid for precipitation from the liquid phase and not from the gas phase, as it happens in the magnetron sputtering process. Therefore, deviations between analysis and phase diagrams are possible. To even show the fine grain boundaries around the larger and smaller precipitations in detail, an InLens detection image at an acceleration potential of 7keV was taken (Fig. 45).

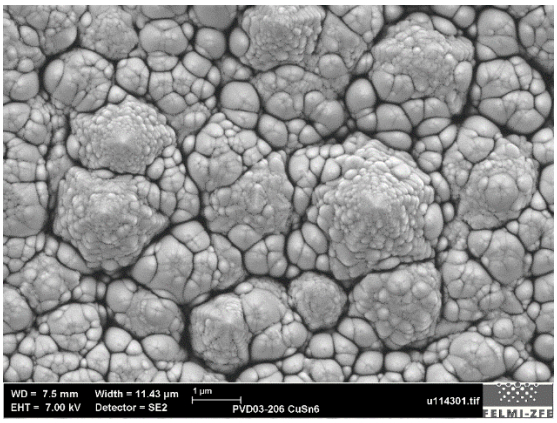

Figure 44 - CuSn6 (PVD03-206). 3D- image of the surface of the CuSn6 film. It resembles the structure of Romanesco broccoli. 7 keV and SE detection system.

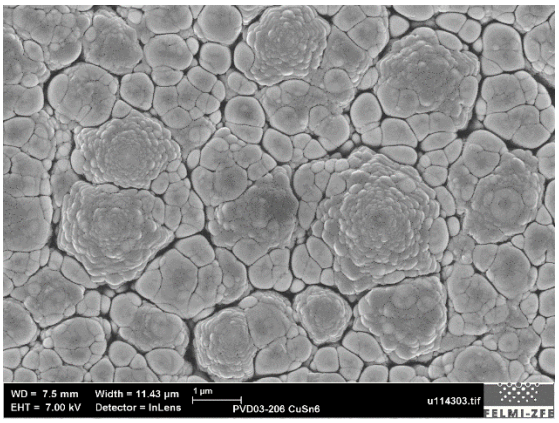

Figure 45 - CuSn6 (PVD03-206). Image taken with an InLens detection system to illustrate the fine structures and grain boundaries more precisely.

The whole image area of Figure 42 was scanned and quantified with EDS at an acceleration voltage of 15 and 7 keV to determine the average composition of the desired CuSn6 film. The results are listed below in Table 5.

Table 5 - Results of the quantitative analysis of the area shown in Figure 42 at an acceleration potential of 15 and 7 keV

Acceleration potential	15 keV		7 keV	
Element	*[wt%]*	*[at%]*	*[wt%]*	*[at%]*
Sn L-line	4.32	2.36	7.22	4.00
Cu K-line	95.68	97.64	92.78	96.00

The results deviate slightly from the desired composition but to assess the accuracy of the EDS quantification method the missing AAS results would be helpful. The differences of quantification between 7 and 15 keV result from different interaction volumes.

For further investigations, different positions were selected to show possible differences in composition within the film illustrated in Figure 46 and 47. The composition of the pyramids at position +1 and +2 measured at 15 keV is relatively similar, the smaller and brighter dot at position +3 contains more tin (Fig. 46).

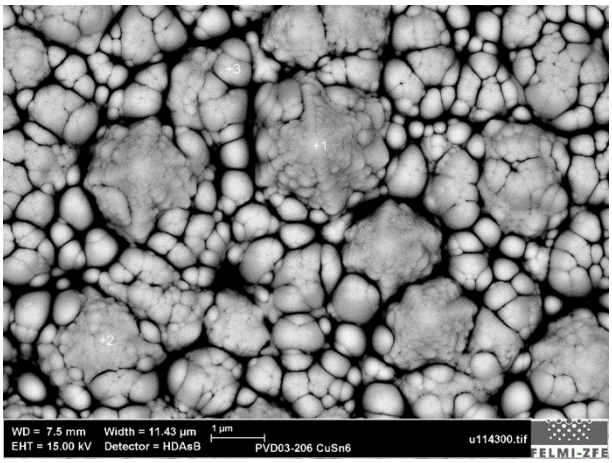

Figure 46 – CuSn6 (PVD03-206). This image exhibits the selected positions for the quantitative analysis to show compositional differences across the film. 15 keV and HDAsB detection system.

Table 6 – Results of the quantitative analysis of position +1, +2 and +3 shown in Figure 46.

	Position in image		
Element	*+1 [wt%]*	*+2 [wt%]*	*+3 [wt%]*
Sn L-line	4.84	4.61	5.91
Cu K-line	95.16	95.39	94.81

The tin content at other selected positions and measured with 7 keV is about 1 to 2 wt% higher compared to the measurements at 15 keV and, thus, very close to the desired composition (Fig. 47).

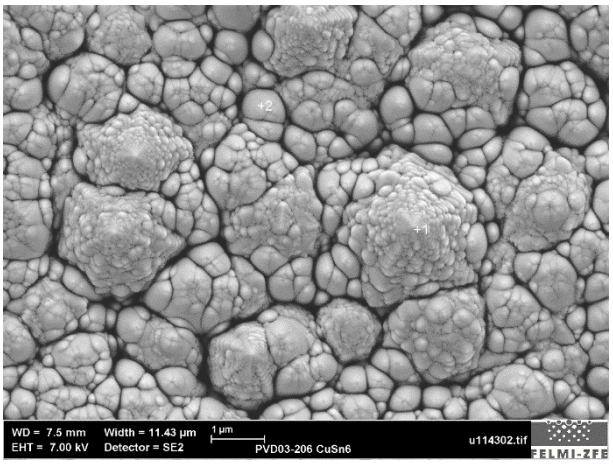

Figure 47 - CuSn6 (PVD03-206). Selected positions +1 and +2 to show the compositional contrast of the different structures within the CuSn6 film recorded at 7 keV.

Table 7 – Results of the EDS quantification of position +1 and +2 from Figure 47.

	Position in image	
Element	*+1 [wt%]*	*+2 [wt%]*
Sn L-line	5.26	6.28
Cu K-line	94.74	93.72

These results show that the composition of different positions only slightly varies. Thus, a relatively homogenous deposition of CuSn6 is possible. For the determination of the average composition of a metal film it is very important to scan and quantify a large area with EDS to gain a meaningful result.

Due to the voluminous structure of the surface film, geometry effects and consequent absorption of secondary or backscattered electrons by higher positions in the surrounding are unavoidable. These effects could falsify the results of the composition. This can be minimized by preparing a polished cross section. Also different correction modes and optimizations methods can be used to reduce such effects, but therefore a suitable reference value (AAS measurement) is necessary.

Figure 48 shows that also a small amount of oxygen and carbon can be detected with EDS quantification. Since the layers were not immediately measured after the deposition and transported in the air atmosphere, oxidation of copper is unavoidable. The carbon at the film probably results from the paper

which was covered around the layer during the transportation. Due to the relatively high oxidation potential of copper, the voluminous surface structure of the film could be the result of the formation of oxides. However, therefore the content of oxygen should be higher as measured. To determine oxide formation on the film additional measurement methods like Raman spectroscopy are necessary.

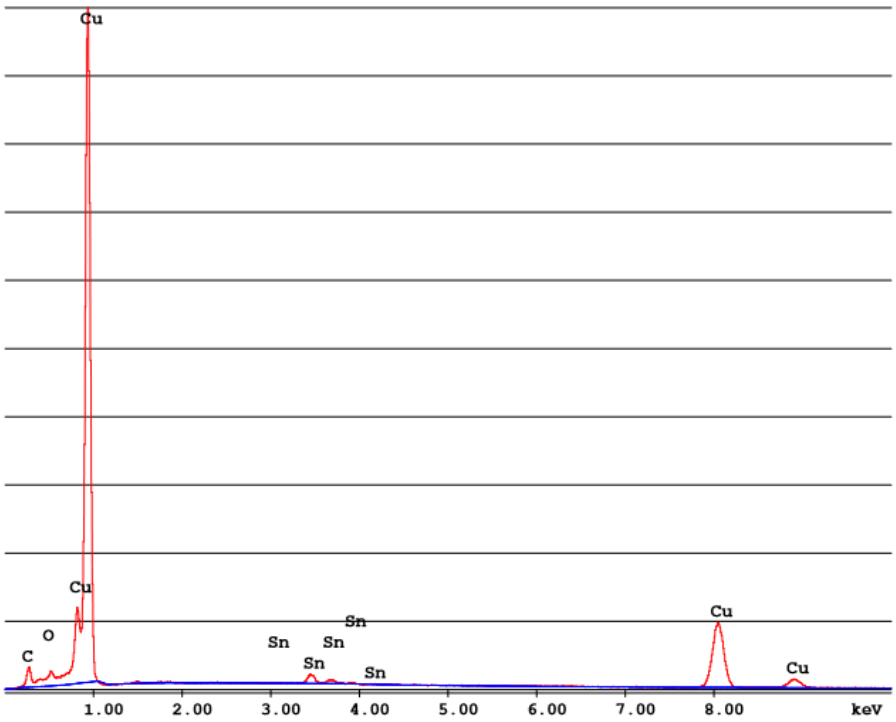

Figure 48 - CuSn6 (PVD03-206). Spectrum of EDS measurement recorded at an acceleration voltage of 15 keV. Cu, Sn, C and O were detected.

6.2.1.2 Investigation of the Polished Cross-Section

For layer PDV03-206 a polished cross-section was prepared. Therefore, Method 1, explained in Chapter 5.3, was used. Thus, a totally different impression of the film can be created.

The layer in the polished cross-section shows a relatively homogenous columnar structure in Figure 49. At some positions broader cracks are illustrated (Fig. 50), which even reach the stainless-steel sheet and resemble break-outs. This problematic growing of the layer might be the result of nucleation due to deformations (scratches or tooth-like break-outs) on the substrate surface. These cracks also might be a result from stress. Such defects are present across the whole layer and might be those positions, which appear as larger, pyramid-like grains in the surface images (Fig. 44). The finer cracks can be explained as grain boundaries resulting from inhomogeneous nucleation due to the large temperature gradient arising from the “cold start”. This effect is less formed in the CuSn6 layer RR60 which was started on a preheated substrate (“warm start”) (Fig. 52). This finer cracks or grain boundaries are not mechanical origin but thermodynamic.

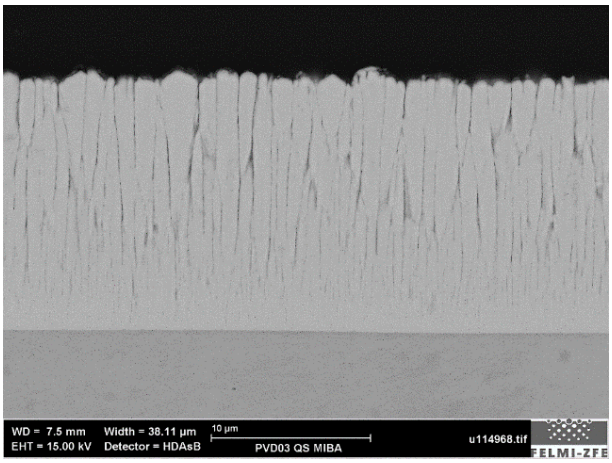

Figure 49 - CuSn6 (PVD03-206). This image shows the relatively homogenous but columnar structure of the CuSn6 film. It was recorded at 15 keV with a HDAsB detection system.

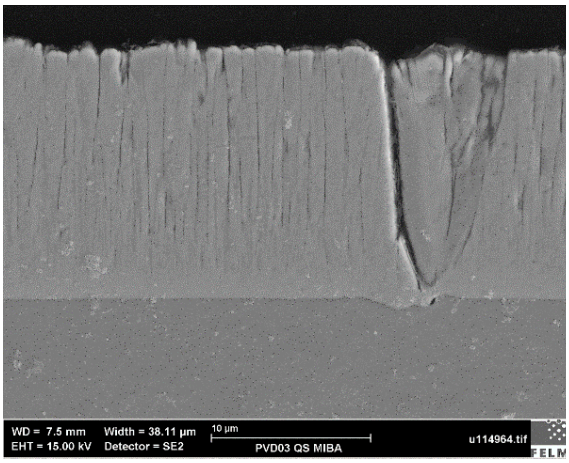

Figure 50 - CuSn6 (PVD03-206). It illustrates a crack formation due to defects on the substrate surface or stress. 15 keV and SE detection system.

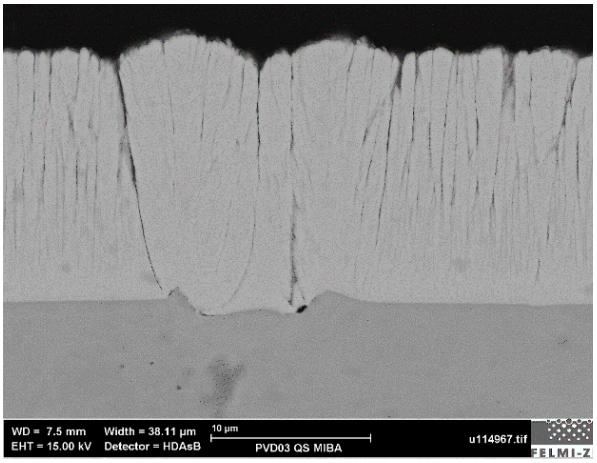

Figure 51 - CuSn6 (PVD03-206). Another deformation of the CuSn6 layer due to defects on the stainless-steel sheet. Recorded with 15 keV and HDAsB detection system.

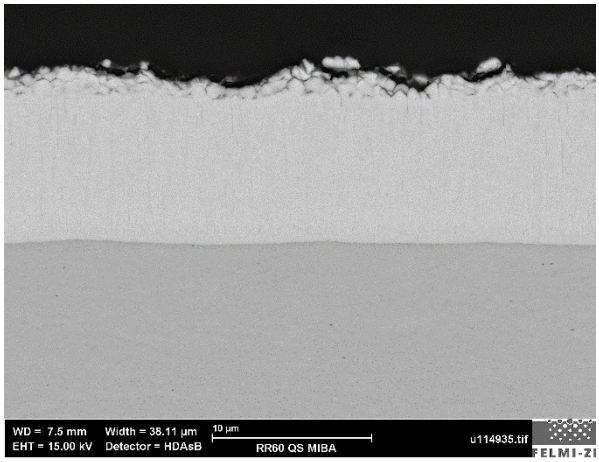

Figure 52 -CuSn6 (RR60). In this layer the grain boundaries are less visible or even finer possibly due to the "warm start" of the sputter deposition and the lower temperature gradient.

The quantitative analysis of the film was performed across a large area shown in Figure 53 at 7 and 15 keV. The determined average composition of the film is relatively close to the desired CuSn6 composition. However, due to the missing AAS analysis, it is not possible to assess the accuracy of the EDS analysis. Nevertheless, the results confirm again that the solubility of tin in copper under certain conditions is given and a solid solution is formed.

Table 8 – Results of quantitative analysis of area 1 shown in Figure 53

	15 keV		7 keV	
Element	*[wt%]*	*[at%]*	*[wt%]*	*[at%]*
Sn L-line	5.07	2.78	6.18	3.41
Cu K-line	94.79	97.22	93.82	96.59

As already shown in the quantitative analysis of the surface, the determined amount of tin is always a little higher at lower acceleration potential.

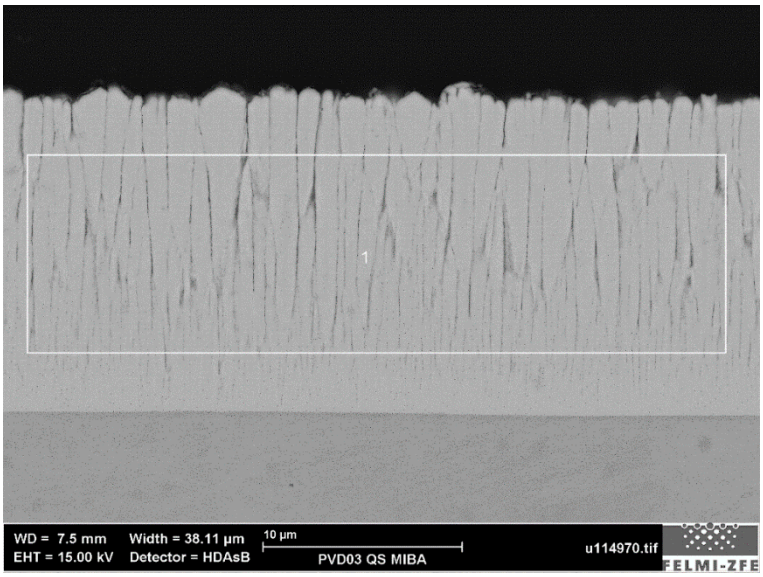

Figure 53 - CuSn6 (PVD03-206). Selected area for the quantitative analysis recorded at 7 and 15 keV. 15 keV and HDAsB detection system.

Higher magnifications show that residues from the lubricant (mostly silicon) used for polishing stick to the surface. The brighter dots shown in Figure 54 mainly contain silicon. These impurities can falsify the quantitative analysis with EDS. Thus, a careful layer preparation is necessary.

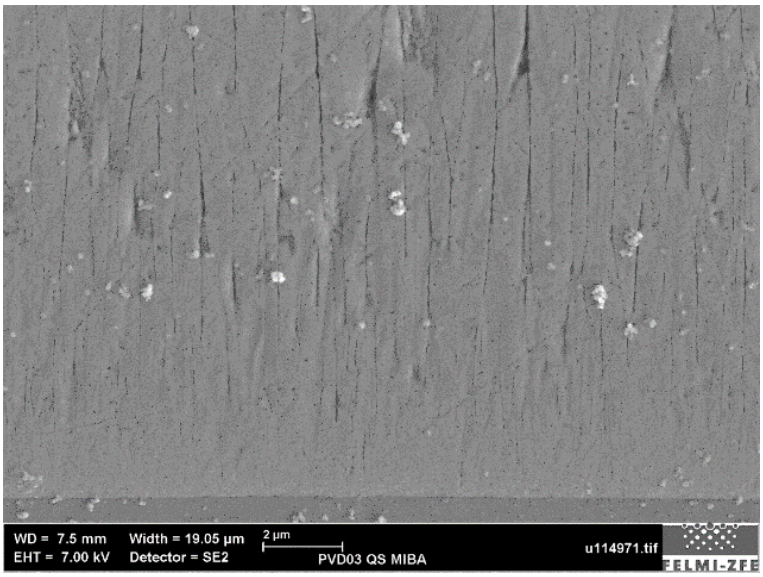

Figure 54 - CuSn6 (PVD03-206). This image shows contaminants from lubricants on the surface of the polished cross-section. 7 keV and SE detection system.

6.2.2 CuSn6 (RR60)

Layer RR60 should ideally have the composition CuSn6. The AAS analysis yields a composition of 3.79 wt% Sn and 96.21 wt% copper. The deposition was started on a warm substrate in contrast to the layer of PVD03-206 (Chapter 6.2.1). Thus, the sputter process starts at a temperature of about 190°C and ends at 210°C. During the deposition, the systems reaches a maximum of 250 °. For the deposition, a CuSn6 alloy target is used. Since Cu and Sn have the similar vapor pressure, the composition of the deposited film is almost the same as those of the alloy target.

6.2.2.1 Investigation of the Untreated Surface

In Figure 55 the surface of the film of sample RR60 appears very homogenous and smooth. Moreover, the lines from the structure of the substrate, which are depicted through the layer, can be seen. The area of this image was investigated with SEM-EDS to determine the average composition of the film (Table 9). The composition determined by 15 keV deviates less than 1 wt% from those of the AAS analysis. The quantitative analysis with 7 keV shows a larger deviation.

Table 9 - Average composition of the CuSn6 film measured with 15 and 7 keV.

	AAS	15 keV		7 keV	
Element	*[wt%]*	*[wt%]*	*[at%]*	*[wt%]*	*[at%]*
Sn L-line	3.79	4.60	2.52	5.98	3.29
Cu K-line	96.21	95.40	97.48	94.02	96.71

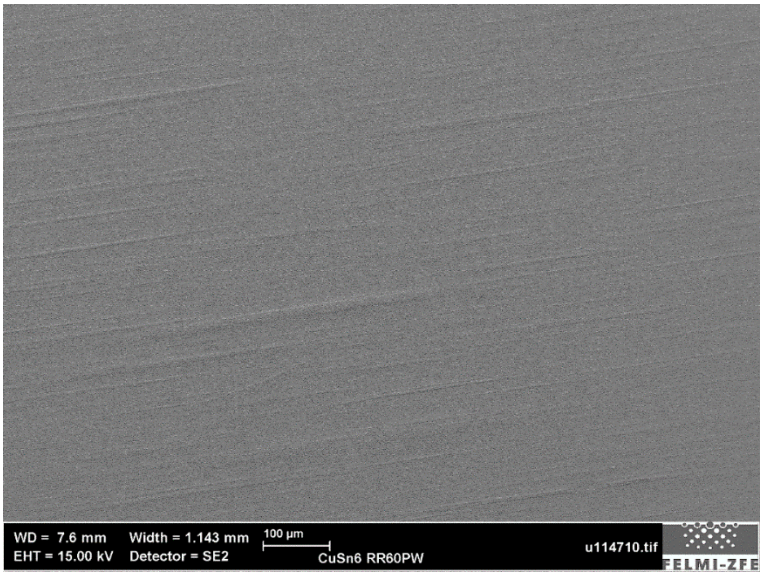

Figure 55 - CuSn6 (RR60). This image illustrates the area, which was analyzed to determine the average composition of layer RR60. 15 keV and SE detection system.

In Figure 56 the CuSn6 film of sample RR60 appears as a very homogenous granular structure. The SE detection image suggests a multiphase structure. However, the HDAsB detection illustrates that there is

no compositional contrast across the film. The SE detection merely shows the topographic contrast of the film as usual.

Figure 57 illustrates that the layer consists of finer and coarser precipitations similar to layer PVD03-206 (Chapter 6.2.1). Moreover, the morphology is less porous than those of layer PVD03-206 due to the higher process temperatures during the deposition of RR60.

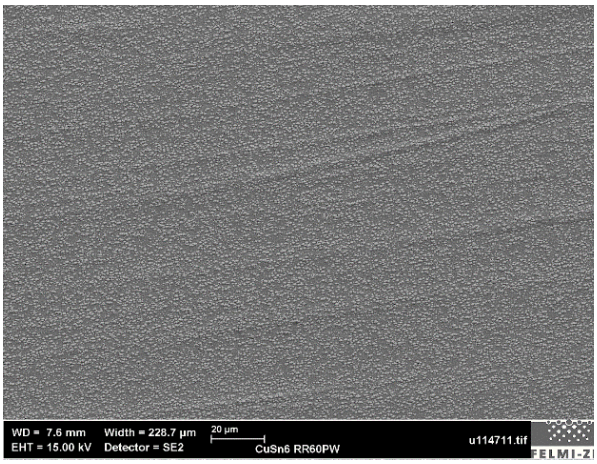

Figure 56 - CuSn6 (RR60). The image shows the homogenous granular structure of the CuSn6 film.

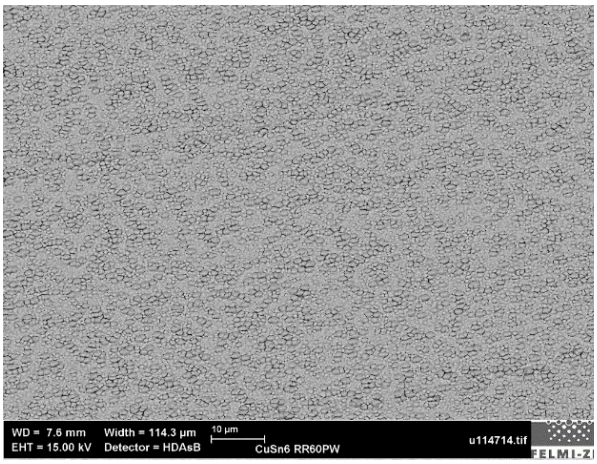

Figure 57 - CuSn6 (RR60). At larger magnification coarser and finer grains are recognizable.

In Figure 58 the structure of the CuSn6 film appears totally different to those of layer PVD03-206. The finer and coarser precipitations seem to be smoother and do not grow like layered pyramids or Romanesco broccoli. However, the growth of the larger grains resembles a cone structure. Three positions in Figure 58 were selected to determine the compositional contrast of the different sized grains at 15 keV. The amount of tin of the coarser grains at position +1 and +2 is about 0.80 wt% higher than those of the average composition. The smallest grain at position +3 shows a lower amount of tin. The larger amount of tin at some positions might arises due to geometry effects. A rough surface leads to the generation of more X-ray radiation of tin and, therefore, the amount of tin appears higher than it is. Moreover, the fact that copper and tin leave the target surface at different average angles can result in variations of the composition across the whole film.

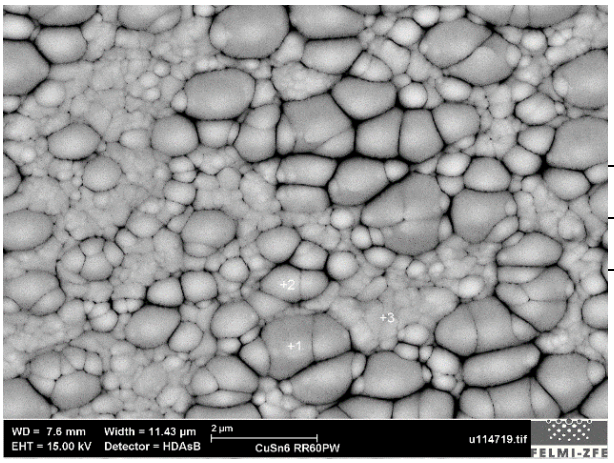

Figure 58 – CuSn6 (RR60). It exhibits the areas selected for the quantitative analysis to show the differences in composition across the CuSn6 film.

Table 10 – The results of the quantitative analysis of the selected positions to show the compositional contrast with 15 keV (Figure 58).

	Position in image		
Element	*+1 [wt%]*	*+2 [wt%]*	*+3 [wt%]*
Sn L-line	5.40	5.47	4.16
Cu K-line	94.60	94.43	95.85

At a lower acceleration potential of 7 keV the material contrast already shown in Table 11 (15 keV) appears clearer in Figure 59 with HDAsB detection than in Figure 60. Coarser grains have a similar composition and finer precipitations as well, as the coloring of the HDAsB image at 7 keV illustrates. The larger and darker grains contain a small amount more tin as the quantitative analysis in Table 11 confirms. In general, the tin content at 7 keV is a little overvalued. This could be already shown for the determination of the average composition of layer RR60 and for the quantitative analysis of layer PVD03-206.

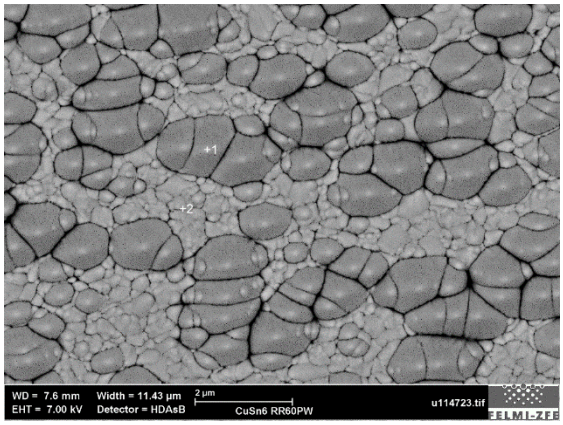

Figure 59 – CuSn6 (RR60). The HDAsB image at 7 keV better shows the compositional contrast of larger and smaller grains of the CuSn film.

Table 11 – The results of the quantitative analysis of the selected positions in Figure 59 to show the compositional contrast with 7 keV.

	Position in image	
Element	*+1 [wt%]*	*+2 [wt%]*
Sn L-line	6.87	5.73
Cu K-line	93.13	94.27

The InLens image (Fig. 60) clearly shows the grain boundaries around the smaller and larger precipitations and that this CuSn6 layer of RR60 is more compact and less porous compared to PVD03-206.

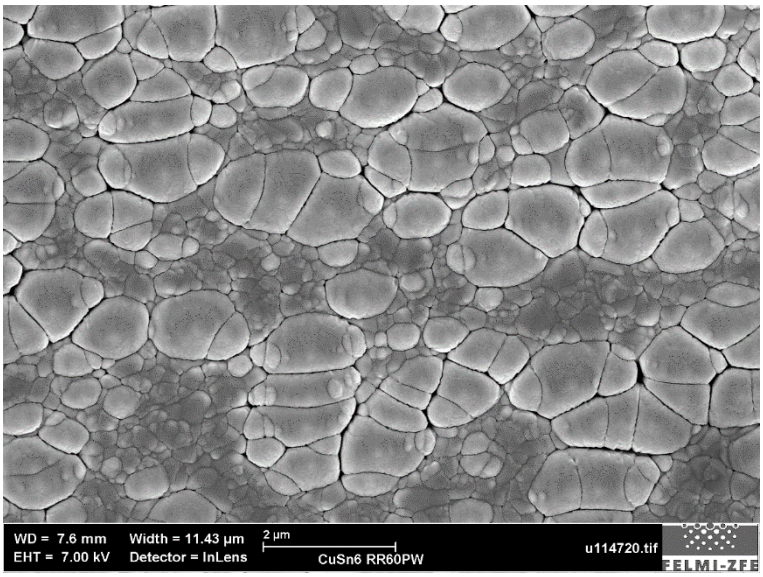

Figure 60 - CuSn6 (RR60). With InLens detection and an acceleration potential of 7 keV the grain boundaries can be clearly seen.

According to the phase diagram (Chapter 4.4.2), the deposition of a homogenous solid solution of copper and tin at this process conditions is possible. Due to the higher temperatures during the sputtering process the generation of pure α- mixed crystals (solid solution) is more likely than for layer PVD03-206. There, maybe additional phases arise due to the lower process temperature.

6.2.2.2 Investigation of the Polished Cross-Section

The polished cross-section of layer RR60 was prepared with Method 1 explained in Chapter 5.3. In the polish the structure of the CuSn6 film appears as well very homogenous in Figure 61. However, the region, where the film gets in contact with the embedding agent, looks relatively rough. At higher magnification, the layer appears totally deformed by the embedding material.

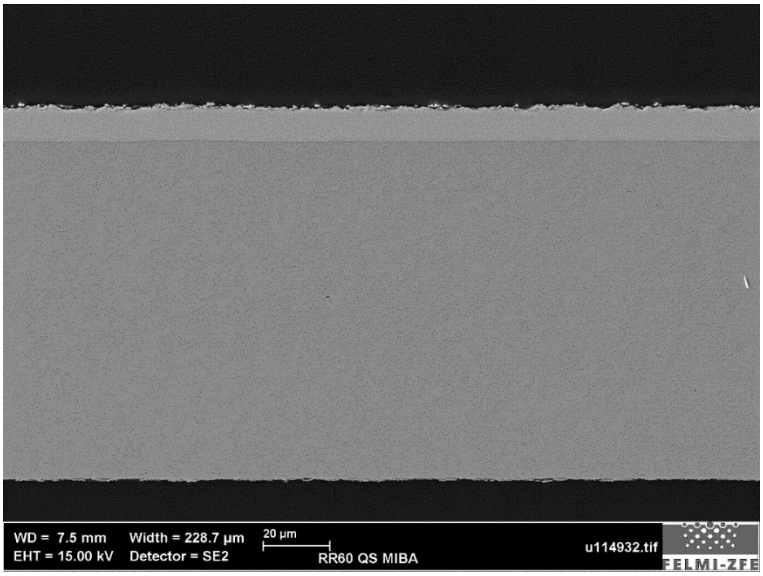

Figure 61 - CuSn6 (RR60). The image shows the polished cross-section of layer RR60 detected with 15 keV.

Figure 62 illustrates the columnar growth of the CuSn film. In contrast to layer PVD03-206 the structure is less porous. For the quantitative analysis, the selected area 1 in Figure 62 was analyzed. The amount of tin in the CuSn film determined in the polished cross-section is about 1.3 wt% higher than the results of the AAS analysis and deviates from the surface measurements as well. The amount of copper at 15 keV was determined by the Cu-K-line and at 7 keV by the Cu-L-line. The difference in the quantitative analysis of Cu-K and Cu-L-line is minimal.

Table 12 – The results of the quantitative analysis of area 1 of the polished cross-section at 15 and 7 keV (Fig. 62).

	AAS	15 keV		7 keV	
Element	*[wt%]*	*[wt%]*	*[at%]*	*[wt%]*	*[at%]*
Sn L-line	3.79	5.14	2.82	5.07	2.78
Cu -line	96.21	94.86	97.18	94.93	97.22

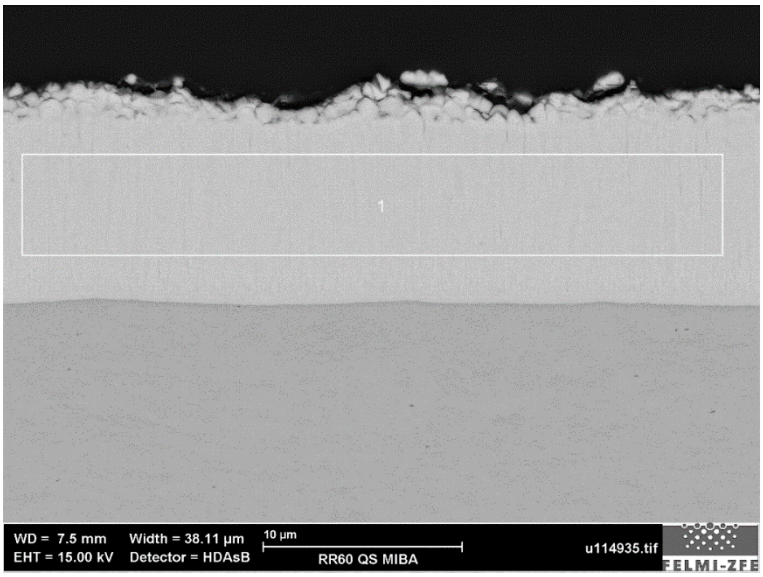

Figure 62 – CuSn6 (RR60). This image shows the columnar growth of the CuSn6 film and the selected area for the quantitative analysis of layer RR60.

Figure 63 illustrates many fine scratches across the surface of the polish, which results from tiny hard particles from polishing material. Moreover, residues (silicon) from the polishing plates or agents (light particles on the surface) are present. Thus, the polishing procedure should be improved to get more accurate results.

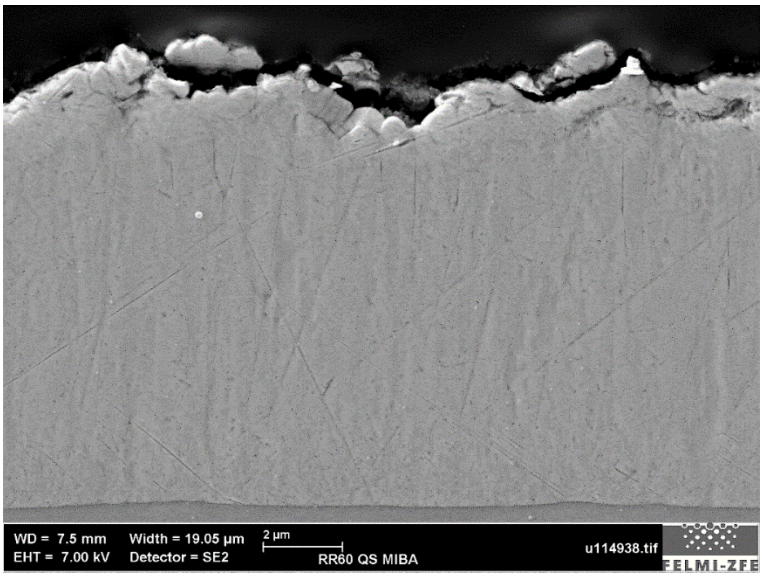

Figure 63 – CuSn6 (RR60). This image illustrates the problems of the polish preparation. Fine scratches and residues of the polishing plates and agents (light particles in the surface) can falsify the results of the quantitative analysis.

6.2.3 Cu9Pb (RR32)

The layer RR32 should have the composition Cu9Pb. The AAS analysis of the sputtered CuPb layer shows a composition of 90.58 wt% lead and 9.42 wt% copper. The deposition was started on a cold (room temperature) stainless steel substrate. Thus, the temperature during the sputtering process does not exceed 150 °C. An elemental copper target and an elemental lead target was used to deposit the desired Cu9Pb film.

6.2.3.1 Investigation of the Untreated Surface

The Cu9Pb layer of sample RR32 appears very homogenous in Figure 64. The lines, which arise due to line structure of the stainless-steel band, are very well developed. Reason for that might be that the Cu9Pb film is relatively soft and, therefore, the structure of the harder substrate is especially strongly depicted.

For the determination of the average composition of the Cu9Pb film, the area of Figure 64 was scanned and analyzed with SEM-EDS. For the analysis with 15 and 7 keV, the results deviate maximum 1 wt% from those of the AAS analysis.

Table 13 – The results of the quantitative analysis of the area shown in Figure 64 recorded at 15 and 7 keV.

	AAS	15 keV		7 keV	
Element	*[wt%]*	*[wt%]*	*[at%]*	*[wt%]*	*[at%]*
Cu K-line	9.42	8.44	23.12	9.3	74.95
Pb M-line	90.58	91.56	76.88	90.7	25.05

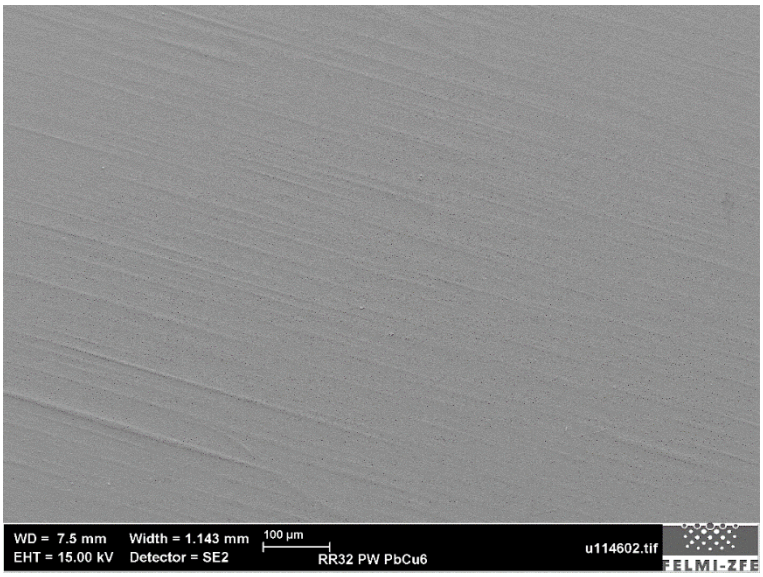

Figure 64 – Cu9Pb (RR32). The SE image of layer RR32 appears relatively homogenous and shows the lines resulting from the structure of the stainless-steel substrate.

In Figure 65 the layer appears very porous. Smaller and larger pores give the layer a sponge-like structure. It is almost impossible to show this porous morphology in a polished cross-section, since the pores are smeared up with lead. However, with a broad ion beam preparation it should be possible.
The next image possibly shows fine precipitations of copper and lead across the film, but the quantitative analysis of these structures is not possible due to the limited resolution (2 µm) of EDS.

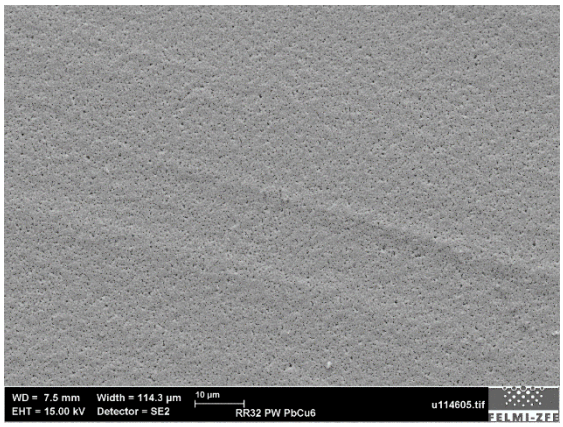

Figure 65 – Cu9Pb (RR32). This image illustrates a porous structure.

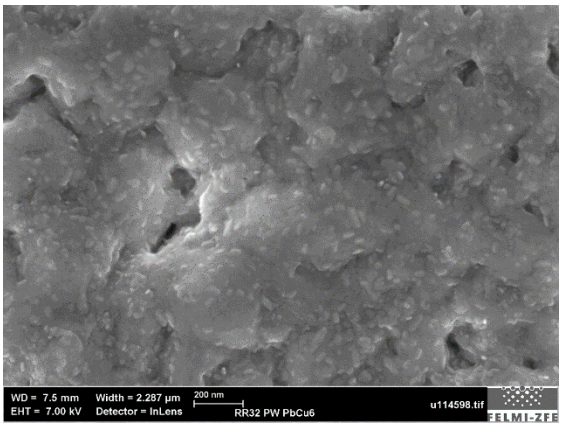

Figure 66 – Cu9Pb (RR32). With an InLens detector small lead and copper precipitations are recognizable at 7 keV.

To keep the interaction volume as small as possible and to minimize the uptake of information from the surrounding, the selected areas from Fig. 67 were measured with 7kev. The darker position +1 contains less lead compared to the brighter position + 2. Position +3 was not analyzed, since the selected structure was too small for EDS analysis. The selected lead precipitation was about 50 nm. All three positions show high amount of oxygen. The higher the amount of lead, the higher is the oxidation of the film.

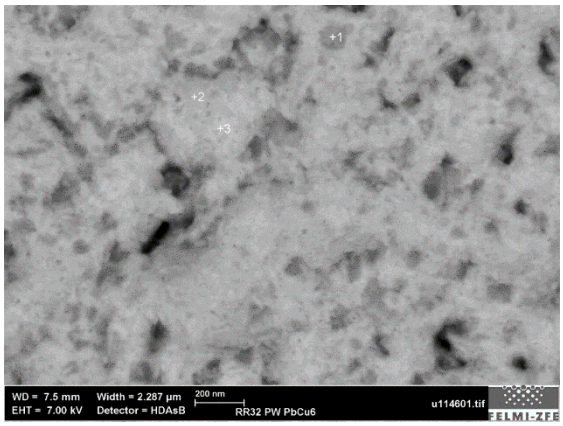

Figure 67 – Cu9Pb (RR32). This image shows the selected areas for the quantitative analysis recorded with 7 keV.

Table 14 – The results of the quantitative analysis of the selected positions from Figure 67 at 7 keV:

	Position in image	
Element	*+1 [wt%]*	*+2 [wt%]*
Cu K-line	46.7	81.56
Pb M-line	53.3	18.44

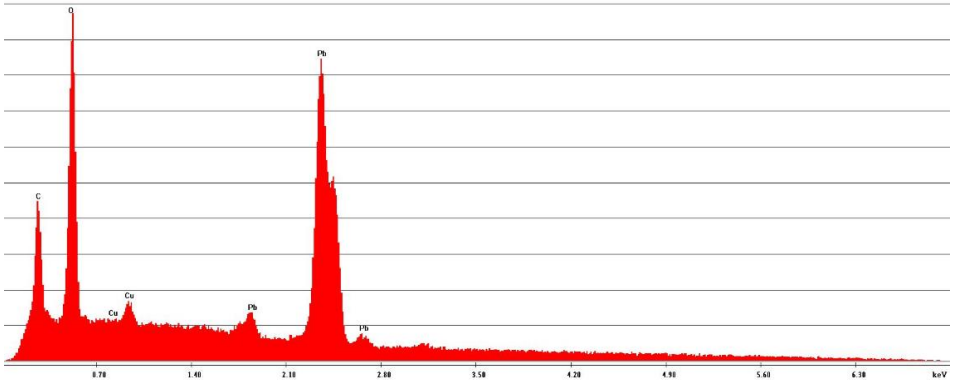

Figure 68 - This spectrum shows the high amount of oxygen on the film surface at position +2 in Figure 67 of Cu9Pb layer RR32.

6.2.3.2 Investigation of the Polished Cross-Section

The polished cross-section of layer RR32 was prepared with Method 1 as explained in Chapter 5.3. Figure 69 shows a delamination of the Cu9Pb film. This defect does not result from the preparation process due to the regularity of the fracture. It possibly already happened during the deposition due to changing conditions while sputtering.

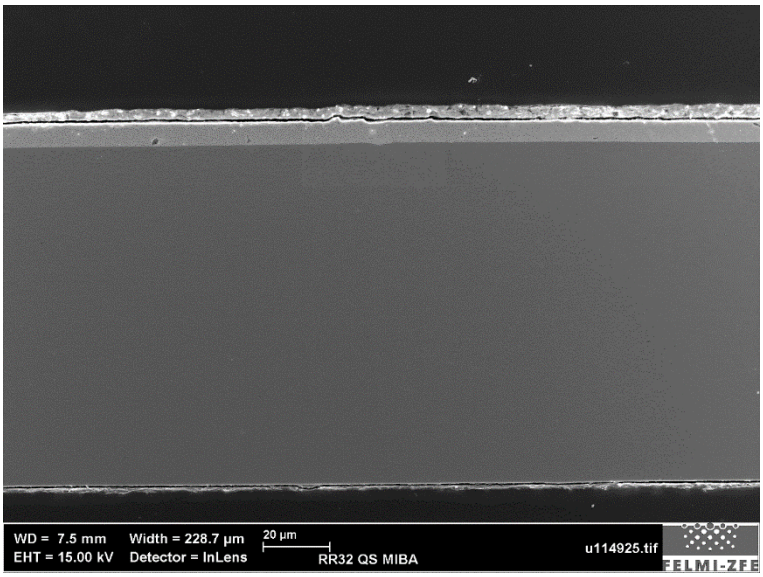

Figure 69 – Cu9Pb (RR32). This image illustrates the delamination of the Cu9Pb film.

Due to delamination, the determination of the average composition of the film was performed for both layers. Therefore, the selected areas 1 and 2 shown in Figure 70 were scanned and analyzed with SEM-EDS. The composition of area 1 deviates about 1 wt% from the results of the AAS analysis. Area 2 (upper layer) contains a small amount of Fe and Si (< 2 wt%). Silica probably is a residue from the polishing plates and agents. The source of Fe is difficult to understand, but possibly it comes from the copper or lead target, when one of those ran out of copper or lead during deposition process. That the iron comes from the steel substrate due to interaction volume form the primary electron beam is excluded, since the measurement area 2 is far enough away from the substrate.

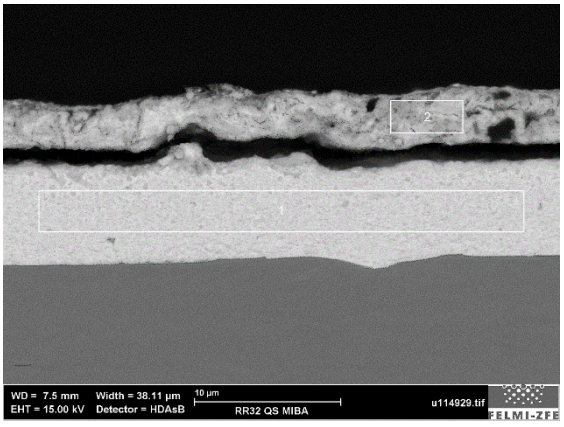

Figure 70 – Cu9Pb (RR32). This figure illustrates the two selected areas for the quantitative analysis of the Cu9Pb film.

Table 15 – The results of the quantitative analysis of the upper and lower layer of layer RR32 (Figure 70) recorded at 15 keV. The upper layer additionally contains 1.36 wt% Si and 1.64 wt% Fe.

	Area in image		
Element	*AAS [wt%]*	*1 [wt%]*	*2 [wt%]*
Cu K-line	9.42	10.91	12.75
Pb M-line	90.58	89.09	84.24

Higher magnifications (Fig. 71) show that the two layers have a totally different structure. In the upper layer spherical lead precipitations are preferable present, whereas the lower layer generally appears more homogenous. Between the two layers, residues from the polishing materials are visible.

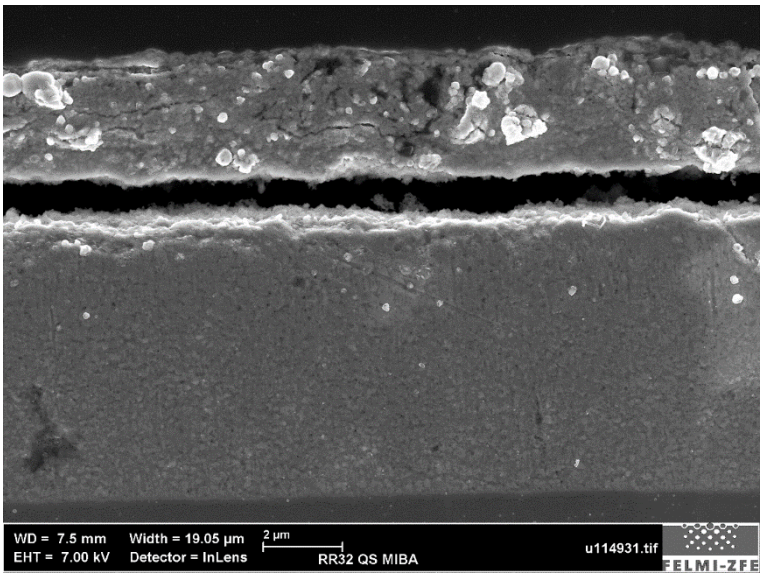

Figure 71 – Cu9Pb (RR32). The InLens detection shows that especially in the upper layer spherical lead precipitations are present. Residues from polishing are visible between upper and lower layer.

The greatest problem to correctly analyze the Cu9Pb film is to find a preparation method, which does not smear the soft metal alloy. The used polishing methods are not necessarily suitable. The preparation can be improved by using the broad ion beam cut. However, this method cannot be implemented into the serial monitoring of the sputtered layers in the multi-layer system due to the high time expense and the high costs.

6.2.4 CuPb27 (RR28)

The sputtered layer of sample RR28 should have the composition CuPb27.The AAS analysis yields 71.5 wt% Cu and 28.5 wt% Pb. The deposition process was started on a cold (room temperature) substrate. Thus, the temperature during the process does not exceed 150°C. For the deposition, an elemental copper and an elemental lead target was used, because due to the large mass difference of Cu and Pb. (Chapter 4.2.13).

6.2.4.1 Investigation of the Untreated Surface

The untreated surface of layer RR28 in Figure 72 appears very granular but homogenous. The average composition of RR28 was determined by scanning the area of the image Figure 72 with 15 keV. The amount of Pb in the film is strongly undervalued. Geometry effects and the absorption of secondary or backscattered electrons by the layer might be the reason for the deviation of the results. The preparation of a polished cross-section of the layer or special optimization modes (k-correction) are necessary to improve the results.

Table 16 – The results of the average composition of layer RR28 recorded at 15 keV (Fig. 72)

	AAS	15 keV	
Element	*[wt%]*	*[wt%]*	*[at%]*
Cu K-line	71.5	80.34	93.02
Pb M-line	28.5	19.66	6.98

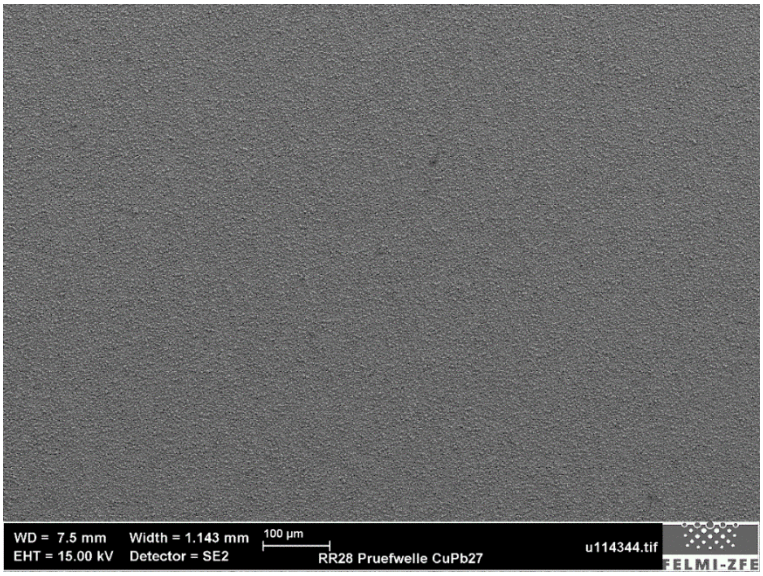

Figure 72 – CuPb27 (RR28). Granular structure of RR28 recorded with 15 keV and SE detection system.

The next images show a very porous morphology, which resembles agglomerates. In Figure 73 it seems as this cloud-like structures grow up cone-shaped.

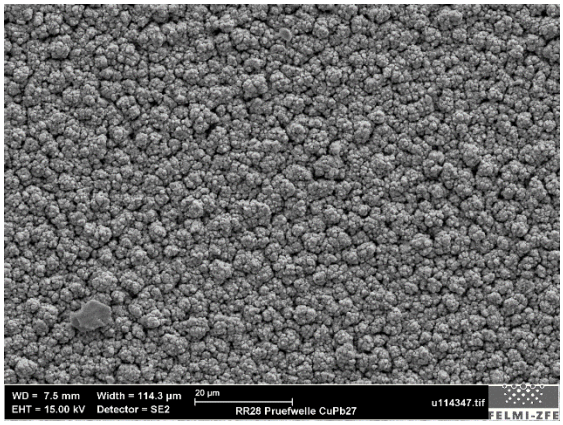

Figure 73 – CuPb27 (RR28). The structure of the CuPb27 film resembles agglomerates. 15 keV and SE detection system.

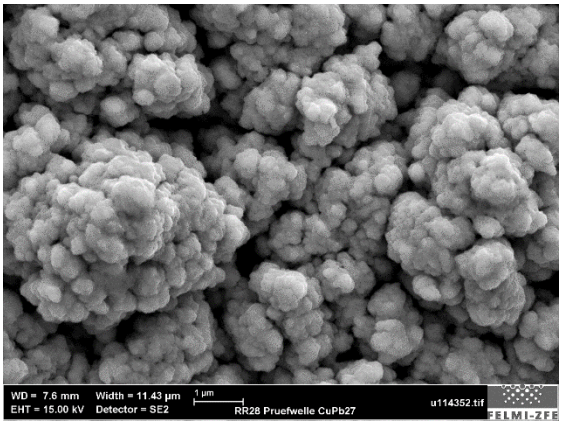

Figure 74 – CuPb27 (RR28). This SE image shows the cone-shaped agglomerates of the CuPb27 film. 15 keV and SE detection system.

To show the compositional contrast of the CuPb27 film an HDAsB image of RR28 was taken. It illustrates again the high porosity of the film and that darker and brighter areas are present as expected, due to the immiscibility of lead in copper at these process temperatures (Chapter 4.4.1). However, it seems as if fine lead grains are distributed over the whole layer. However mixed Cu-Pb phases (Table 17) are formed due to the rapid cooling after deposition. As a result, that the diffusion is unhindered, and the phases cannot be completely separated.

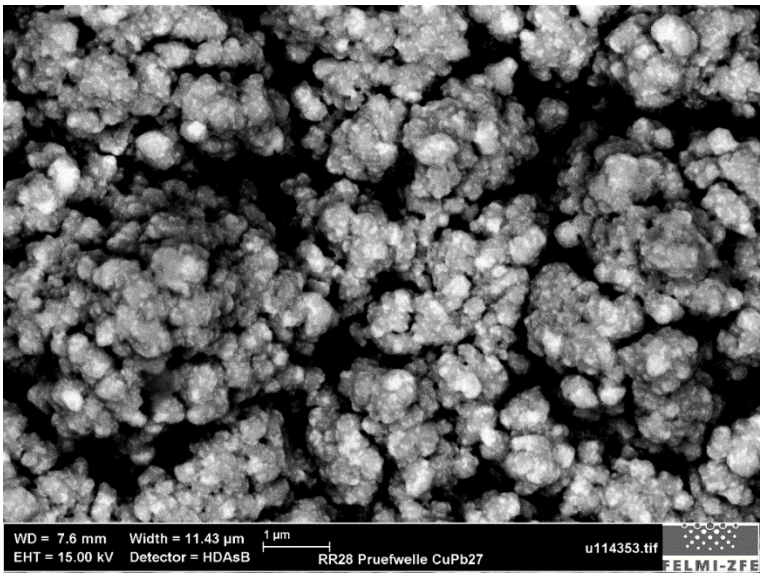

Figure 75 – The HDAsB- image shows the compositional contrast of RR28 measured at 15 keV.

To illustrate the differences in composition within the film a brighter and a darker area was selected for further quantitative analysis (Fig. 76). The brighter position +1 consists of equal parts of copper and lead according to the EDS analysis. The darker area +2 is rich in copper as expected. Due to the relatively large interaction volume at an acceleration potential of 15 keV, it cannot make a clear statement about the accuracy of the EDS results.

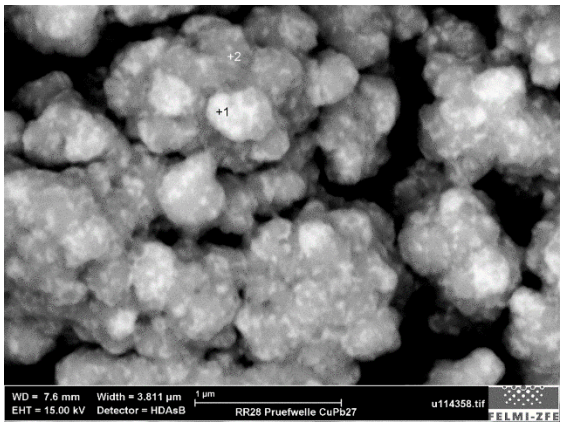

Figure 76 – CuPb27 (RR28). In this image small lead precipitations are visible. Position +1 and +2 were selected for the quantitative analysis at 15 keV.

Table 17 – The results of the quantitative analysis of selected positions shown in Figure 76 recorded at 15 keV.

	Position in image	
Element	*+1 [wt%]*	*+2 [wt%]*
Cu K-line	50.17	80.61
Pb M-line	49.83	19.39

A further quantitative analysis was performed at 7 keV (Fig. 77). The results are relatively similar to the measurement at 15 keV. However, position +1 shows a little more lead (53 wt%) compared to copper (47 wt%) that better corresponds to the coloring of the compositional contrast. Possibly the structure of the film consists of copper crystals covered with smaller lead precipitations. Therefore, the analysis at 7 keV obviously shows a larger amount of lead at position +1, due to minimized interaction volume. The darker position 2 consist of 82 wt% copper as expected.

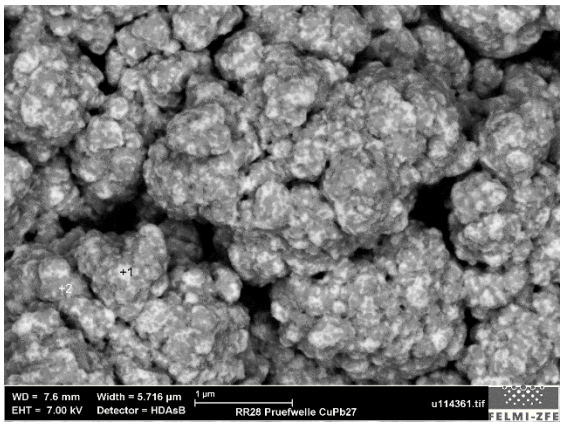

Figure 77 – CuPb27 (RR28). This HDAsB image shows again the multiphase structure of the CuPb27 layer. Position +1 and +2 were selected for the quantitative analysis at 7 keV.

Table 18 – The results of the quantitative analysis of the selected areas shown in Figure 77 recorded at 7 keV.

	Position in image	
Element	*+1 [wt%]*	*+2 [wt%]*
Cu K-line	46.7	81.56
Pb M-line	53.3	18.44

6.2.4.2 Investigation of the Polished Cross-Section

The polished cross-section of layer RR28 was prepared with Method 1 explained in Chapter 5.3.

In Figure 78 the surface of the CuPb27 film appears very rough. Cracks, which reach from the top of the film into the CuPb27 layer, are recognizable across the whole layer.

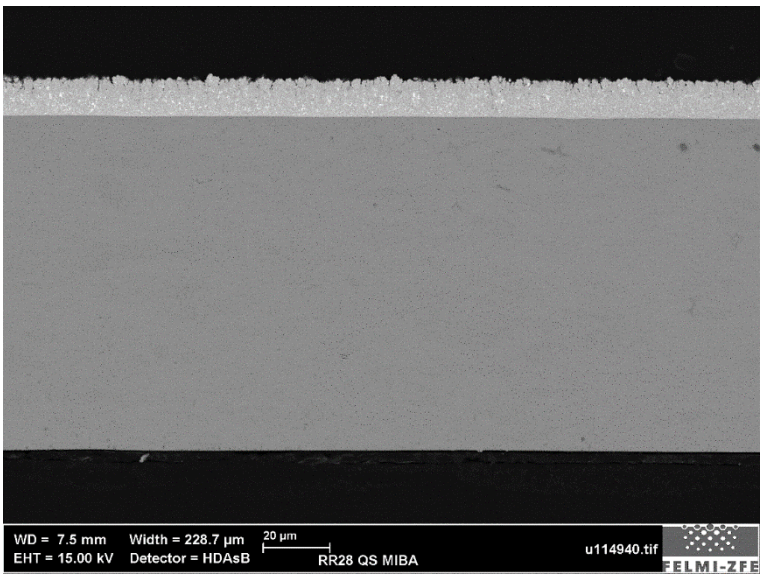

Figure 78 – CuPb27 (RR28). Polished cross-section of layer RR28. It shows a rough surface structure recorded at 15 keV and with HDAsB detection system.

In the next HDAsB image (Fig. 79) it seems as if these cracks are filled with lead. The lower part of the CuPb film appears more homogenous, and the ´filled´ cracks are finer. Towards the surface, the network of Pb precipitations gets larger until large cracks appear in the surface near regions (Fig. 79 and 80). These cracks are not filled and contribute to a very porous morphology. This porosity might be the result of too low process temperatures or changing conditions during the sputtering.

In Figure 80 spherical lead precipitations are recognizable over the whole layer. Moreover, an elemental copper layer is shown between the stainless-steel substrate and the CuPb film.

To determine the average composition of the alloy film area 1 shown in Figure 79 was scanned and analyzed with SEM-EDS. The results at 15 keV deviates about 1 wt% from the AAS values, at 7 keV about 6 wt%. Moreover, a small amount of iron (0.87 wt%) was detected at 15 keV, for 7 keV not. Due to the low process temperatures diffusion from the steel substrate cannot be the reason for the measured amount of Fe in the CuPb film. Thus, gained information from the stainless-steel substrate due to the large interaction volume of the electron beam at 15 keV influences the result.

Table 19 -The results of the quantitative analysis of area 1 (Fig. 79) at 15 and 7 keV. At 15 keV 0.87 wt% Fe from the stainless-steel substrate was measured due to the large interaction volume of the electron beam.

	AAS	15 keV		7 keV	
Element	*[wt%]*	*[wt%]*	*[at%]*	*[wt%]*	*[at%]*
Cu K-line	71.50	69.99	87.58	77.85	91.98
Pb M-line	28.50	29.14	11.18	22.15	8.02

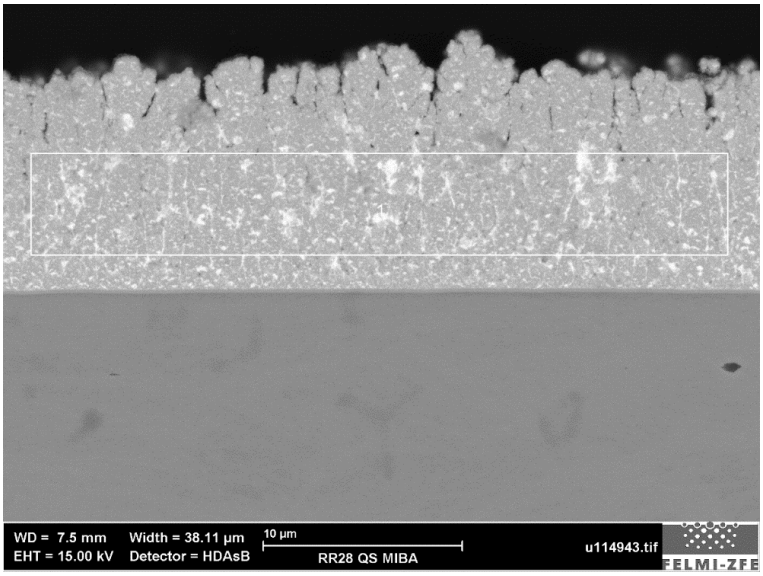

Figure 79 - CuPb27 (RR28). The image shows the area for the quantitative analysis with EDS recorded with 15 keV and HDAsB-detection.

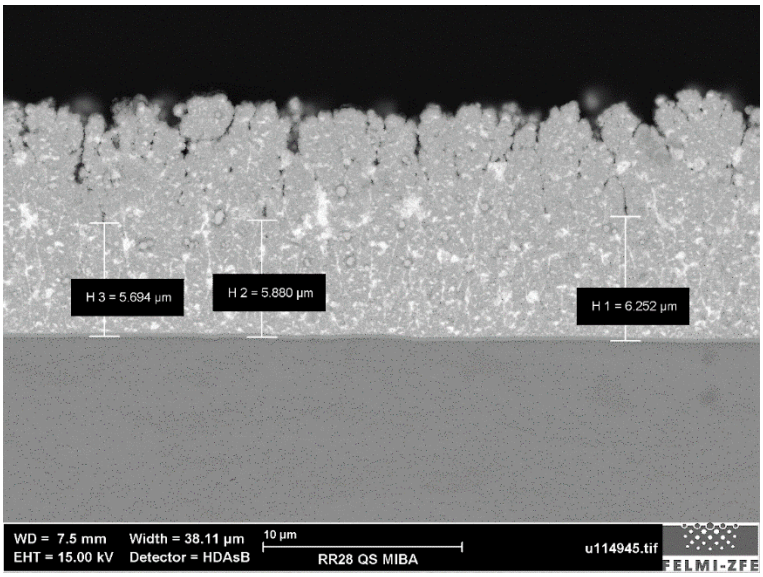

Figure 80 – CuPb27 (RR28). This picture illustrates how far the ´unfilled´ cracks reach into the CuPb27 film.

6.2.5 CuPb25 (RR69) prepared with Broad-Ion-Beam Milling

Layer RR69 with the desired composition CuPb25 was prepared by broad ion beam milling. The AAS measurements yield a composition of 31 wt% Pb and 69 wt% Cu.

The sputter process was started on a warm substrate. The deposition started at a temperature of 260 °C and drops to 240°C while sputtering. Thus, this layer was coated at higher temperatures compared to RR28. Therefore, a more continuous and homogenous film compared to RR28 is suspected. As sputter source an elemental lead and copper target was used.

The structure of the film of the following image resembles the polished cross-section of RR28 but a narrow ham is detected on the surface of the film. The gap between the sputtered layer and the protection tungsten plate is larger than for usual broad-ion beam preparations due to the very rough surface of the Cub25 film. The difference between the widest and narrowest point of the layer is over 5 µm. Within this gap undesired residues of re-deposition might accumulate, which can raise problems in further analysis. Moreover, larger and smaller pores within the M42 steel substrate could be detected.

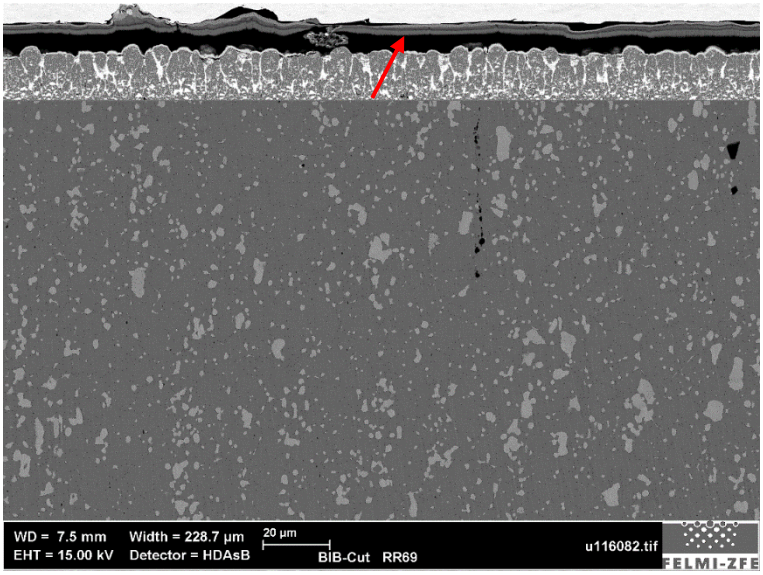

Figure 81 – CuPb25 (RR69 BIB cut). Polished cross-section of layer RR69 after broad-ion beam preparation. HDAsB detection and 15 keV. The red arrow shows the re-deposition residues between the CuPb25 film and the tungsten blade.

Due to the BIB cut preparation the larger and smaller pores within the CuPb25 film clearly appear. The images of RR28 (CuPb27) suggested that there are pores within the layer. It was suspected that the holes arise due to the polishing process, which still cannot be completely ruled out. Some lead particles are teared out of the film by hard polishing materials and leave pores. However, it was also suspected that the soft metal lead smear across the film while polishing and fills pores resulting from the deposition process. Thus, one advantage of this preparation method is that the real microstructure of the layer can be uncovered without smearing soft metals like Pb across the whole film and falsify the appearance.

The thin hem on the surface of the of the CuPb25 film could be re-deposition residues from the steel substrate or tungsten plate but this can be excluded due to a quick elemental analysis with SEM-EDS. The re-deposition residues are located at the other side of the gap between the CuPb25 film and the tungsten blade (Fig. 81). Due to the regularity a lead and copper oxide layer is rather suspected.

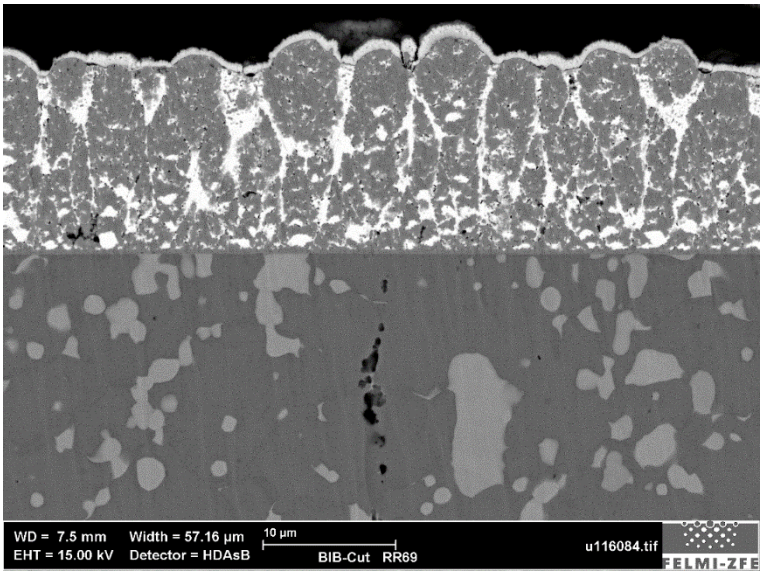

Figure 82 – CuPb25 (RR69 BIB cut). In this image a thin hem on the CuPb25 film appears. Undesired pores within the film and the steel substrate are presents. HDAsB detection and 15 keV.

The quantitative analysis of the surface of RR69 (Fig. 83) shows almost the same composition as those of the ´US measurement` of the BIB-cut shown in Table 21, but a little more oxygen is present. Possibly, the hem is a delamination of the main CuPb25 layer as already observed for layer RR32 (Cu9Pb). The two layers of RR32 are similar in composition, although the HDAsB-image suggests others. That could also apply to this layer. However, the determination of the composition of the hem (1µm) is difficult, since it is very thin, and information form the surrounding would be gained due to the interaction volume of the electron beam.

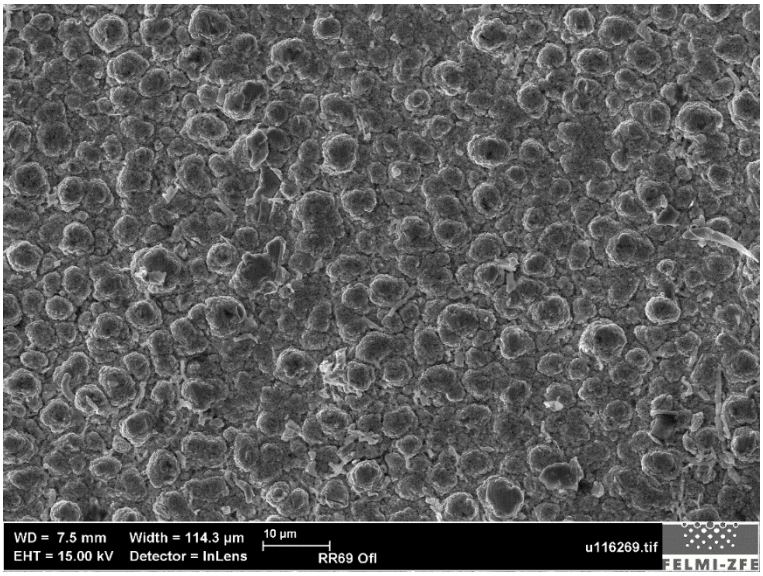

Figure 83 – CuPb25 (RR69 BIB cut). The surface of RR69 appears relatively rough. InLens detection and 15 keV.

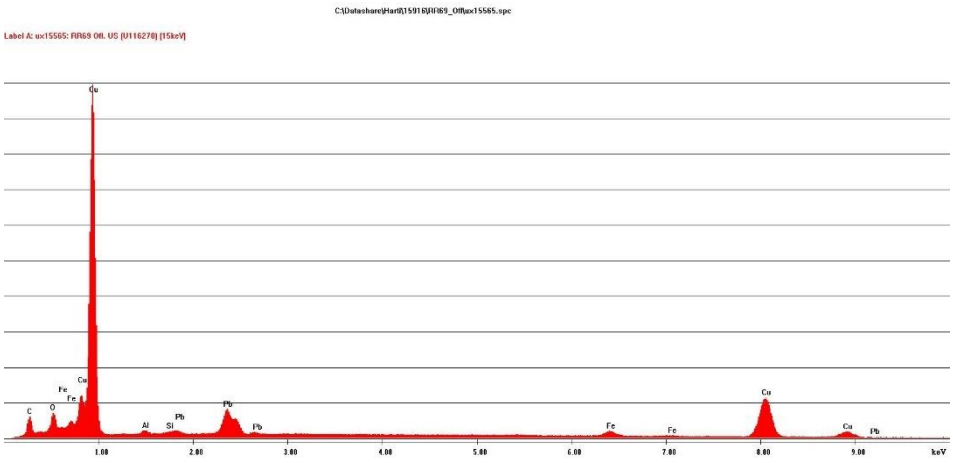

Figure 84 – CuPb25 (RR69 BIB cut). The EDS spectrum of the surface of layer RR69 (Fig. 83) recorded at 15 keV illustrates the similar average composition as those of the BIB-cut prepared area.

The structure of RR69 appears similar to those of RR28 apart from the pores within the film. The first half of the film appears richer in lead compared to the upper half. In the lower part, the Pb is finer and more homogenous distributed. In the upper part of the film, the copper seems to grow up columnar and the lead fills the large cracks between the Cu-rich phases (Fig. 85 and 88). However, not every crack is filled with lead as Figure 88 and 89 exhibits. The temperature measurement during the sputter process illustrates that the deposition starts at about 260°C and relatively quick drops to 239 °C. Thus, the

difference in structure might be explained with the structure zone model (SZM) shown in Figure 86 (Chapter 4.2.12). However, contrary to expectations, at lower process temperatures (upper part of the CuPb26 film) the deposited film grows up more columnar. At higher temperatures the structure is more like Zone T of SZM. Thus, the two different structure within the CuPb25 film of RR69 cannot be clearly comprehended.

The loss of lead in the upper layer cannot be explained by ´back-evaporation` of Pb to the target, since the temperature during deposition of the upper region is lower. Thus, possibly it is pressed into the lower layer, which shows a signification higher amount of lead (Table 20 and 21). The mean of the separate determined composition of the upper and lower part of the CuPb25 film is almost the same as the average composition of the whole area (upper and lower region together).

Immediately after the steel substrate, a 250 to 300 nm thick elemental copper film was deposited as adhesive layer shown in Figure 85.

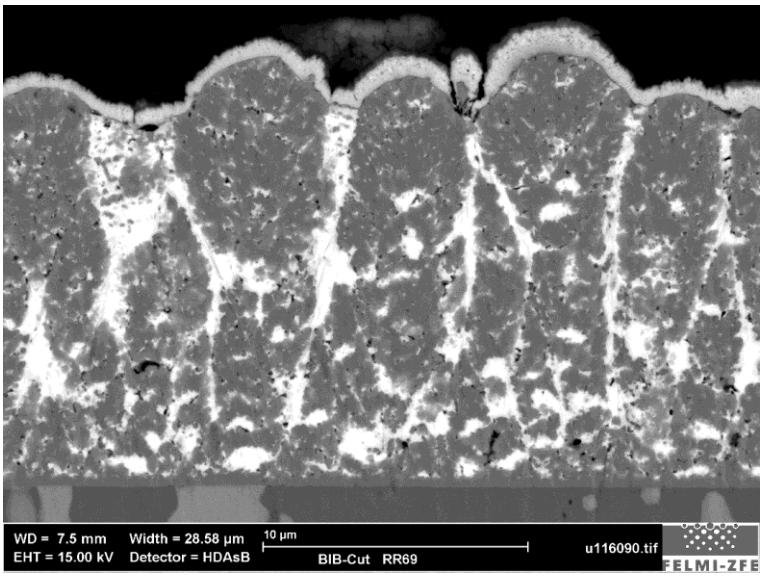

Figure 85 – CuPb25 (RR69 BIB cut). It shows a thin elemental copper film immediately after the steel substrate. The difference in structure across the CuPb25 film is visible. The lower part contains more lead compared to the upper part, where a columnar growth of the copper precipitations appears. HDAsB- detection and 15 keV.

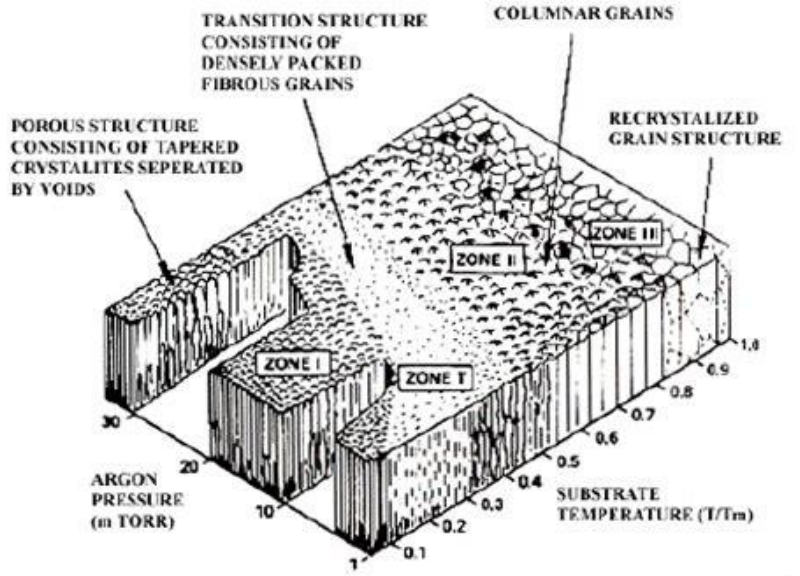

Figure 86 – The structure zone model (SZM) describes the film growth of sputter deposition depending on substrate temperature and argon pressure. ***[1]***

The HDAsB-image (Fig. 87) of the surface of layer RR69 indicates again that columnar growth of the copper precipitations (dark). It seems as if the larger and smaller copper dots are surrounded by elemental lead and lead-copper precipitations.

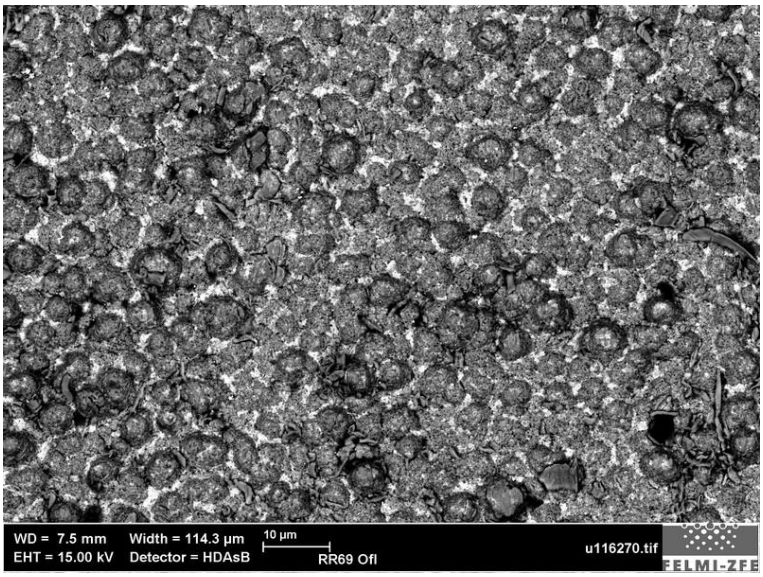

Figure 87 - CuPb25 (RR69). The BSE-image illustrates the compositional contrast of the CuPb25 film (RR69). It seems as the columnar copper precipitations grow out of the surface and appears as dark dots which are surrounded by lead (brighter areas). HDAsB-detection and 15 keV.

The next SE-image shows that the hem on the CuPb25 film appears very voluminous. This indicates again that this film might be an oxide layer. It seems that a fine gap is present between the CuPb25 layer and the hem.

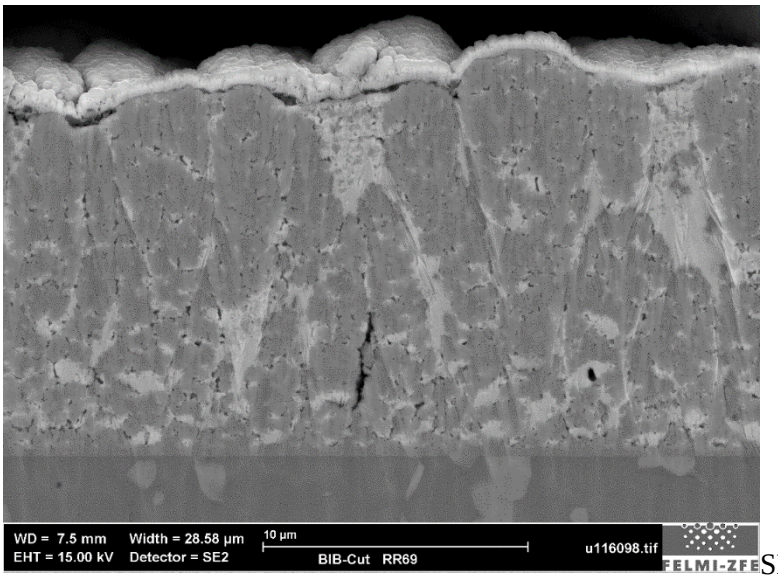

SE

Figure 88 – CuPb25 (RR69 BIB cut). This image shows that the hem does not directly grow on the metal film and appears very voluminous. Thus, a pure oxide layer can be excluded. SE-detection and 15 keV.

To confirm the assumption that the lower part of the CuPb25 film has a higher concentration of lead than the upper part, two areas (Zone 1 and Zone 2) were analyzed and quantified with SEM-EDS (Fig. 89 and 90). This measurement was performed twice at different positions within the film to show the reproducibility (Table 20 and 21). The upper part Zone 1 shows a significant higher concentration of Pb (11 wt%). Also small amount of Fe is detected in both zones. The average composition of the lower part is similar to those of the AAS analysis, whereas the upper zone totally deviates from the reference value.

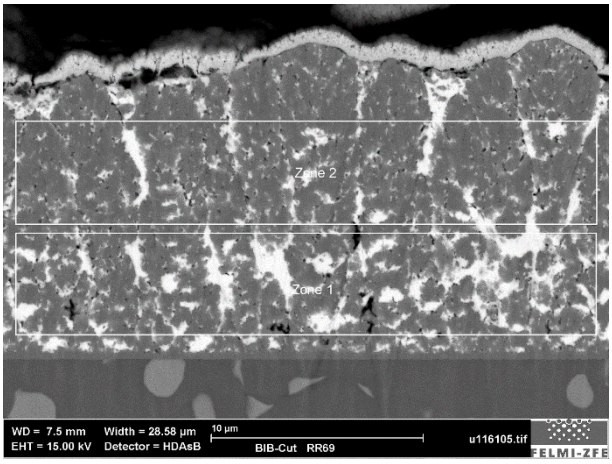

Figure 89 – CuPb25 (RR69 BIB cut). Selected areas for the quantitative analysis with EDS to show the differences in amount of lead between the upper and lower area in the CuPb25 film. The results are listed in Table 20. HDAsB-detection and 15 keV.

Table 20 – The average composition of the selected areas shown in Figure 89.

	Zone in image		
Element	*AAS [wt%]*	*1 [wt%]*	*2 [wt%]*
Cu K-line	69.00	66.53	77.94
Pb M-line	31.00	31.41	20.46
Fe K-line	-	2.06	1.60

For the next quantitative analysis, additional to the scan of Zone 1 and 2 an overall scan (US) was performed (Fig. 90). It shows the same trend as the previous measurement. The lower part has a higher amount of Pb compared to the upper part and confirms the optical impression of the BSE-images. The Pb content of the overall area (Zone US) is about 4 wt% lower than the AAS measurement yields.

However, the mean of the two areas is about the composition of the overall scan. Therefore, the accuracy of the AAS measurement is doubtful. Possibly the complex structure and the inhomogeneity lead to falsification of the AAS reference measurements. Both quantitative analyses show that the amount of iron in the lead-rich regions is about 1 wt% higher than in the copper-rich part of the CuPb25 film. Possibly the elemental lead target ran out of Pb during the deposition process and therefore Fe from the target substrate was sputtered. This phenomenon was already observed for layer RR32 (Cu9Pb) (Chapter 6.2.3).

Table 21 – The results of the quantitative analysis of the three selected areas shown in Figure 90 are listed. It was measured again the upper and lower region of the film to illustrate the difference and additional an overall scan (US) was performed to determine the average composition across the whole film.

	Zone in image			
Element	*AAS [wt%]*	*1 [wt%]*	*2 [wt%]*	*US [wt%]*
Cu K-line	69.00	62.18	77.35	70.76
Pb M-line	31.00	35.31	21.39	27.29
Fe K-line	-	2.51	1.26	1.95

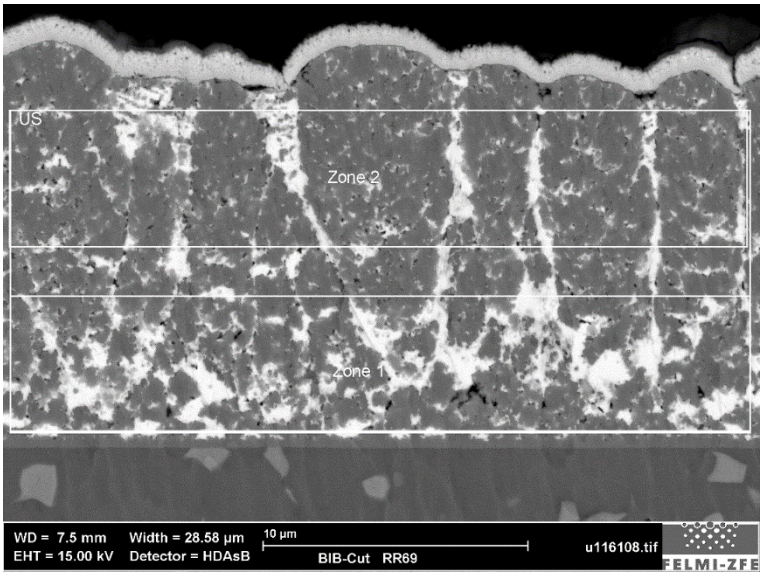

Figure 90 – CuPb25 (RR69 BIB cut). Selected areas Zone 1, Zone 2 and US for the quantitative analysis of RR69. The results are listed in Table 21. HDAsB- detection and 15 keV.

Moreover, selected positions shown in Figure 91 were analyzed with SEM-EDS to show the compositional contrast within the layer of layer RR69. The spectra of EDS analysis show again that lead- rich (bright, +1) and copper-rich (dark, +2) areas are present within the film. Regions with higher amount of Pb contain iron, which confirms the assumption that the lead target possibly ran out of Pb during sputtering. It further affirms that the formation of more phases with different compositions at these sputtering conditions is present (Cu-Pb-phase diagram Chapter 4.4.1).

Position +3 shows that the hem consists of almost copper, lead and oxygen compared to other positions within the layer. Thus, it is suspected that the thin coating on the surface of the CuPb25 film is an oxidized lead and copper layer and do not arise from residues from re-deposition. Moreover, a small amount of Fe is again present in the hem.

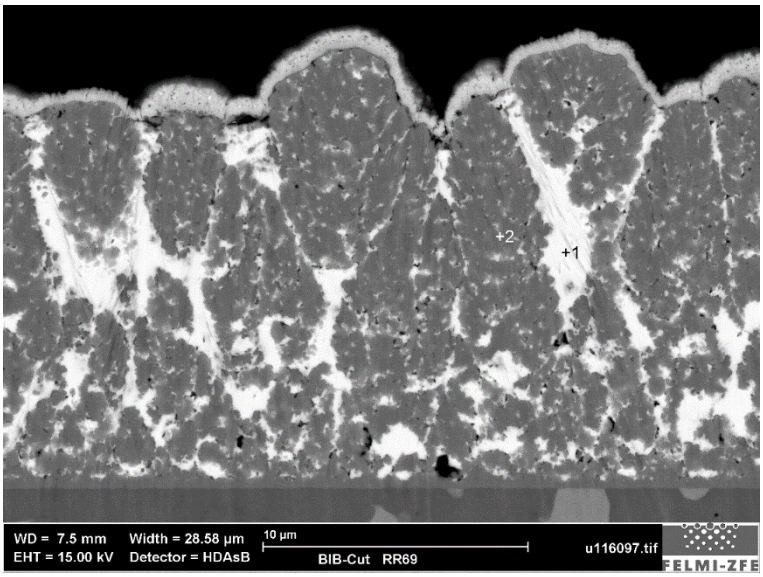

Figure 91 – CuPb25 (RR69 BIB cut). Position +1 and +2 are selected to show the composition contrast within the CuPb25 film. HDAsB- detection and 15 keV.

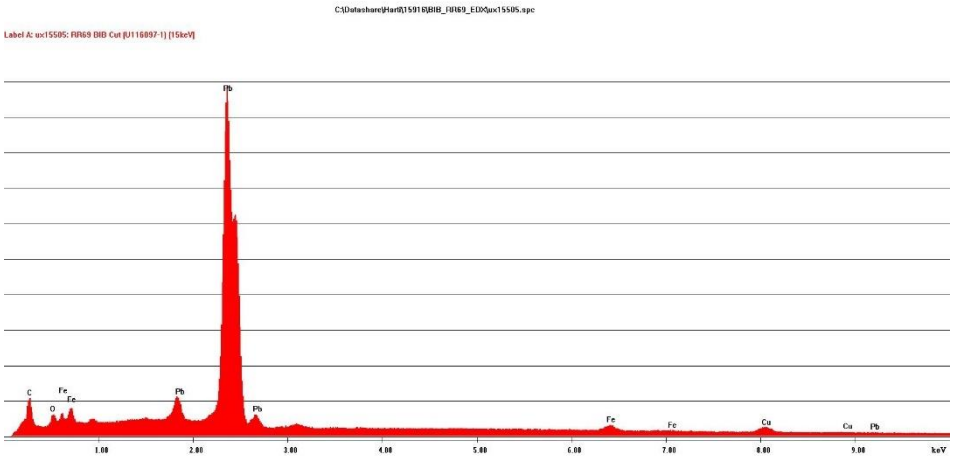

Figure 92 – CuPb25 (RR69 BIB cut). EDS spectrum of position +1 of Figure 91 illustrates the desired high amount of Pb. Less Fe and Cu is also present.

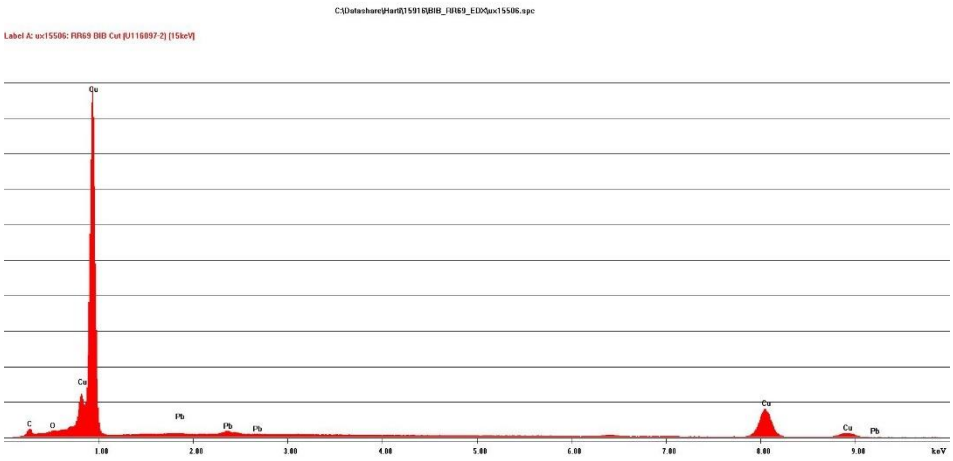

Figure 93 – CuPb25 (RR69 BIB cut). The EDS spectrum of position +2 of Figure 91 shows a huge amount of copper and barely lead.

In the following image (Fig. 94) small copper precipitations are found within the lead-rich regions. These precipitations seem to be continuing in copper-rich regions, where the copper crystals overlap and therefore it appears as one continuous phase with a high concentration of copper platelets. The quantitative analysis confirms again the visual assumption of the BSE- images of the CuPb25 layer, that position +2 is richer in copper than the brighter phase +1 (Fig. 94) and it shows the higher the lead content the higher is the amount of Fe. Those hexagonal-like structures of copper precipitations were already identified for layer RR34 (CuPb23Sn3) and RR57 (CuPb23Sn3).

This is an advantage of the BIB-cut preparation, that crystal structures can be revealed without smearing polishing agents or soft materials from the layer across the whole film.

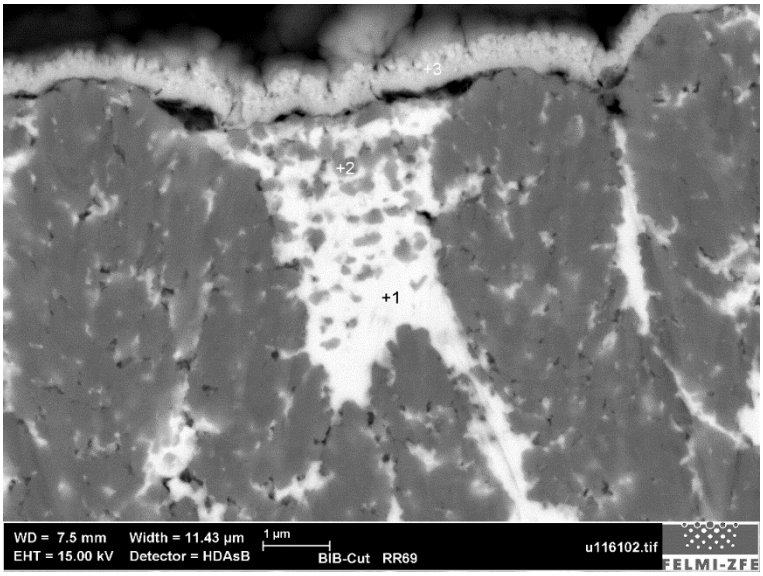

Figure 94 – CuPb25 (RR69 BIB cut). This image shows small copper precipitations within the brighter lead-rich phase. To confirm the two-phase structure of this film two selected areas +1 and +2 were analyzed. HDAsB- detection and 15 keV.

With broad- ion- beam preparation slight waves (nm range) especially on the steel substrate arise. These result from the BIB-cut preparation due to different material removal rate. Since the film consists of

different phases and crystal structures, material is removed at different rates and leads to a slightly wavy surface. Moreover, the longer the ion beam gets, the more it is split, which also results in a various material removal rates.

6.2.5.1 Comparison of Broad-Ion-Beam and Conventional Polishing Preparation Method

The high portion of lead within the alloy layers causes problems during the polishing preparation. It is smeared across the whole multilayer system and leads to changes in the appearance of the structure and in composition. Moreover, residues form the polishing materials are preferably accumulated in gaps and pores within the layers and on the surface of the polished cross-section, which also falsify the quantification. Nevertheless, the determined average composition of the single layers within the graduated layer system partially shows very similar values to the expected composition, especially the CuSn6 layers. However, lead-rich films partly strongly deviate from the desired composition, since lead is mostly very irregular distributed within the film. This leads to the formation of lead- rich and copper-rich areas and thus problems in quantification arise. The absorption of generated electrons by lead also leads to problem in quantification by EDS but this difficulty cannot be improved by an optimized sample preparation.

With the broad-ion-beam method the smearing of soft components can be avoided but re-deposition of the elements cannot be completely excluded. As well the quantification of a CuPb25 film with the BIB-cut deviates from the AAS value, probably due to the irregular distribution of lead within the film and the formation of areas within the films containing more or less lead. Due to the high costs of the broad-ion-beam device itself and each single preparation and the high time expense of a BIB-cut, it is not suitable for the implementation in serial monitoring of multilayer systems. Therefore, the polishing methods must be improved by several experiments by changing polishing agents and embedding material for example.

6.2.6 CuPb23Sn3 (RR27)

The sputtered film on sample RR27 consists of copper, lead and tin and should ideally have a composition of CuPb23Sn3 as RR34. However, the results of the AAS measurement are 87.46 wt% Cu, 8.28 wt% Pb and 4.26 wt% Sn. In contrast to RR34 the deposition process was started on a cold (room temperature) substrate. Therefore, the temperature during sputtering does not exceed 150 °C.

For the deposition, a CuSn6 alloy target, an elemental copper and an elemental lead target were used.

6.2.6.1 Investigation of the Untreated Surface

In Figure 95 the film appears relatively homogenous with some larger precipitations. The lines across the whole layer, resulting from the stainless-steel sheet production are depicted trough the thin film.

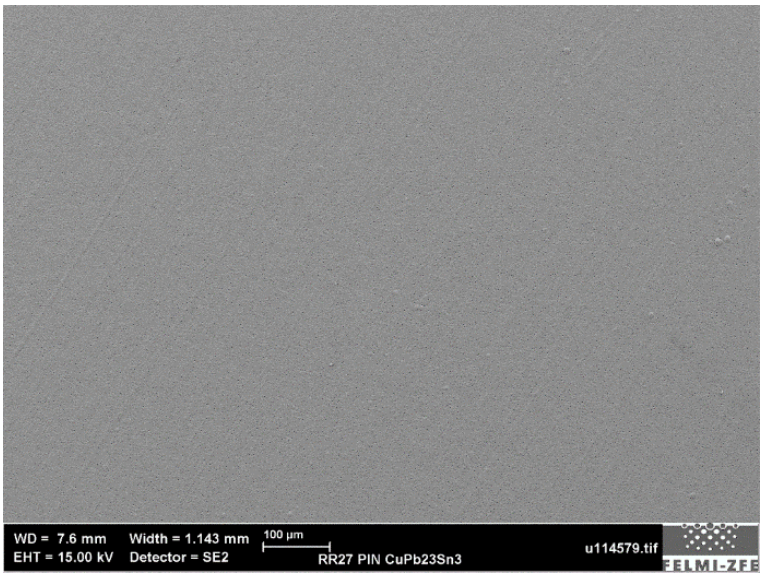

Figure 95 - This area is used for the determination of the average composition of the film with EDS. It appears very homogenous with some larger precipitations. The lines from the substrate which are depicted trough the thin layer are also shown. SE detection and 15 keV.

The detection of secondary electrons in Figure 96 shows a dense granular morphology with smaller and larger grains. In general, the structure of layer RR27 appears coarser-grained than RR34. The reason can be that RR34 was warm started and, therefore, the sputtering process happens at higher temperatures up to 250 °C compared to RR27, which was started on a substrate at room temperature. The much lower amount of lead in the layer can influence the film growth as well.

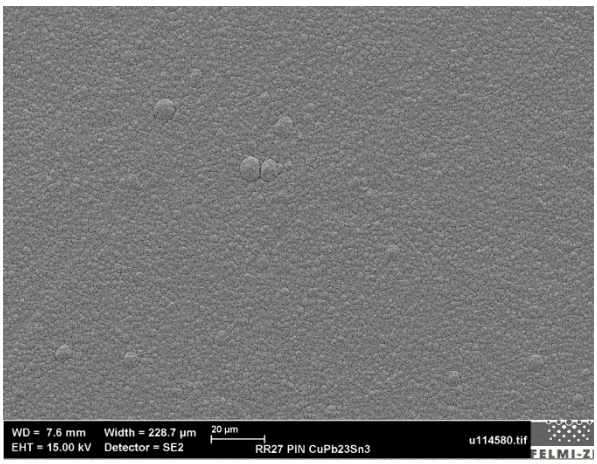

Figure 96 - CuPb23Sn3 (RR27). This image illustrates the granular structure of RR27 "cold start" recorded with SE detection system and 15 keV. Smaller and larger grains are present.

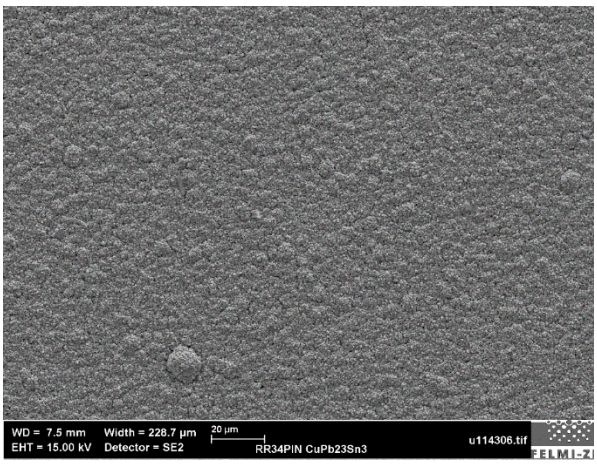

Figure 97 - CuPb23Sn3 (RR34). The image shows a finer granular structure compared to RR27 probably due to higher process temperatures ("warm start") or the lower amount of Pb in the layer.

The compositional contrast detected with HDAsB in Figure 98 shows less brighter regions compared to RR34 due to the lower amount of Pb in the film. The darker areas prevail as expected.

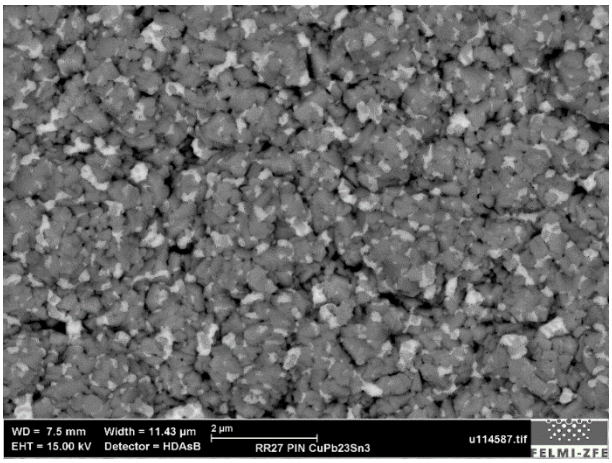

Figure 98 - CuPb23Sn3 (RR27). This image illustrates the compositional contrast of the CuPbSn film detected with 15 keV and HDAsB detection system.

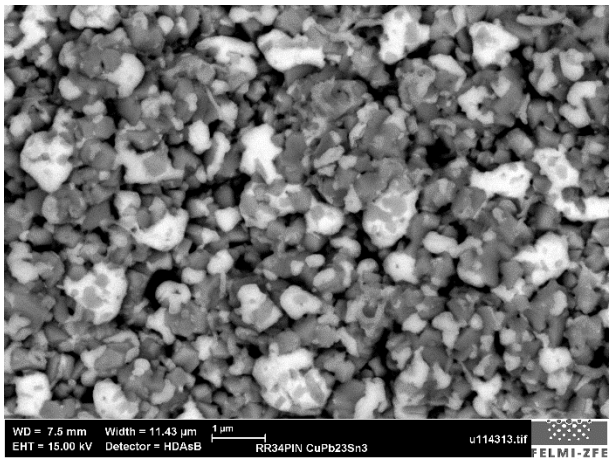

Figure 99 - CuPb23Sn3 (RR34). This image illustrates more brighter regions (lead rich) compared to RR27 (left).

The average composition of the CuPbSn film was determined by scanning the area of Figure 95 with SEM-EDS. The EDS results listed in Table 22 measured with an acceleration potential of 15 keV slightly deviate from the AAS measurements. The determined tin content is almost the same, whereas the copper and lead content measured with EDS are about 2 wt% lower. The results measured with 7 keV again strongly deviate from the AAS values. Copper is strongly undervalued, and lead is overvalued, maybe due to the higher geometry effects closer to the surface.

Table 22 -Average composition of the CuPbSn film determined at 15 and 7 keV. Therefore, the whole area of Figure 95 was scanned.

	AAS	15 keV		7 keV	
Element	*[wt%]*	*[wt%]*	*[at%]*	*[wt%]*	*[at%]*
Sn L-line	4.26	4.44	2.62	6.59	4.13
Cu K-line	87.46	85.43	93.97	76.86	89.93
Pb M-line	8.28	10.13	3.42	16.55	5.94

The quantitative analysis of the selected positions in the CuPb23Sn3 film (Fig.100) confirms again that this kind of CuPbSn alloy consists of different phase compositions. However, the measurement with 15 keV illustrates that the brightest position +3 contains 52 wt% copper and 44 wt% lead contrary to the expectations. Position +2, which also appears relatively bright contains significantly more copper than lead and the darkest area +3 is rich in copper as expected due to the coloring. These results, which do not really correspond to the coloring due to the compositional contrast, might arise due to the large interaction volume from electron beam with an acceleration potential of 15 keV. Thus, elemental copper or copper-rich areas, which are directly positioned below the bright selected positions, influence the result and increase the measured copper content.

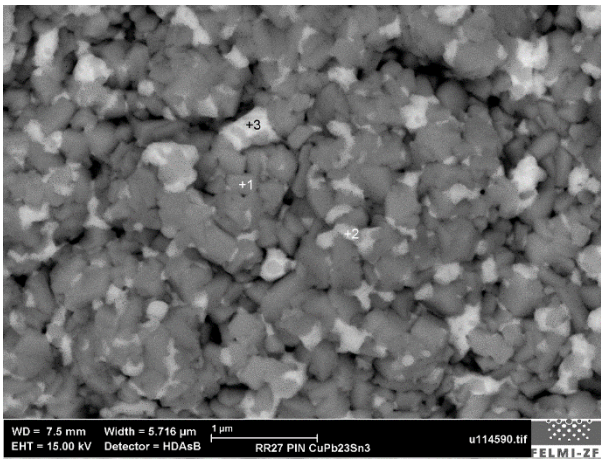

Figure 100 - CuPb23Sn3 (RR27). The image shows the selected areas for the quantitative analysis (Table 23) detected with 15 keV and HDAsB detection system.

Table 23 -The composition of the three selected areas from Figure 100 recorded at 15 keV.

	Position in image		
Element	*+1 [wt%]*	*+2 [wt%]*	*+3 [wt%]*
Sn L-line	4.83	3.97	3.59
Cu K-line	88.86	67.71	52.71
Pb M-line	6.31	28.32	43.71

However, the quantitative analysis of selected areas (Fig.101) at 7 keV confirm the trend of the CuPb23Sn3 layer. The brighter the area the more lead is present. The darker regions are rich in copper and contain more tin (Table 24), which can be explained by the better solubility of tin in copper compared to tin in lead (Chapter 4.4). Due to smaller interaction volume, less information from the surrounding is gained, and, thus the EDS results better correspond to the expectations due to the coloring of composition contrast. However, at lower acceleration potential, geometry effects influence the investigation with SEM-EDS more.

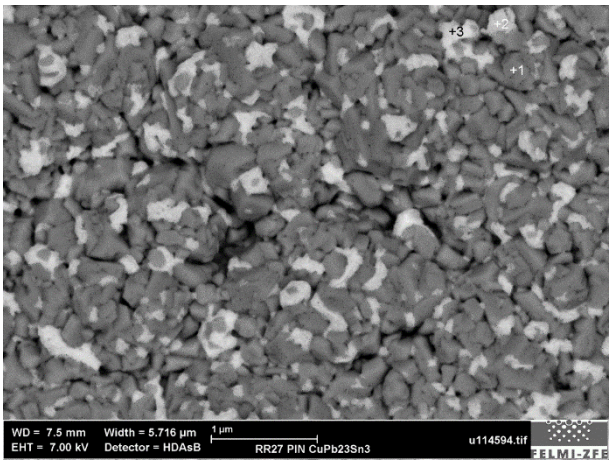

Figure 101 - CuPb23Sn3 (RR27). Image was recorded with 7 keV and HDAsB detection system. Three areas were selected for the quantitative analysis to show the compositional contrast (Table 24).

Table 24 -Composition of the three selected areas in Figure 101 recorded at 7 keV.

	Position in image		
Element	*+1 [wt%]*	*+2 [wt%]*	*+3 [wt%]*
Sn L-line	4.94	1.57	0.71
Cu K-line	94.22	26.88	25.19
Pb M-line	0.84	71.54	74.1

Both measurements show that the lead rich regions are more oxidized than copper rich areas. However, at 7 keV the amount of oxygen is higher than at 15 keV, since the information for the quantitative analysis is gained from an interaction volume closer to the surface and oxidations exclusively happen at the surface.

Further investigations of a polished cross-section of RR27 were not carry out, since the layer strongly deviates from the desired composition CuPb23Sn3.

6.2.7 CuPb23Sn3 (RR29)

The sputtered layer of sample RR29 should ideally have the composition CuPb23Sn3.The deposition was started on a cold (room temperature) substrate. Thus, the temperatures within the magnetron system reach a maximum of 150 °C. RR29 and RR27 undergo the same process conditions.

The AAS measurements show that the deposited film consists of 80.95 wt % copper, 15.21 wt% lead and 3.84 wt% tin. For the deposition, a CuSn6 alloy target, an elemental copper and an elemental lead target were used as sputtering sources.

6.2.7.1 Investigation of the Untreated Surface

At low magnification, the image in Figure 102 appears rougher compared to RR34 and RR27. Fine and coarse lines are visible across the whole layer, resulting from the structure of the stainless-steel band used as substrate.

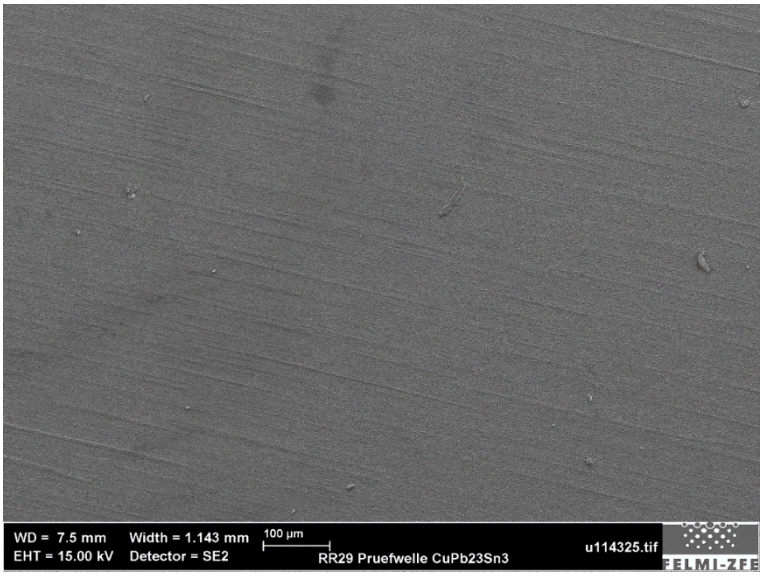

Figure 102 – CuPb23Sn3 (RR29). This SE- image shows a relatively rough structure of the film. Finer and coarser lines and grater precipitations are already visible.

The next picture Figure 103 shows two phases within the film, a granular structure and some conspicuous broader lines on the surface of the film. It seems as if the composition of those phases varies due to the different coloring of the HDAsB image. Therefore, two area spectra were recorded (Fig.104). At higher magnification the granular morphology appears very porous, especially in the copper-rich areas (Fig.104).

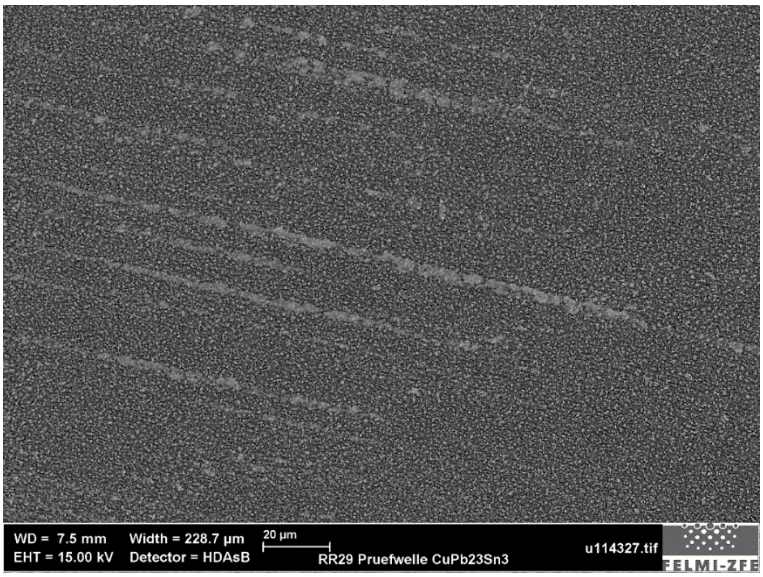

Figure 103 - CuPb23Sn3 (RR29). This image illustrates a film consisting of two or more phases.

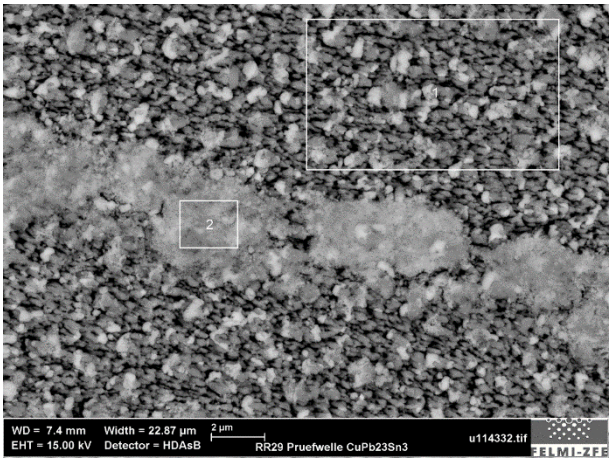

Figure 104 - CuPb23Sn3 (RR29). The image recorded with HDAsB detection system clearly shows the compositional contrast of the two phases in layer RR29.

Table 25 – Results of the quantitative analysis of the areas from Figure 104, measured at 15 keV.

	Area in image	
Element	*1 [wt%]*	*2 [wt%]*
Sn L-line	3.43	2.69
Cu K-line	70.57	47.58
Pb M-line	26.00	49.73

The quantitative analysis (Table 25) shows that the darker area 1 is rich in copper, whereas the brighter area 2 consists of almost the same amount of copper and lead. The tin content in both areas is very similar.

Figure 105 again shows that the structure of layer RR29 is more porous than sample RR27 and RR34. A possible reason for the more compact structure of RR34 is the higher temperature during the puttering process. The deposition of RR29 was performed at a maximum of 150 °C (cold start), whereas RR34 was started warm and reaches a temperature around 250°C while sputtering.

The differences in morphology also arise through the different compositions of the CuPbSn alloy. RR29 contains almost twice as much lead compared to RR27. Thus, the higher amount of lead might be the reason for the porous film growth.

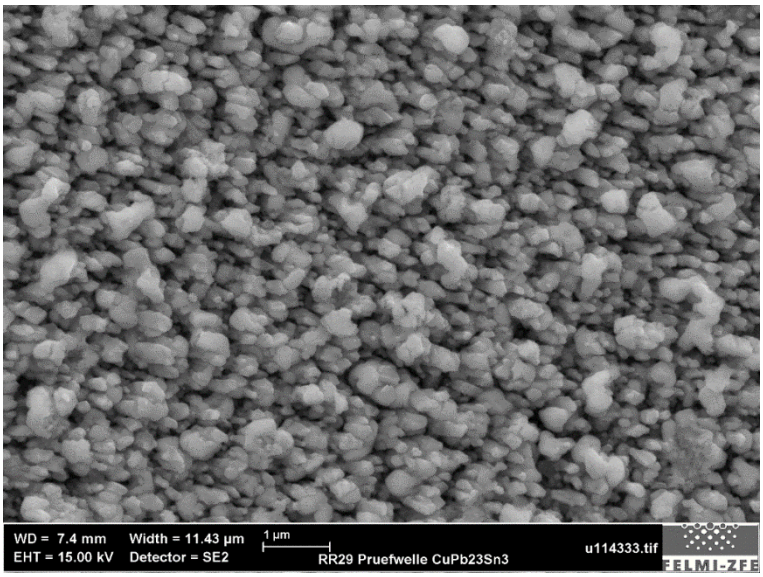

Figure 105 – CuPb23Sn3 (RR29). This image shows the porous granular morphology of the sputtered layer.

To determine the compositional differences within the film, selected positions were quantified with EDS. The measurements at 15 keV confirm the expectations (Fig.106). The brighter area +1 is very rich in Pb and the darker area +2 contains significantly more copper (Table 26).

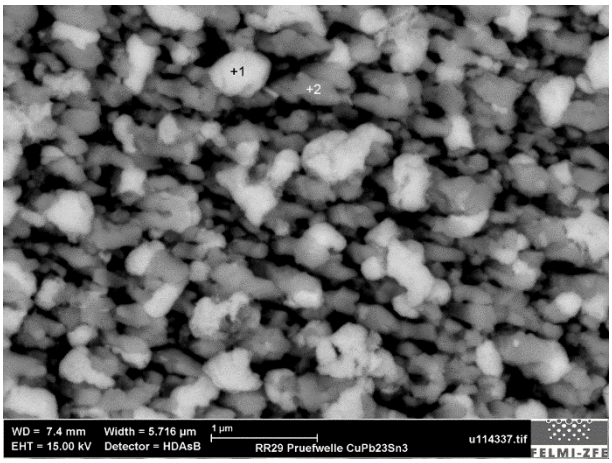

Figure 106 – CuPb23Sn3 (RR29). This figure shows two selected positions for the quantitative analysis with EDS at 15 keV.

Table 26 – Quantitative analysis of selected positions in the film to demonstrate the two-phase system of the CuPbSn alloy at 15 keV.

	Position in image	
Element	*+1 [wt%]*	*+2 [wt%]*
Sn L-line	1.94	4.03
Cu K-line	27.84	82.66
Pb M-line	70.23	13.31

Due to the quantitative analysis at 7 keV, the two-phase structure becomes more obvious (Fig.107). The area +1 contains about 91 wt% lead and the area +2 about 89 wt% copper. The difference in results to 15 keV can be explained by the smaller interaction volume. Thus, less information from the surrounding is gained. Moreover, the results show again that the solubility of tin in copper is better than tin in lead.

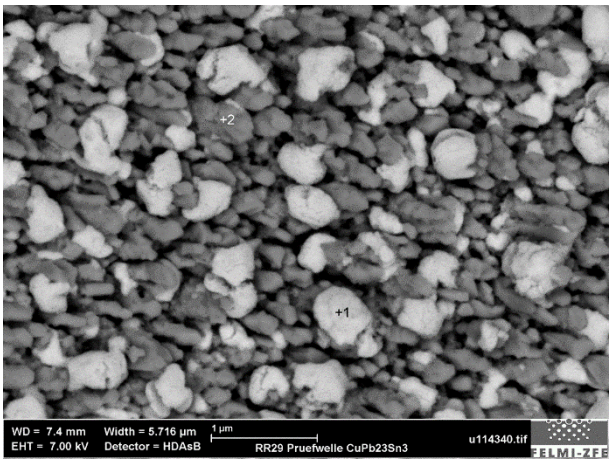

Figure 107 – CuPb23Sn3 (RR29). This image illustrates the two positions selected for the quantitative analysis with EDS at 7 keV.

Table 27 – Results of the quantitative analysis of the selected areas (Fig.107) at 7 keV

	Position in image	
Element	*+1 [wt%]*	*+2 [wt%]*
Sn L-line	1.89	5.27
Cu K-line	5.68	88.73
Pb M-line	92.46	5.99

The investigation of the polished cross-section of layer RR29 was not performed, since it shows a large area phase separation (Fig. 103 and 104 and Table 25).

6.2.8 CuPb23Sn3 (RR34)

The sputtered film on sample RR34 should ideally have the composition CuPb23Sn3 (74 wt% Cu, 23 wt% Pb and 3 wt% Sn). The AAS reference measurements of RR34 show an average composition of 71.96 wt% copper, 24.52 wt% lead and 3.52 wt% tin. This values only slightly deviate from the desired composition CuPb23Sn3.

The sputter process was started on a warm substrate. The start temperature within the system is about 200 °C and reaches about 250 °C during the deposition process. For the deposition of the CuPb23Sn3 film a CuSn6 alloy, an elemental copper and an elemental lead target was used to reduce the tin content of CuSn6 and to increase the Cu and Pb content for the desired CuPb23Sn3 film. A deposition from an CuPbSn or CuPb alloy is difficult due to the different mass of the elements. (Chapter 4.2.13).

6.2.8.1 Investigation of the Untreated Surface

At low magnification the CuPb23Sn3 film appears relatively homogenous. The lines covering the whole layer as shown in sample PVD03-206 resulting from the substrate surface are also detected.

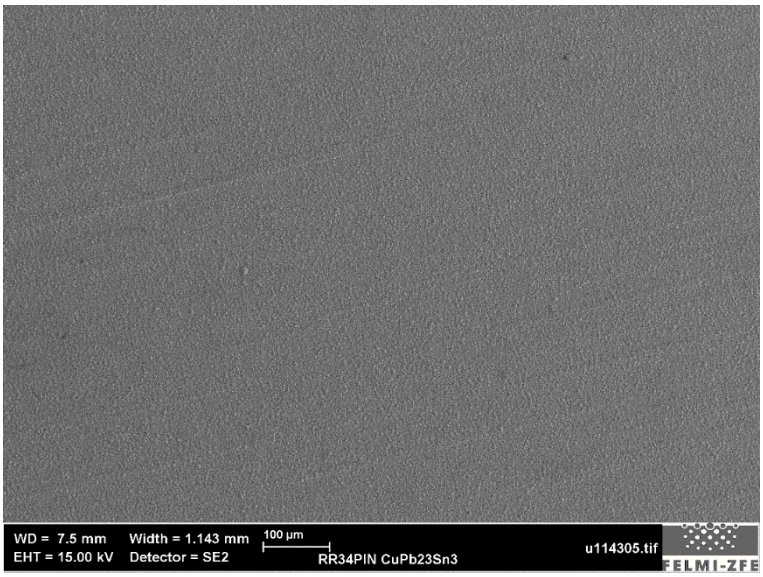

Figure 108 –CuPb23Sn3 (RR34). Image shows a relatively homogenous structure. 15 keV and SE detection system.

The following image (Fig.109) illustrates the CuPb23Sn3 film recorded at 15 keV. It shows that a homogenous fine granular structure is interrupted by larger spherical precipitations. To demonstrate the material contrast and the porosity of the CuPb23Sb3 film a HDAsB image at was also recorded.

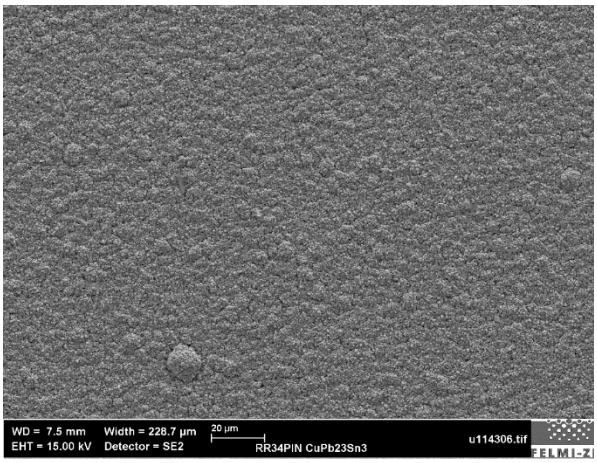

Figure 109 – CuPb23Sn3 (RR34). This image shows some larger precipitations on the surface of the film. 15 keV and SE detection system.

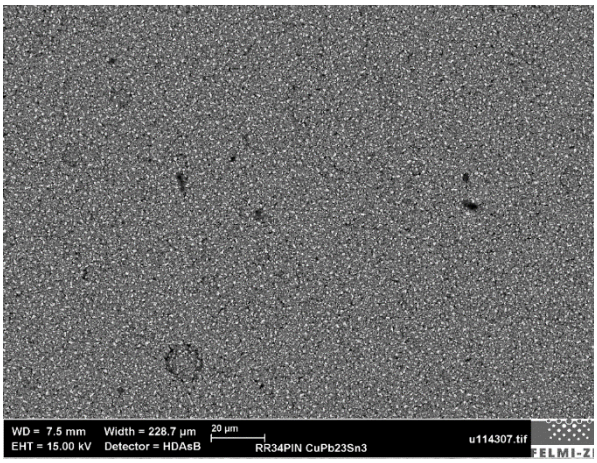

Figure 110 – CuPb23Sn3 (RR34). In the HDAsB-image the structure appears porous and a material contrast is clearly recognizable. HDAsB detection system and 15 keV.

At higher magnifications the film appears as a very voluminous popcorn-like structure. (Fig.111). The imaging with the HDAsB detector (Fig.112) suggests that the film consists of two phases with different composition. Bright and dark areas are illustrated. Thus, copper-rich and lead-rich precipitations are suspected. Some larger positions indicate a hexagonal structure, which is likely for elemental copper precipitations.

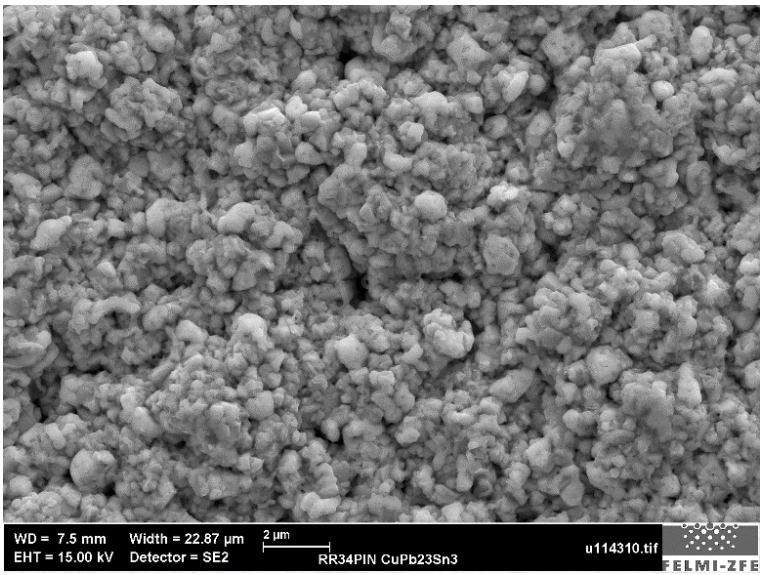

Figure 111 - CuPb23Sn3 (RR34). Image of CuPb23Sn3 film recorded by the detection of secondary electrons. The layers resemble a voluminous popcorn-like structure.

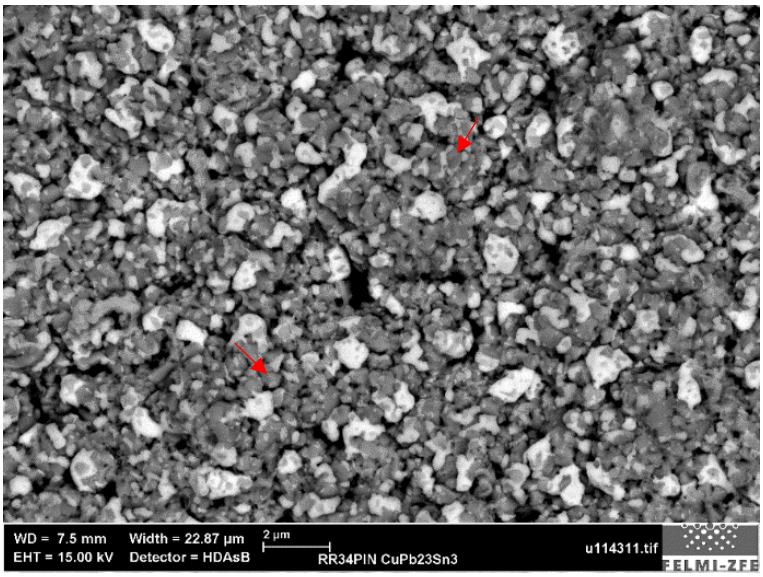

Figure 112 - CuPb23Sn3 (RR34). Image of CuPb23Sn3 film recorded by the detection of backscattered electrons to visualize the compositional contrast. Larger and hexagonal structures (red arrow) appear, which are likely for elemental copper precipitation.

The quantitative analysis of the area of Figure 108 (Table 28) shows that the average composition deviates from the desired composition (74 wt% Cu, 23 wt% Pb, 3 wt% Sn). The lead content is about 3 wt% and the tin content about 1 % higher (15 keV). However, these results are strongly influenced by the geometry effects, and, therefore it is difficult to judge the accuracy of the measurement method. However, the reference values form AAS measurements deviate less than 1 wt% from the values determined by SEM-EDS measured at 15 keV.

Table 28 – Results of the quantitative EDS analysis of the CuPn23Sn3 film. Therefore, an area scan of the image of Figure 108 at 15 and 7 keV was performed. The lead content is about 3 wt% higher and the tin content is about 1 wt% higher than the desired composition of the film.

	AAS	15 keV		7 keV	
Element	*[wt%]*	*[wt%]*	*[at%]*	*[wt%]*	*[at%]*
Sn L-line	3.52	4.14	2.77	6.07	4.54
Cu K-line	71.96	70.02	87.35	57.07	79.68
Pb M-line	24.52	25.84	9.88	36.86	15.78

At an accelerating potential of 7 keV the deviation is significantly higher, and the lead content is extremely overvalued. The heavy element lead is responsible for high geometry effects and absorption, which show more influence at lower acceleration potential.

At an acceleration potential of 7 keV, it seems, that the brighter phase covers the film with streak-like structures. However, the hexagonal structures are still visible as shown in Figure 113.

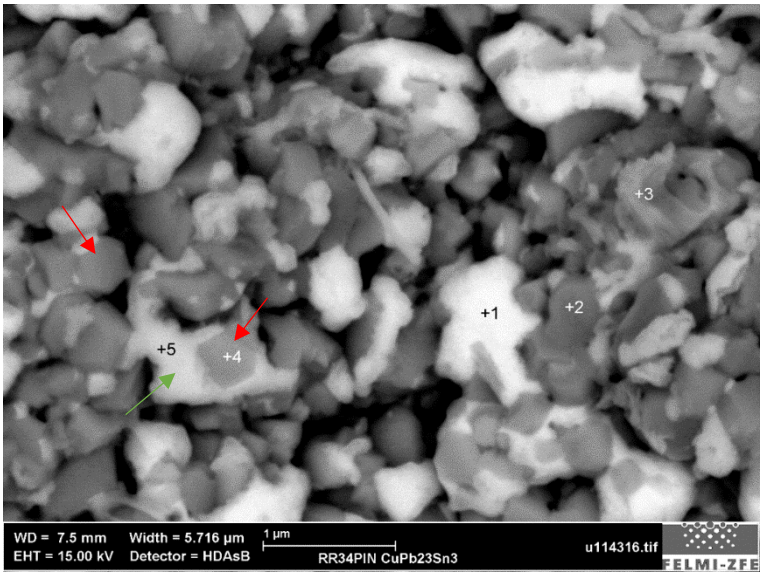

Figure 113 – CuPb23Sn3 (RR34). This image shows bright streak-like structures (green arrow) covering darker regions, and hexagonal copper (red arrow) structures (position +4) recorded with 15 keV and HDAsB detection system.

The quantitative analysis of selected areas (Fig. 114) shows that the composition strongly varies from position to position, as expected. Position +1 consists of 85 wt% Pb (1 wt% Sn and 14 wt% Cu) and confirms the assumption due to the bright coloring. The composition of the hexagonal and darker position +2 is about 80 wt% copper, 16 wt% lead and 4 wt% tin. Position 3 and 4 are very similar in its composition and position 5, which is significantly brighter than 2, 3 and 4 contains more Pb (60 wt%). These results confirm the very inhomogeneous and multiphase structure of the CuPb23Sn3 sputter film.

Table 29 – Results of quantitative analysis of selected position shown in Figure 114.

	Position in image				
Element	*+1 [wt%]*	*+2 [wt%]*	*+3 [wt%]*	*+4 [wt%]*	*+5 [wt%]*
Sn L-line	1.36	4.47	4.48	3.79	2.86
Cu K-line	14.39	78.75	63.18	69.16	38.18
Pb M-line	84.25	16.78	32.33	27.05	58.96

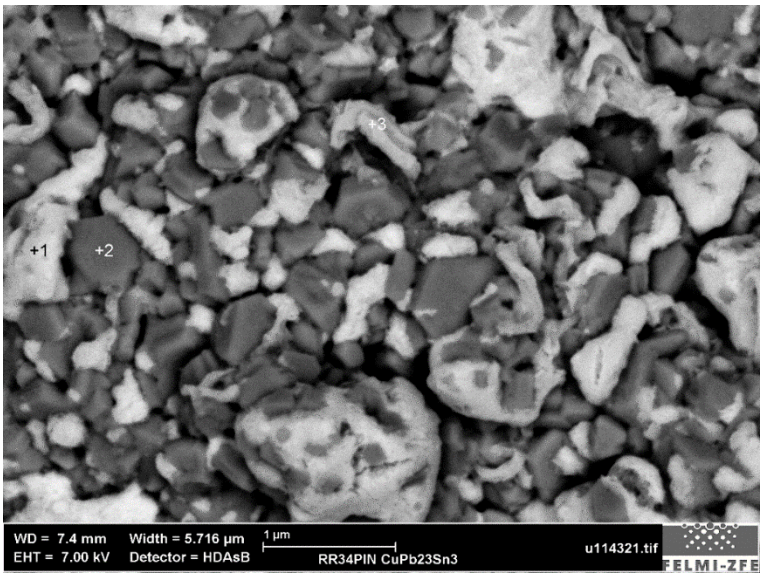

Figure 114 – CuPb23Sn3 (RR34). HDAsB image of layer RR34 recorded at 7 keV.

The image recorded at 7 keV (Fig. 115) confirms the trend of the 15 keV spectrum. Position +1 consists of almost pure lead (90 wt%). The hexagonal structure at position +2 contains 90 wt% copper. The composition of position +3 is about 70 wt% Pb, 30 wt% and 1 wt% Sn. The higher content of copper and lead compared to the comparable positions in Figure 114 results from the lower acceleration potential. Thus, the interaction volume is smaller and, therefore, less information from the surrounding (underlying layers) is gained. At higher acceleration potential of 15 keV possibly layers underneath the measurement point are also quantified and, therefore, falsify the result. In the EDS spectra the content of oxygen and carbon, especially oxygen, is significantly higher at brighter positions, which contains more Pb, since the oxidation potential of Pb is higher compared to Cu.

The InLens image of the CuPb23Sn3 film in Figure 115 shows tiny dots at the film at very high magnification. Due to the limited resolution of the EDS (2 µm), these formations cannot be quantified. However, this could be small Sn precipitations or CuO, which grows on the surface. The compositional contrast strongly indicates fine tin precipitations.

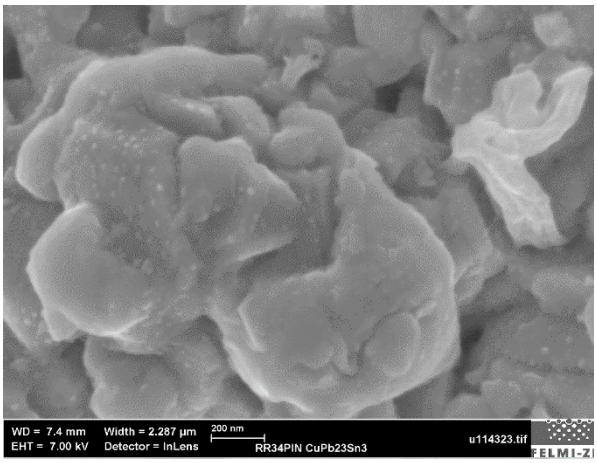

Figure 115 – CuPb23Sn3 (RR34). This image shows bright small dots at the structure surface. It was recorded at 7 keV and with InLens detector.

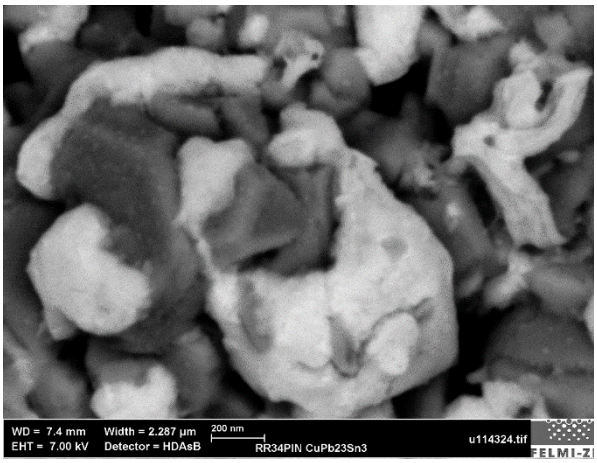

Figure 116 – CuPb23Sn3 (RR34). In this picture the compositional contrast with HDAsB detector at 7 keV is illustrated.

According to the phase diagram of Cu-Pb (Chapter 4.4.1), the formation of the two- phase structure of the CuPb23Sn3 film consisting of copper rich (dark areas) and lead rich areas (bright areas) can be roughly explained. Below 326 °C elemental copper and lead phases are present. If indeed elemental copper and lead are present in the film, is difficult to investigate with EDS, because due to the interaction volume of the electron beam, information from the surrounding is taken into the evaluation.

The higher amount of tin in copper rich areas is explained due to the higher solubility of tin in copper compared to tin in lead (Chapter 4.4). Nevertheless, it must keep in mind that the phase diagrams of Cu/Pb and Cu/Sn are valid for the precipitation from the liquid phase, but the sputter process is based on the precipitation from the gas phase.

6.2.8.2 Investigation of the Polished Cross-Section

The polished cross-section of layer RR34 was prepared with Method 1 explained in Chapter 5.3.

In the following (Fig. 117) image the surface of the sputtered film appears very rough but homogenous within the layer.

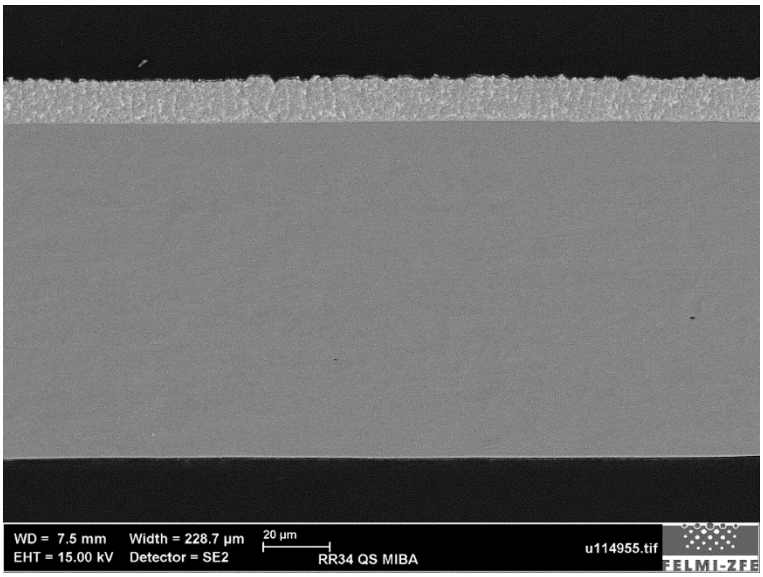

Figure 117 - CuPb23Sn3 (RR34). This image was recorded with 15 keV and SE detection system. It shows a relatively homogenous structure of the RR34 with a rough surface

The following image shows a blocky and the typical two-phase structure for this type of CuPbSn alloy. Moreover, a narrow band between embedding material and CuPbSn film appears. This consists of elemental copper and was deliberately deposited as gradient layer. The quantitative analysis of area 1 (Fig. 118) shows that the results (Table 30) at 15 keV only slightly deviates (maximum 2 wt%) from the reference value of the AAS measurement. The results gained at 7 keV vary more, but nevertheless, these values fit better than those from the untreated surface recorded at 7 keV. These results show again the importance of a carefully prepared polished cross section to avoid geometry effects due to rough and voluminous untreated layer surfaces.

Table 30 – Results of the quantitative analysis of the area 1 shown in Figure 118.

	AAS	15 keV	7 keV
Element	*[wt%]*	*[wt%]*	*[wt%]*
Sn L-line	3.52	4.29	4.5
Cu K-line	71.96	73.6	78.43
Pb M-line	24.52	22.11	17.08

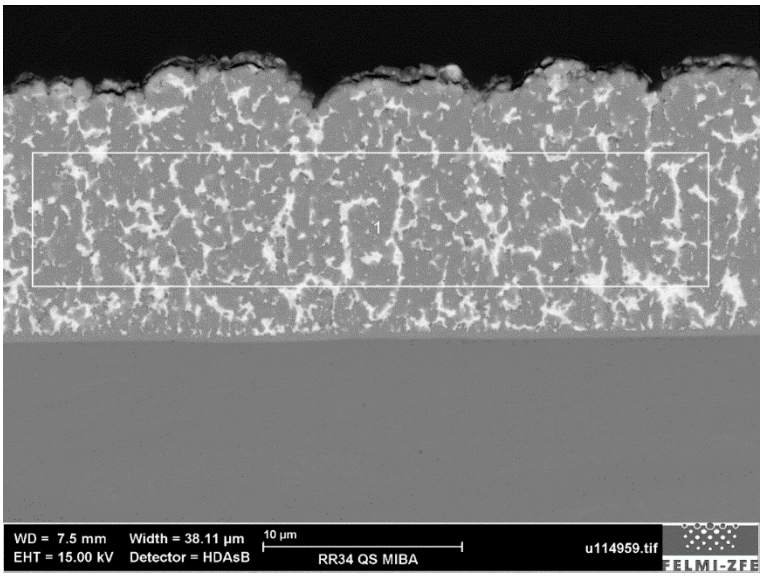

Figure 118 - CuPb23Sn3 (RR34). The area 1 was used to determine the average composition of the polished cross-section of RR34 recorded with an acceleration potential of 15 keV and HDAsB detection system.

In general, it seems as if the cracks, probably resulting from the blocky construction of copper rich phases, are filled with elemental lead or lead rich phases shown as brighter areas (Fig. 119). Figure 119 and 120 show that the bright lead-rich areas shown with HDAsB appear deeper located at the image taken with SE detector. Possibly parts of the smooth metal lead are pulled out of the film during the polishing process.

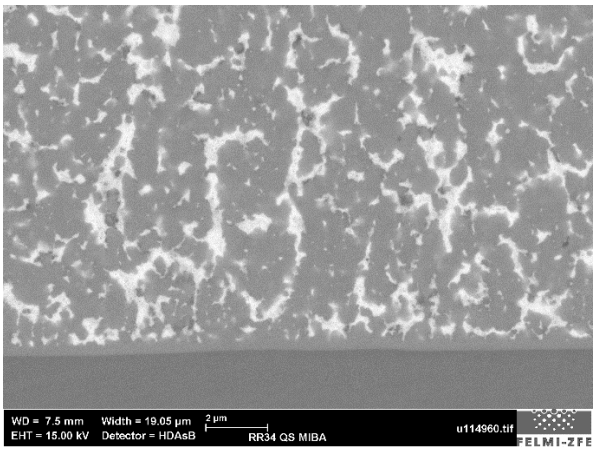

Figure 119 – CuPb23Sn3 (RR34). Compositional contrast shown by HDAsB detection. and 15 keV acceleration potential.

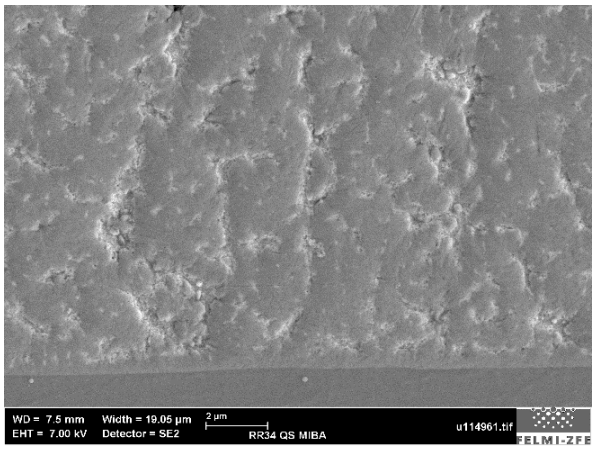

Figure 120 – CuPb23Sn3 (RR34). Topography of RR34 shown with SE detection and 15 keV acceleration potential.

6.2.9 CuPb23Sn3 (RR57)

The expected composition of layer RR57 is 3-4 wt% tin, 21-25 wt% lead and the rest copper. The AAS analysis yields 3.54 wt% Sn, 25.40 wt% Pb and 71.06 wt% Cu. The film deposition was started on a warm substrate. Thus, the temperature during the sputtering process reaches about 270°C. Thus, this deposition happens at about 20 °C higher temperatures compared to the other CuSnPb film productions. For the sputter process of the CuPbSn film a CuSn6 alloy, an elemental copper and an elemental lead target was used.

6.2.9.1 Investigation of the Untreated Surface

The first impression of the film of layer RR60 is very similar to the other CuPbSn layers (RR27, RR29, RR34). It appears relatively homogenous and the fine lines from the structure of the substrate are visible through the sputtered layer. To determine the average composition of the CuPbSn film, the area shown in Figure 121 was investigated and analyzed with SEM-EDS. The amount of lead determined with 15 and 7 keV is significantly higher than the results of the AAS analysis (Table 31). Geometry effects of Pb might be the reasons for the falsification of the results. As the following BSE-images show, the lead is very homogenously distributed within the film and therefore the AAS measurement should be plausible.

Table 31 – The average composition of the layer RR57 analyzed at 15 and 7 keV (Fig. 121).

	AAS	15 keV		7 keV	
Element	*[wt%]*	*[wt%]*	*[at%]*	*[wt%]*	*[at%]*
Sn L-line	3.54	3,93	2.77	3,35	2.50
Cu K-line	71.06	64,16	84.37	58,18	81.06
Pb M-line	25.40	31,91	12.87	38,47	16.44

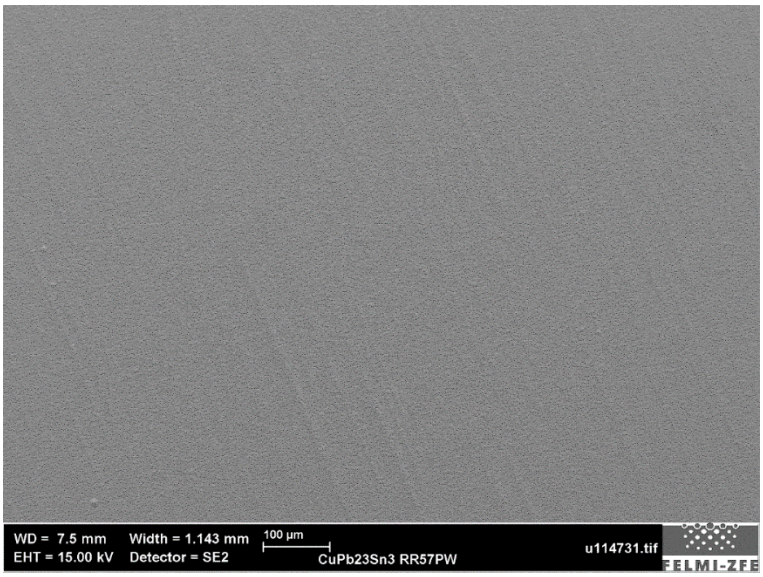

Figure 121 – CuPb23Sn3 (RR57). This image shows the homogenous structure of the CuPb23Sn3 film at an acceleration potential of 15 keV.

In Figure 122 a granular and homogenous morphology is shown. The darker and brighter areas in the HDAsB picture illustrate the two-phase structure of the alloy film (Fig. 123). In comparison to the CuPb23Sn3 layer of RR34 (Fig. 124), the film of RR57 consists of more brighter (Pb) and finely distributed areas. Moreover, the structure is less porous compared to the other CuPb23Sn3 films., probably due to the higher process temperatures of RR57.

In the Figure 126, it seems as if this CuPb23Sn3 layer only consists of two phases instead of three phases. A copper-rich phase, where a small amount of tin is dissolved, and an almost elemental lead phase is expected. Figure 126 illustrates that the Pb phase covers the copper-tin phase. This confirms again that lead might be present in elementary form in this film.

Moreover, the surface images indicate a columnar growth of the film, which is characteristic for the CuSn phase.

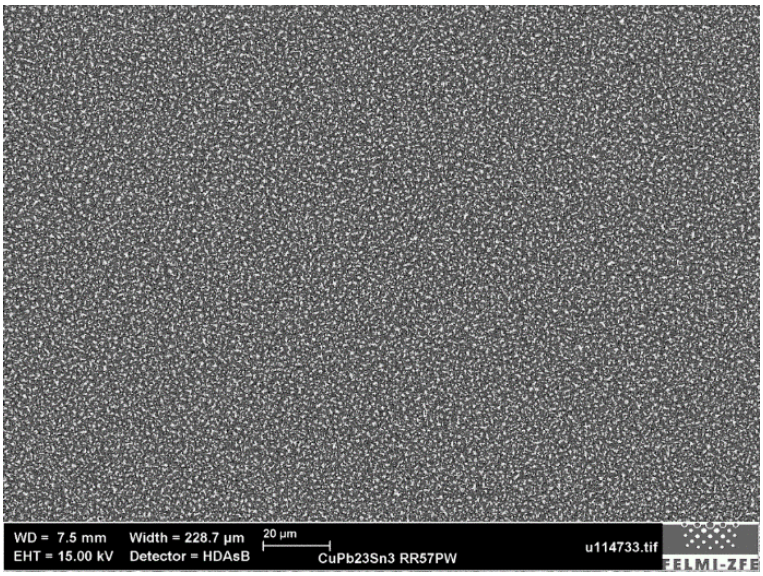

Figure 122 - CuPb23Sn3 (RR57). The HDAsB image illustrates the homogenous granular morphology of the film. Moreover, the multiphase structure is shown due to the different coloring in the picture.

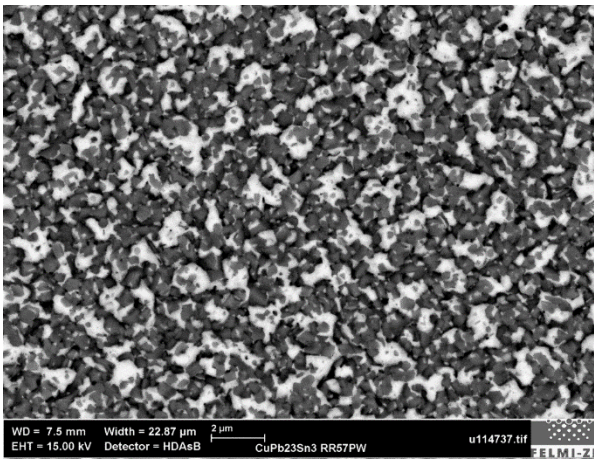

Figure 123 – CuPb23Sn3 (RR57). Two phases are visible in the HDAsB image. The bright areas are rich in lead and the darker areas are copper-rich-tin phases. This layer appears denser compared to the layer of RR34 on the right side due to little higher process temperatures.

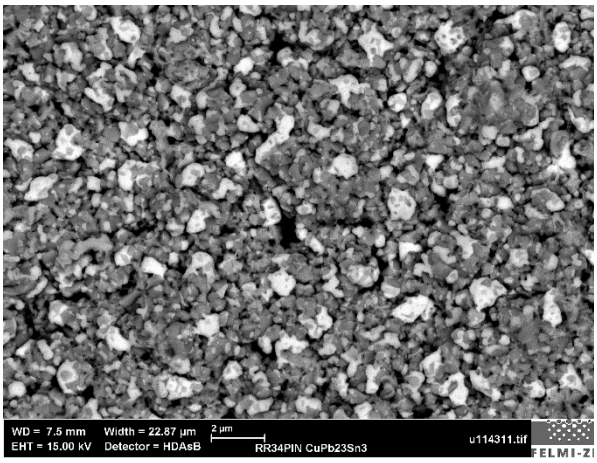

Figure 124 – CuPb23Sn3 (RR34). The brighter lead- rich areas are less homogeneously and finely distributed than in the left image of RR47 layer.

Higher magnifications (Fig. 125) show a voluminous structure, which resembles layer RR34. Hexagonal like (probably copper) and streak like structures (probably lead) are visible.

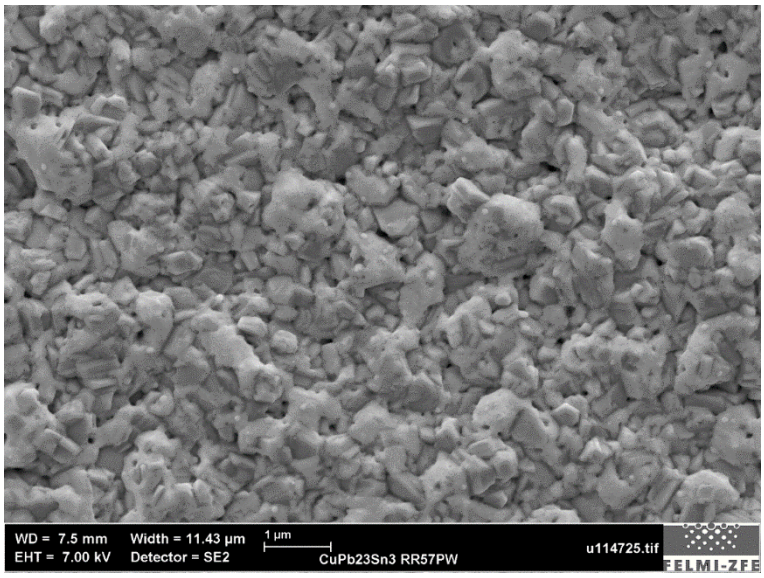

Figure 125 – CuPb23Sn3 (RR57). This SE image shows streak-like structures of lead possibly covering copper-rich areas recorded at 7 keV.

To show the two-phase structure of the CuPb23Sn3 film, a quantitative analysis of selected areas shown in Figure 126 was performed. Due to the assumption that elemental lead covers the copper-rich-tin phases, an analysis with 15 keV was not performed. The large interaction volume would falsify the result due to the information gained from regions below the relatively thin lead film. The quantitative analysis (Table 32) at 7 keV shows that almost elemental lead and copper-rich-tin phases are present in the film as expected. According to the Pb-Cu phase diagram, the two elements are not miscible at these process temperatures. The higher solubility of tin in copper can also be explained by the phase diagram of Cu-Sn (Chapter 4.4.2).

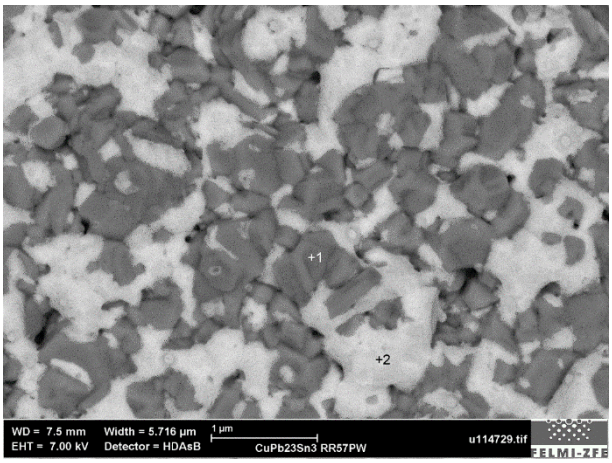

Figure 126 – CuPb23Sn3 (RR57). This image shows the selected areas for the quantitative analysis to exhibit the two phases on the film.

Table 32- -The results of the quantitative analysis of selected positions from Figure 126. The analysis was only performed at 7 keV, since the larger interaction volume at 15 keV would falsify the results even more due to the structure of the film.

	Position in image	
Element	*+1 [wt%]*	*+2 [wt%]*
Sn L-line	6.15	1.02
Cu K-line	91.65	1.88
Pb M-line	2.2	97.1

The EDS-spectra of the quantitative analysis show again that the lead phases are much more oxidized compared to the copper-rich phases due to the higher oxidation potential of Pb. Due to the multiphase system of the CuPb23Sn3 film, a quantitative analysis of the average composition with EDS is difficult. The overvaluation of lead in the quantitative analysis of the films is a problem. Massive geometry effects, the absorption of electrons and generation of florescence radiation falsify the results.

6.2.9.2 Investigation of the Polished Cross-Section

The polished cross-section of layer RR57 was prepared with Method 1 explained in Chapter 5.3.

The layer appears again very homogenous and flat due to an efficient polishing as shown in the SE image (Fig. 127).

The HDAsB image (Fig. 128) already shows the strong material contrast of the CuPbSn film.

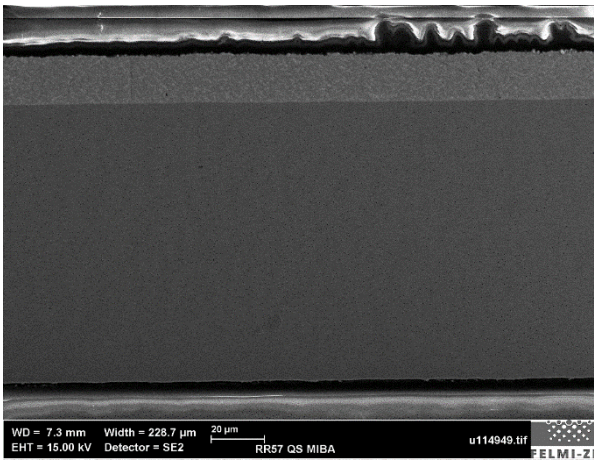

Figure 127 – CuPb23Sn3 (RR57). This image illustrates the flat polished cross-section of layer RR57.

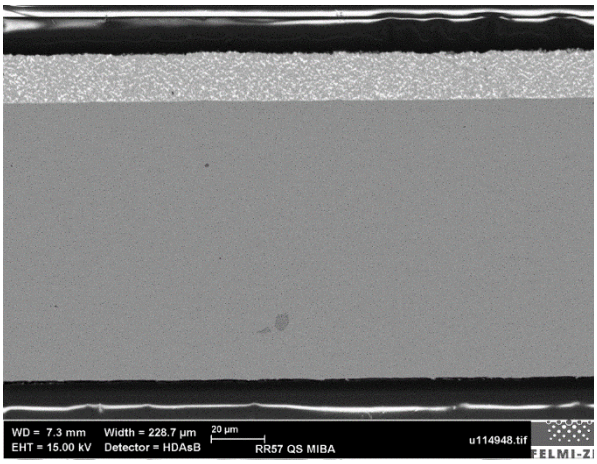

Figure 128 – CuPb23Sn3 (RR57). The polished cross-section appears as well very homogenous.

To determine the average composition of the CuPbSn layer, area 1 (Fig. 129) was scanned and analyzed at 15 and 7 keV (Table 33). The quantitative analysis at 15 keV of the polished cross-section resembles the AAS analysis. The results differ by a maximum of 1.70 wt%. The measurement at 7 keV deviates

more from the reference values as usual, since the geometry effects in surface near regions are stronger. These results show again that the geometry effects of rough surfaces massively influence the analysis.

Table 33 – The results of the quantitative analysis of a selected area in the CuPbSn film (Fig. 129) at 15 and 7 keV

	AAS	15 keV		7 keV	
Element	*[wt%]*	*[wt%]*	*[at%]*	*[wt%]*	*[at%]*
Sn L-line	3.54	4.11	2.69	4.61	2.86
Cu K-line	71.06	72.20	88.41	78.64	91.18
Pb M-line	25.4	23.69	8.90	16.75	5.96

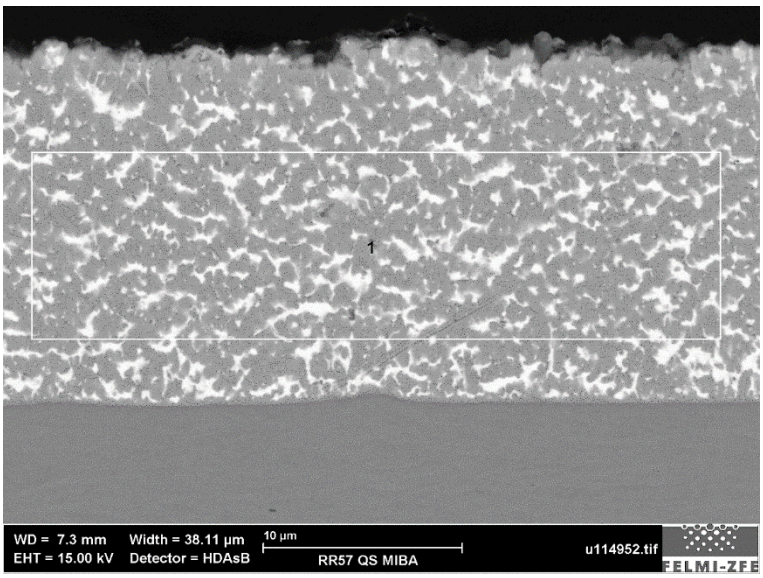

Figure 129 –. CuPb23Sn3 (RR57). This image shows the selected area for the determination of the average composition of the CuPb23Sn3 film (Table 33).

The polished cross-section in Figure 130 confirms the assumption that lead (bright areas) covers the copper-rich-tin phases (dark areas). The elemental lead grows like shells around the Cu-phases.

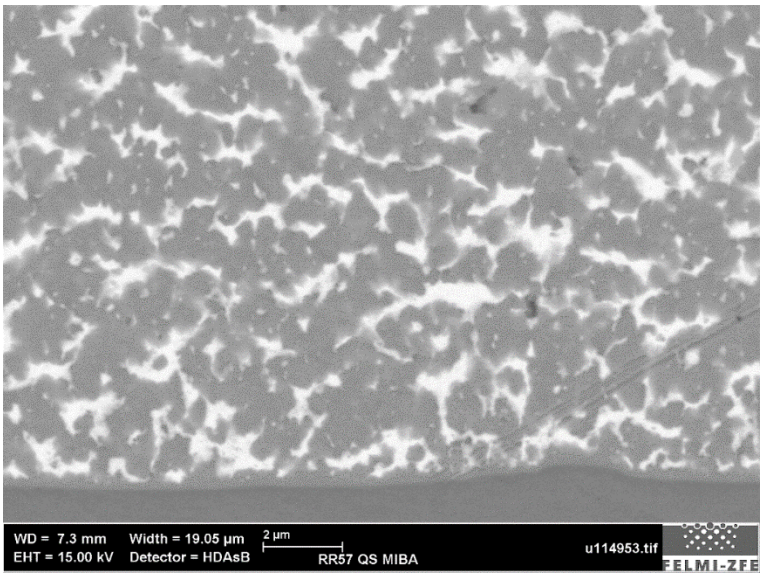

Figure 130 – CuPb23Sn3 (RR57). This image illustrates the thin streak-like elemental lead layers (bright areas) covering the copper-rich tin phases.

6.2.10 Comparison of "cold start" and "warm start" of CuPb23Sn3 layer

The deposition of layer RR29 was cold started. This means that the substrate deposition was started on a cold substrate (room temperature) and the temperature within the magnetron system reaches about 150°C. Sample RR34 and RR57 were started on a preheated substrate. The temperatures for the deposition of layer RR34 was between 200 and 250 °C during the sputter process, for RR57 the temperature was about 20 °C higher.

Figure 131- 133 clearly show that the layer deposited at lower temperature is more porous than the two films deposited at higher temperatures. Layer RR57 (Fig. 133) seems to be the most compact layer. In conclusion, the higher the temperature the denser the sputter coating. It seems as if the inhomogeneous nucleation is preferred at the cold substrate (Fig. 131) due to the higher temperature gradient.

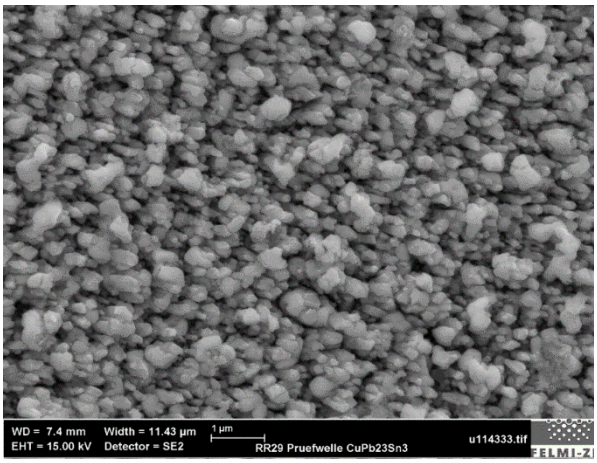

Figure 131 -CuPb23Sn3 (RR29). "Cold start". Depositions is carried out at about 150 °C.

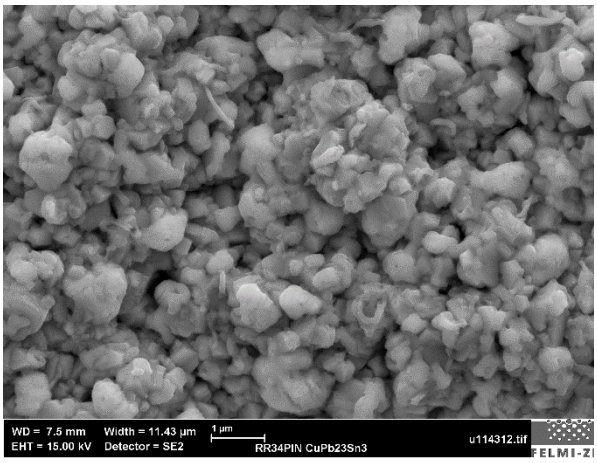

Figure 132 - CuPb23Sn3 (RR34). "Warm start". Depositions is carried out between 200 and 250°C.

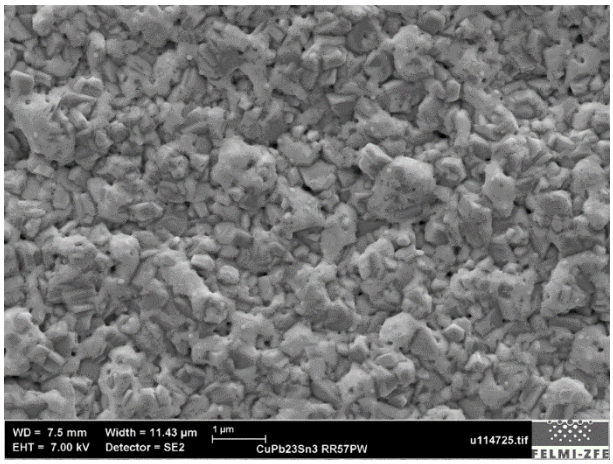

Figure 133 - CuPb23Sn3 (RR57). "Warm start". Deposition is carried out at little higher temperatures compared to RR34.

The HDAsB detection in Figure 134– 136 shows again the difference of density of the films due to different temperatures. Moreover, it illustrates that lead is more homogeneously and finely distributed at highest temperature in layer RR57 (Fig. 136).

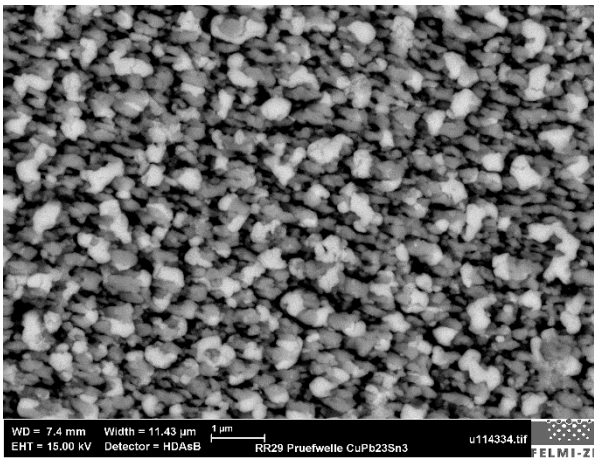

Figure 134 - CuPb23Sn3 (RR29). "Cold start". Depositions is carried out at about 150 °C.

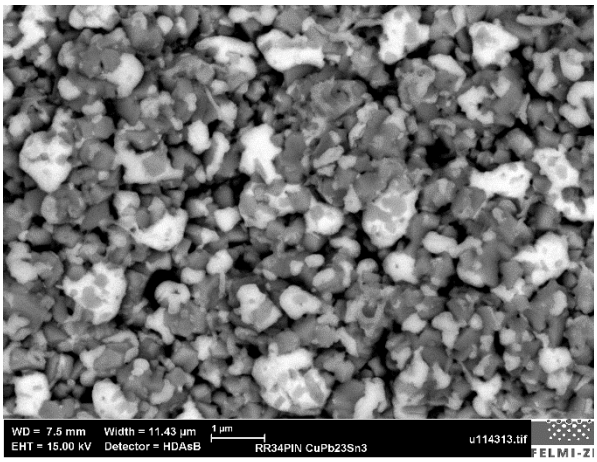

Figure 135 - CuPb23Sn3 (RR34). "Warm start". Depositions is carried out between 200 and 250°C.

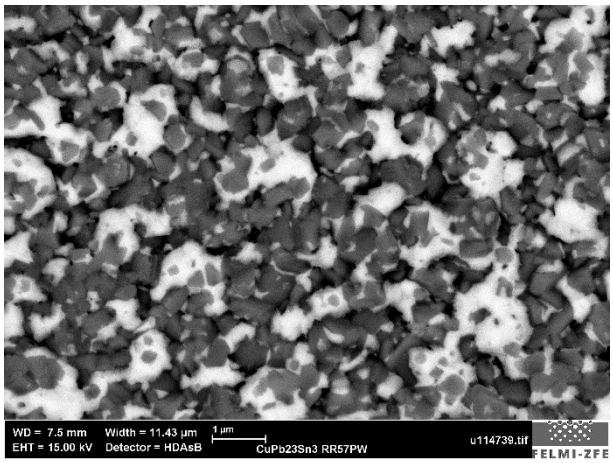

Figure 136 - CuPb23Sn3 (RR57). "Warm start". Deposition is carried out at little higher temperatures compared to RR34.

6.3 Investigation of the Multilayers System

For the investigation of the multilayers systems a polished cross-section of each layer system was produced. Therefore, RR43 and RR44 were prepared with Method 2 and HTC-877 with Method 1 explained in Chapter 5.6 and 5.7. To compare the two preparation methods, RR43 was also prepared with Method 1. For the determination of the average composition, the largest possible area of the single layers within the graduated layer system was scanned and analyzed with SEM-EDS. For the layer system HTC-877 line spectra at different positions within the multilayer system were recorded to show, if diffusion between the layers occurs and how long it takes the deposition process to reach an equilibrium state, where the desired composition is reached.

The multilayer structures are not discussed in detail, but some subregions are described in the following chapters.

6.3.1 RR43 (Preparation Method 1)

In Figure 137 the structure of the CuPb23Sn3 layer seems to be changed during the film growth. At the beginning the lead precipitations (bright) are finely and homogenously distributed. In the progressive layer growth, the lead precipitations get lager and less homogenously dispersed. It seems as if elemental liquid lead fills up the interspaces of the copper-rich-tin phases. Moreover, it seems as if tiny parts of the lead-rich phases are teared out and leave black dots behind. This could happen in any polishing step, since Pb is a very soft metal.

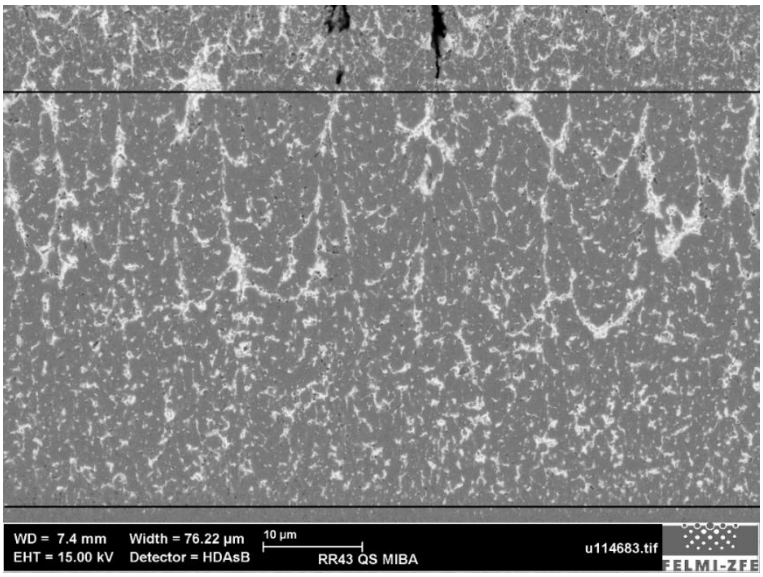

Figure 137 – RR43 (Method 1). The area between the two lines show the CuPb23Sn2 film in the multilayer system. The lead precipitations in the CuPb23Sn3 layer appears relatively homogenous and finely spread at the beginning of the layer. With increasing layer thickness the Pb phases get larger and more irregular distributed. Tiny black areas in lead-rich phases are visible.

The following image (Fig. 138) shows the characteristic columnar growth of the CuSn6 film. Moreover, the layer appears very homogenous, thus, an accurate analysis should be possible. However, silica residues of the polishing agent accumulate at the bottom of the CuSn6 layer.

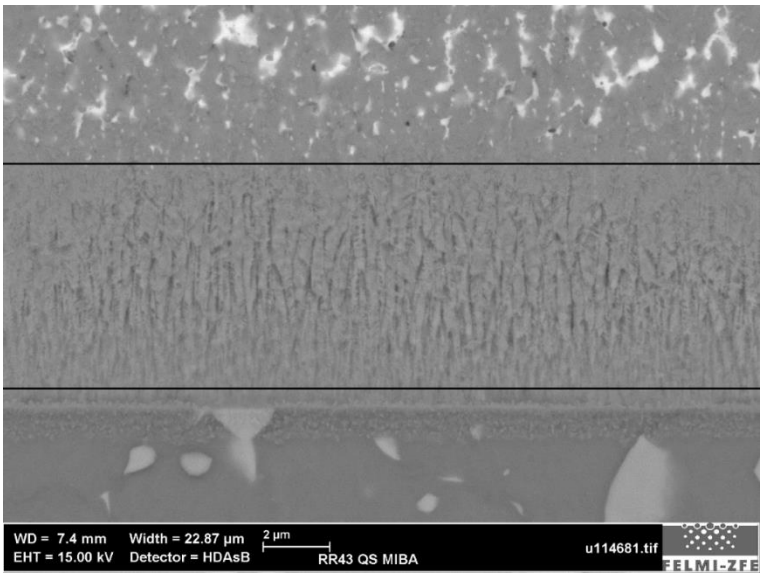

Figure 138 – RR43 (Method 1). The area between the two lines show the CuSn6 film in the multilayer system. The columnar growth of the CuSn6 layer is shown in this image. However, the structure appears amorphous (even crystalline) as well. Moreover, Si residues from polishing material accumulate at the bottom of the CuSn6 layer.

The CuPb27 film is very irregular und inhomogeneous as the following image (Fig. 139) shows. A quantitative analysis with EDS to determine the average composition of this layer is useless due to the large cracks across the whole film. The top layer appears as well very rough.

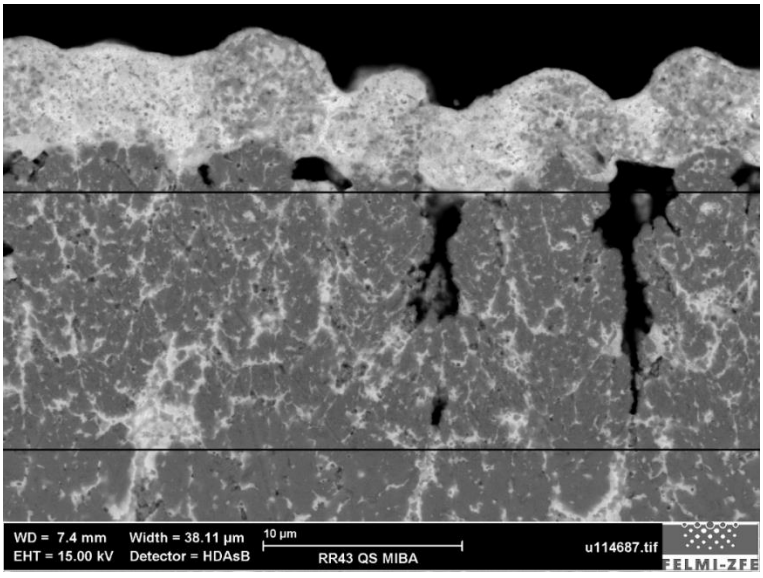

Figure 139 – RR43 (Method 1). This image illustrates enormous cracks in the CuPb27 layer.

For the determination of the average composition of each layer, large areas within the single films of the multilayer system were analyzed with EDS. Thereby, the interaction volume of the electron beam must be kept in mind to avoid information from the adjacent layers. Furthermore, the steel substrate was measured at 15 keV.

The amount of lead in the CuPb23Sn3 film is slightly undervalued, but the tin content is as expected.

In the CuPb27 layer the Pb content is 5 wt% higher as desired. This trend could be also seen in the single layer investigation of the CuPb27 film.

The CuSn6 film yields about 6 wt% tin as desired. The amount of tin at 7 keV is almost twice as high as those measured at 15 keV, possibly due the larger matrix effects in near-surface regions.
For the Cu9Pb layer, the amount of lead is again strongly undervalued. The undervaluation of lead, which is observed in most of the measurements (single layers and multilayers), is caused by the high absorption of electrons. The electrons remain in the film and, thus, the signal at the detector is distorted. The results of the measurements at 7 keV differ even more from the desired composition of the single layers in the graduated layer system.

Table 34 – This table shows the results of the determination of the average composition of each single layer within the multilayer system of RR43 (Method 1) at 15 and 7 keV. Additionally, the steel was quantitative analyzed.

Sample name	*Layer*	*Element*	*15 keV [wt%]*	*7 keV [wt%]*
RR43 (Method 1)	*Steel*	Si	0.77	-
		Mo	8.32	-
		V	1.06	
		Cr	3.99	-
		Mn	0.42	-
		Fe	76.58	-
		Co	8.85	-
	CuPb23Sn3	Cu	77.74	78.28
		Sn	3.77	4.95
		Pb	18.49	16.77
	CuPb27	Cu	67.00	80.86
		Pb	33.00	19.14
	CuSn6	Cu	89.95	78.56
		Sn	6.23	12.16
		Mo	2.52	9.28
		Fe	1.31	-
	Cu9Pb	Cu	15.68	42.41
		Pb	84.32	57.59

Moreover, a quantitative analysis of two selected positions in the CuPb23Sn3 and CuPb27 layer shown in Figure 140 and 141 were performed. The darker position +1 in the CuPb23Sn3 film is a copper-rich-tin phase, whereas the bright position +2 is rich in lead. The exact results are listed in Table 35 and 36. This confirms again the two-phase structure of the CuPbSn alloy shown in the measurements of the single layers of CuPb23Sn3 (Chapter 6.2.8 and 0).

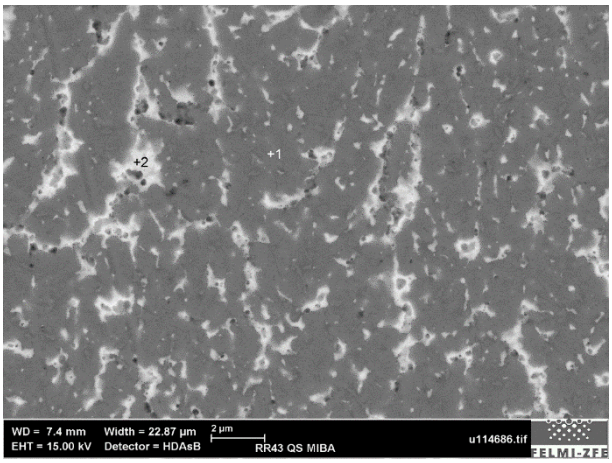

Figure 140 – RR43 (Method 1). This image illustrates the two selected position in the CuPb23Sn3 layer for the quantitative analysis.

Table 35 – It shows the results of the quantitative analysis of selected positions (Figure 140) in the CuPb23Sn3 layer to show the difference in composition.

	Position in image	
Element	*+1 [wt%]*	*+2 [wt%]*
Sn L-line	4.73	1.46
Cu K-line	89.15	26.79
Pb M-line	6.12	71.74

In the CuPb27 film, the darker position +1 contains almost 90 wt% of copper and the brighter position +2 almost 85 wt% lead as expected due to the investigations of the CuPb27 single layer (Chapter 6.2.4). The high degree of segregation of Cu and Pb can be confirmed again.

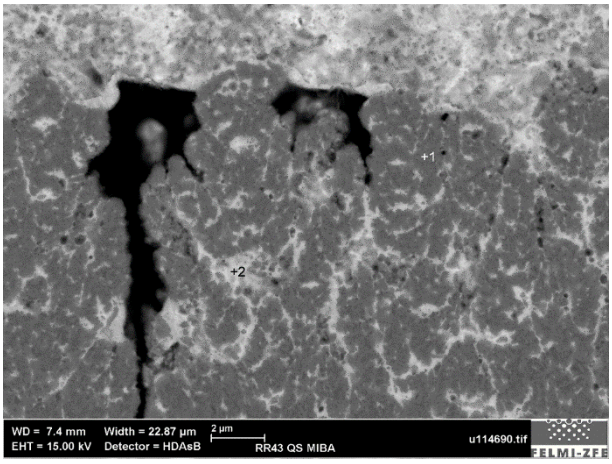

Figure 141 – RR43 (Method 1). This image shows the selected areas in the CuPb27 layer for the quantitative analysis.

Table 36 – The results of the quantitative analysis of two selected areas (Figure 141) in the CuPb27 film to show the compositional contrast.

	Position in image	
Element	*+1 [wt%]*	*+2 [wt%]*
Cu K-line	87.2	16.03
Pb M-line	12.8	83.97

The following images show the problems of the preparation Method 1. Silica residues accumulate between the layers as Figure 142 illustrates. Moreover, the ´black holes´ of the missing lead are visible again.

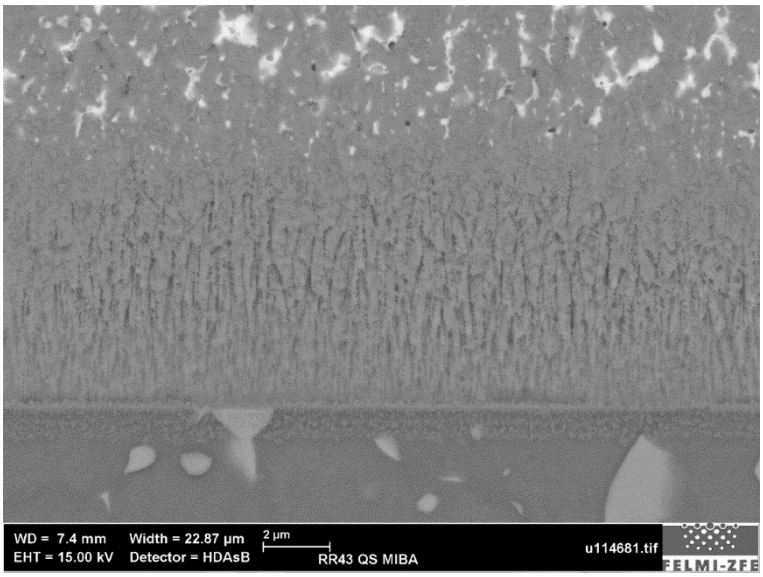

Figure 142 – RR43 (Method 1). The image clearly shows the silica residues between M42 steel substrate and CuSn6 layer.

The InLens image of RR43 (Fig. 143) shows that silica residues are finely spread over the whole polished cross-section. At the border areas silica occurs increased, since the polishing agents accumulate in the gaps between substrate and layers or embedding material.

The spherical lead precipitations in the Cu9Pb layer (Fig. 144), which were already illustrated in the single layer investigation of the Cu9Pb are not visible (Fig. 71). However, fine structures of residues of polishing agents (Si) are present.

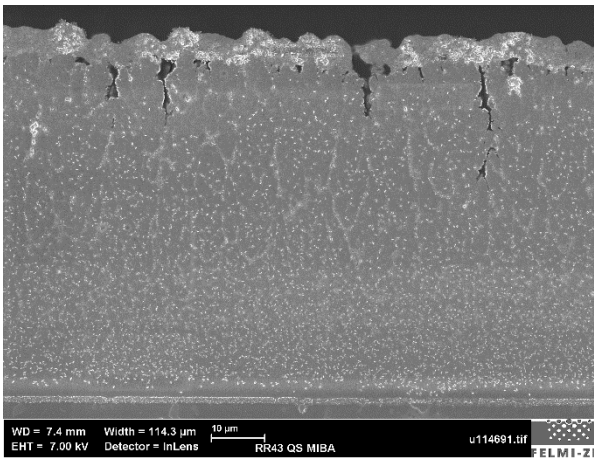

Figure 143 – RR43 (Method 1). This InLens-image exhibits the problem of preparation. Finely spread silica residues over the whole system are visible.

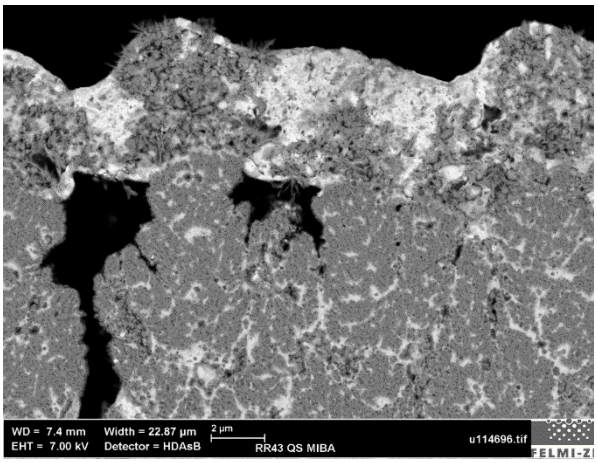

Figure 144 – RR43 (Method 1). This figure shows that residues of polish agents accumulate in cracks and at the surface of the polish. No spherical lead precipitations are visible in the Cu9Pb layer.

6.3.2 RR43 (Preparation Method 2)

The appearance of each layer of the graduated layer system resembles the analyzed single layers. For the quantification of each single layer in the multi-layers system as well large areas were selected for the SEM-EDS analysis.

The amount of lead in the CuPb23Sn3 layers determined at 15 keV is about 10 wt% lower than the desired value. At 7 keV the Pb content is only 7.58 wt% lower. The tin content deviates slightly from the desired composition. At 15 keV the amount of Sn is about 5 wt% and at 7 keV 6 wt%. However, the lead seems to be relatively finely and homogenously distributed within the layer.

In the CuPb27 layer the Pb content is as well strongly undervalued. In the HDAsB image the lead seems to agglomerate within the layer.

The evaluation of the CuSn6 layer at 15 keV deviates slightly from the desired composition. However, the measurement at 7 keV shows excellent results.

Only a relatively small area of the Cu9Pb film could be investigated due to the irregularity and roughness of this layer. The amount of lead in this layer is lower than desired. Moreover, the layer is strongly oxidized as expected due to the high amount of Pb. Smaller and larger spherical lead precipitations are present, which was already observed in the single Cu9Pb layer (Chapter 6.2.3).

A quantitative analysis of selected positions to show the differences in composition within the single layers was not performed.

Table 37 – This table shows the results of the quantitative analysis of each single layer within the multilayer system RR43 (Method 2) at 15 and 7 keV.

Sample name	Layer	*Element*	*15 keV [wt%]*	*7 keV [wt%]*
RR43 (Method 2)	*CuPb23Sn3*	Cu	82.32	86.22
		Sn	4.44	6.19
		Pb	13.23	7.58
	CuPb27	Cu	78.48	87.25
		Pb	21.52	12.75
	CuSn6	Cu	93.81	93.96
		Sn	4.99	6.04
	Cu9Pb	Cu	15.26	28.67
		Pb	84.74	71.33

Figure 145 clearly illustrates again, that at the beginning of the CuPb23Sn3 layer the lead precipitations are finer and more homogenously distributed within the layer. With progressive film growth the lead precipitations get larger. Finally, the layer resembles more and more the investigated single films of CuPb23Sn3.

Scratches appear across the whole multi-layer system. These arise possibly from molybdenum carbides, which are teared out of the steel substrate during polishing, or from hard residues from the polishing plates.

In Figure 146 recorded at 7 keV the spherical lead precipitations in the Cu9Pb layer are clearly visible compared to the preparation Method 1 (compare Fig. 149 and 150). There, these characteristic structures are possibly smeared or pulled out during polishing.

The fine oblong structures are silica residues from polishing agent OPS non-dry. Since the Cu9Pb layer is very soft, the preparation is very challenging. Some parts of the film are strongly maltreated, therefore, a quantitative analysis with SEM-EDS is difficult. This method requires a flat and clean surface to deliver a trustful result. Impurities from the different polishing steps, which falsify the results, accumulate in unevenness and holes within the layer, thus, a regular deposition is also required to gain results with high accuracy.

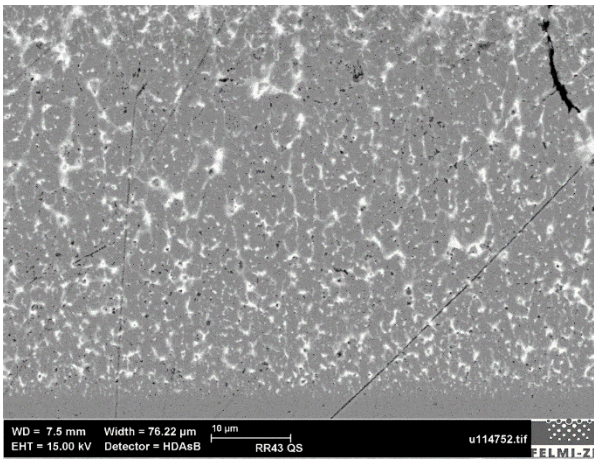

Figure 145 – RR43 (Method 2). This image shows the CuPb23Sn3 layer of RR43 (Method 2). The microstructure of the film changes within the film. Moreover, scratches from the polishing process are illustrated.

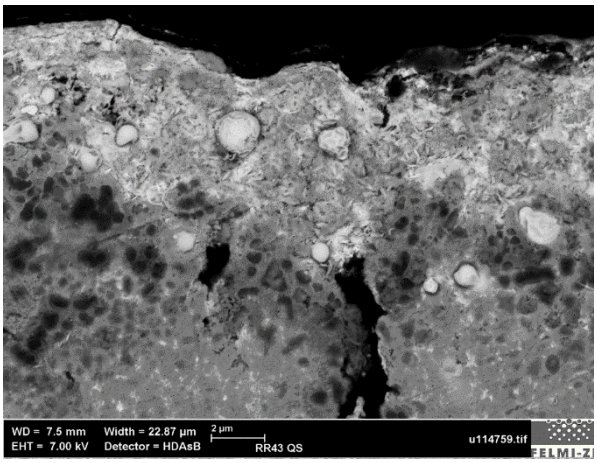

Figure 146 – RR43 (Method 2). This figure shows spherical lead precipitations in the layer Cu9Pb. These are uncovered in the polishing steps. However, also Si residue (fine long structures) are present.

6.3.2.1 Comparison of Preparation Method 1 and 2 with multi- layer system RR43

The following images show the differences of the two different preparation methods (Chapter 5.6 and 5.7). The InLens detection image of layer system RR43 (Method 2) shows that more silica residues (finely spread bright areas) remain on the polished cross-section with polishing Method 1.

The spherical lead precipitations are visible with preparation Method 2, whereas these structures are probably smeared with Method 1. However, on the polished cross-section of preparation Method 1 less scratches are present.

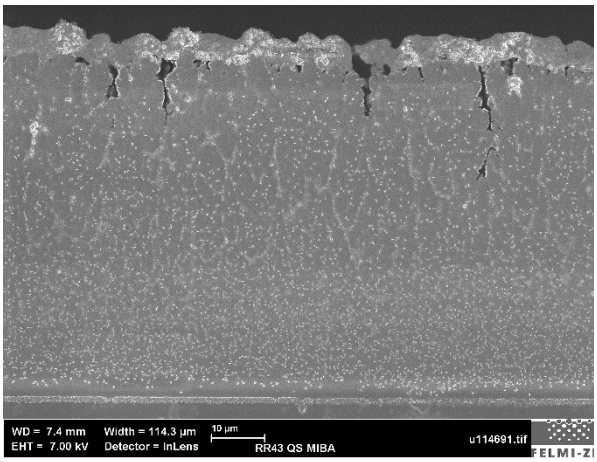

Figure 147 – RR43 (Method 1). The polish prepared with Method 1 shows finely distributed Si residues.

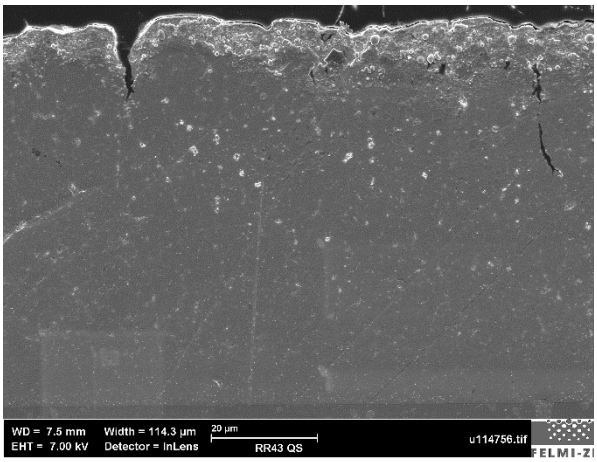

Figure 148 – RR43 (Method 2). The polish prepared with Method 2 show barely residues from polishing.

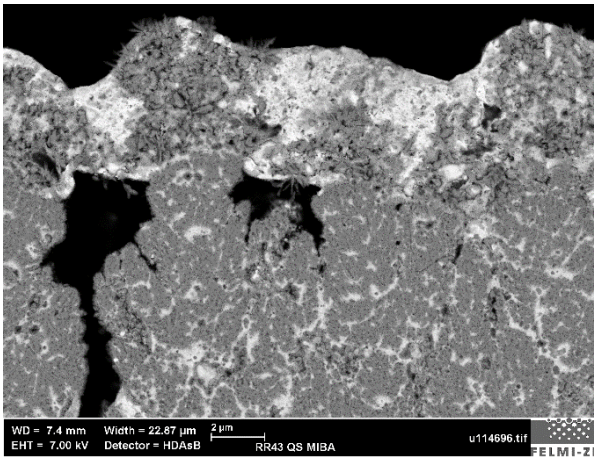

Figure 149 – RR43 (Method 1). This image shows the impurities at the CuPb27 and Cu9Pb layer from polishing Method 1

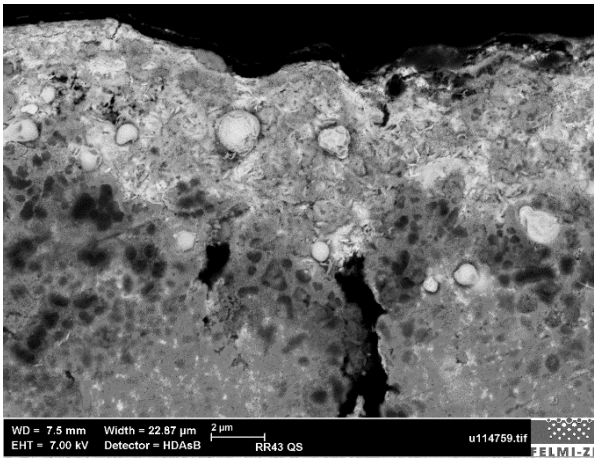

Figure 150 - RR43 (Method 2). This image shows the impurities at the CuPb27 and the spherical lead precipitations Cu9Pb layer from polishing Method 2

6.3.3 RR44 (Preparation Method 2)

In general, the layer system RR44 (Method 2) appears less rough and more homogenous than RR43.

For the determination of the average composition, large areas of each layer in the graduated layer system were scanned and analyzed. The results are listed in the following Table 38.

The composition of the CuPb23Sn3 film is very similar to those of layer system RR43 (Method 1). The lead content is strongly undervalued, but the amount of tin corresponds to the desired value.

For both CuPb (Cu9Pb and CuPb27) layers, the amount of lead is significantly lower as desired. If measurement errors are the reason for those deviations or lead removal during the preparation method is difficult to determine. Single layers of each film should be produced as reference during the deposition of the multi-layer system. Through the analysis of the single layers the accuracy of the measurement can be estimated. However, the CuSn6 layer almost corresponds to the desired composition at an acceleration potential of 15 keV.

Table 38 – This table shows the quantitative analysis of layer system RR44 (Method 2) of each film within the graduated layer system at 15 keV.

Sample name	Layer	*Element*	*15 keV [wt%]*
RR44 (Method 2)	*CuPb23Sn3*	Cu	78.41
		Sn	3.96
		Pb	17.62
	CuPb27	Cu	86.25
		Pb	13.75
	Cu9Pb	Cu	19.46
		Pb	80.54
	CuSn6	Cu	93.56
		Sn	5.19

The CuSn6 layer of the following image (Fig. 151) appears very homogenous and the characteristic columnar growth is not shown as in layer system RR43. Probably the columnar growth of RR44 is finer and appears at larger magnifications. The few bright precipitations might originate from the CuPbSn or CuPb layers by smearing the film during polishing or cracks in the CuSn6 layer are filled with lead phases from adjacent film.

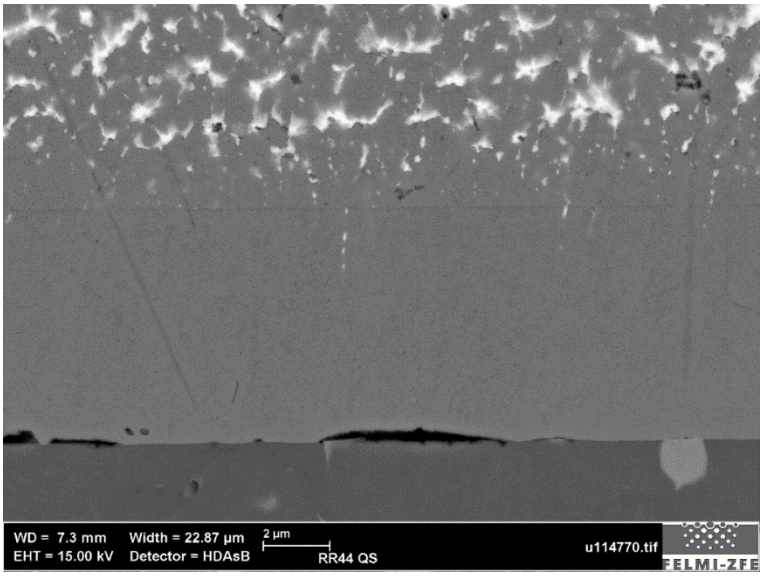

Figure 151 – RR44 (Method 2) In this picture the homogenous CuSn6 layer is shown. Moreover, black structures (rich in oxygen) on the steel substrate, which could lead to adhesion problems, are present.

The microstructure of the CuPb23Sn3 layer (Fig. 152) is similar to those of RR43 (Fig. 145). However, the film is even more homogenous, and the lead precipitations evenly distributed. The Pb phases are finer spread at the beginning of the layer and grow up to larger branches with increasing layer thickness.

That could be a hint that the equilibrium of the desired composition is set after a certain time of deposition. This trend is also shown for layer system RR43.

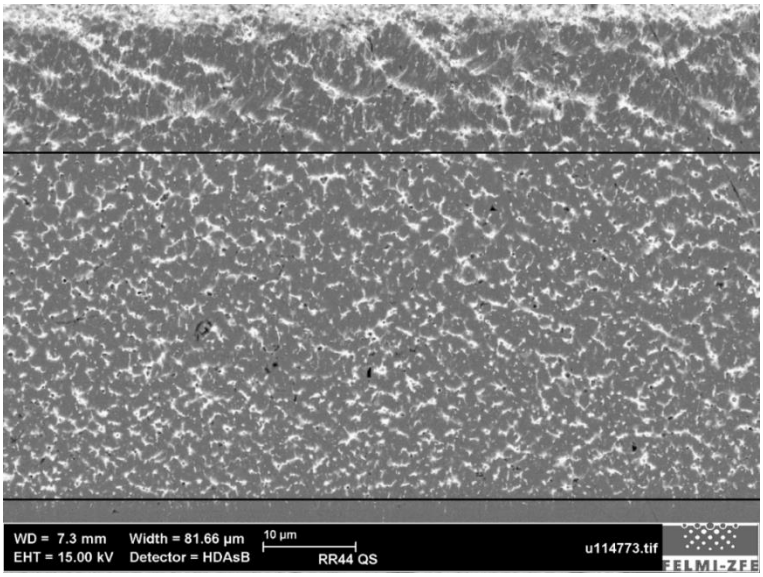

Figure 152 – RR44 (Method 2.) This image exhibits the homogenous microstructure of the CuPb23Sn3 film of layer system RR44 (Method 2).

The tin free CuPb27 phase appears totally different to the CuPb23Sn3 layer. The lead-rich phases (bright) are relatively arbitrarily distributed. The Cu9Pb layer appears smooth and homogenous and the characteristic spherical lead precipitations are visible again.

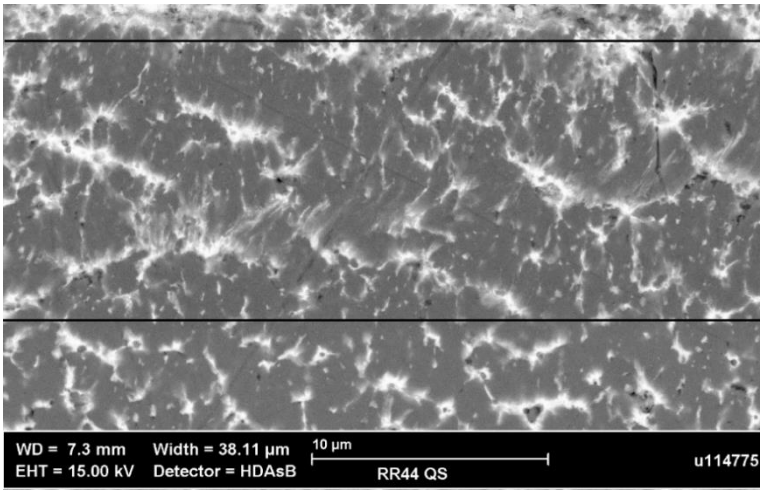

Figure 153 – RR44 (Method 2) In this image the CuPb27 and the Cu9Pb of layer system RR44 (Method 2) are illustrated. Spherical lead precipitations are present in the Cu9Pb layer.

The preparation Method 2 is relatively satisfying. Polishing residues are not present, but some smearings and scratches are visible.

6.3.4 HTC-877 (Preparation Method 1)

The multi-layer system of the layer system HTC-877 was produced under optimized sputtering conditions (190-250 °C). It appears homogenous and smooth. The two-component embedding material Multifast and Durofast, Struers was used instead of Epofix, Struers. The grained structure of the embedding agent leads to deformation of the Cu9Pb film, since the harder grains are pushed into softer layers. The polishing was performed with Method 1.

The quantitative analysis of each single layer of the graduated layer system was performed at 15 keV and the results are shown in the following Table 39.

The lead content in the CuPb23Sn3 film is again strongly undervalued compared to the desired value but very similar to the measured composition of the multi-layer systems RR43 and RR44.

The measured amount of Pb in the CuPb27 layer is about 35 wt% and, therefore, higher than desired. However, the analysis of the Cu9Pb layer corresponds to the desired composition.

The results of the CuSn6 layer correspond to the desired composition like most of the time. The Si residues (0.71 wt%) came from the polishing agents, which accumulate between the harder and softer layers or on the surface of the polished cross-section.

Table 39 – The results of the quantitative analysis of each single layer within the multilayer system of sample HTC-877.

Sample name	*Layer*	*Element*	*15 keV [wt%]*
HTC-877 (Method 1)	*CuPb23Sn3*	Cu	76.86
		Sn	4.15
		Pb	18.98
	CuPb27	Cu	65.27
		Pb	34.73
	CuSn6	Cu	93.00
		Sn	5.09
		Fe	1.20
		Si	0.71
	Cu9Pb	Cu	8.89
		Pb	91.11

In Figure 154 the transition area of two adjacent layers appears smeared. Fine lead streaks from one layer reach into the other layer. Possibly it is an unwanted side effect of the polishing procedure or the interspaces of the columnar structure of the CuSn6 layer partially filled up with lead precipitations.

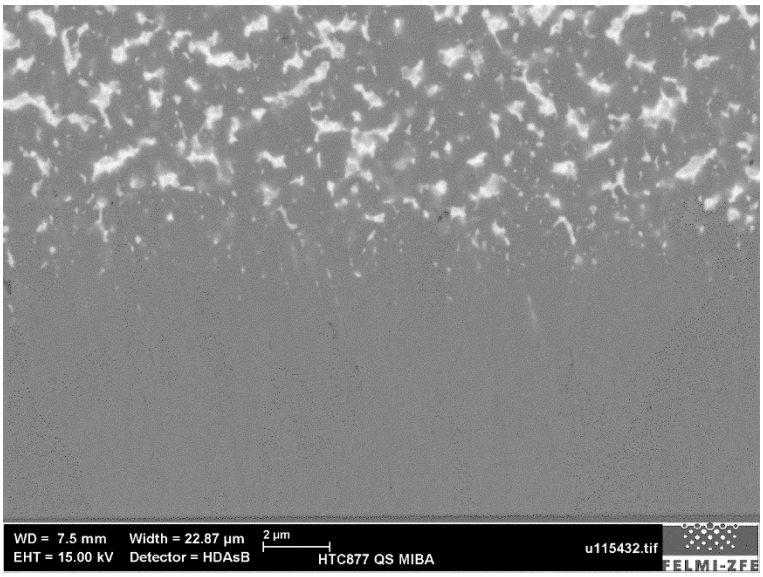

Figure 154 – HTC-877 (Method 1). It shows the smearing of lead due to polishing.

In the CuPb23Sn3 layer lead-rich and lead-poor phases were detected on the HDAsB images recorded with SEM and investigated more closely with EDS analysis. At higher magnification it seems as if lead partially was removed from the layer (Fig. 155) and small holes (black in HDAsB image) are formed. Possibly hard components of the polishing plates or agents tear out the soft lead precipitations. This could be the reason for the low amount of lead in the CuPb23Sn3 layer (Table 40). The smearing of the lead while polishing also influences the results of the EDS analysis.

The quantitative analysis of the areas shown in Figure 155 and 156 confirms the assumption of lead-rich and lead-poor phase in the layer.

Table 40 – This table illustrates the quantitative analysis of lead-rich and lead-poor areas in the CuPb27Sn3 layer of HTC.877 (Method 2) (Fig. 155 and 156)

Area in CuPb23Sn3	*Element*	*[wt%]*	*Area in CuPb23Sn3*	*Element*	*[wt%]*
*Lead-poor area (*Fig. *155)*	Pb	11.41	*Lead-rich area (*Fig. *156)*	Pb	20.67
	Sn	4.45		Sn	3.94
	Cu	84.14		Cu	75.40

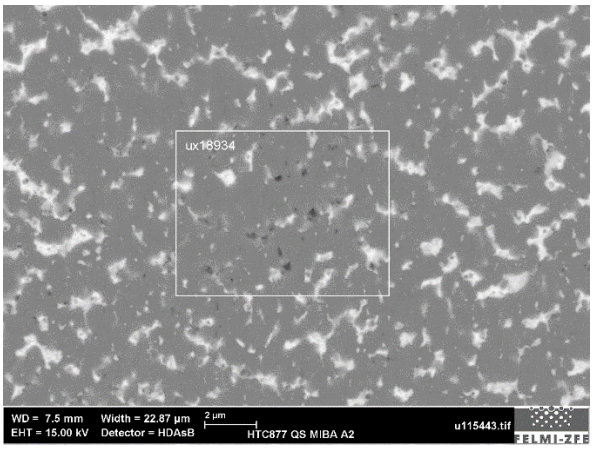

Figure 155 – HTC-877 (Method 1). This image shows the lead-poor area. Parts of Pb are teared out of the film in the polishing steps.

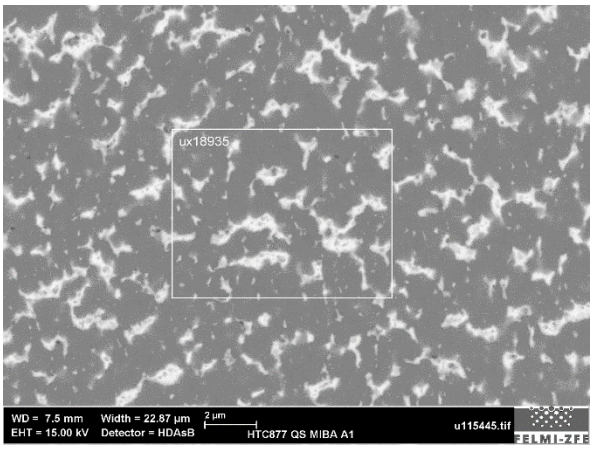

Figure 156 – HTC-877 (Method 1). This image shows the lead-rich area

These break outs are also visible in the CuPb27 layer and lead to the change of composition.

6.3.4.1 Line Spectra between CuSn6 and CuPb23Sn3

The line spectra were recorded to investigate if a graduated transition between the layer CuSn6 and CuPb23Sn3 occurs. Therefore, horizontal line scans at selected positions shown in Figure 158 and 160 were performed. The lines with a length of 20 µm were placed 3 µm, 6µm, 7 µm, 8 µm, 9 µm 10 µm and 15 µm above the beginning of the CuSn6 film. The measurements were carried out at 15 keV and illustrated in Figure 157.

The quantitative analysis of the lines at position 3 µm and 6 µm shows very constant results of the desired composition CuSn6. At the position of 6 µm the curve of Cu slightly starts to decrease, whereas the Pb content slightly increases until both curves reach a value of about 50 wt%. The Sn curve begins to decrease at about 8 µm until it reaches the desired value of about 3 wt%. This confirms the previous investigations, that the CuPb23Sn3 film consists of two phases. In the range of about 6 to 10 µm the lead content increases and the copper content decreases. Since the sputtered layers consist of two phases and are very complex, it is not possible to determine the equilibrium state. The composition varies from position to position, which was already shown in previous studies and is again confirmed in the recording of line spectra.

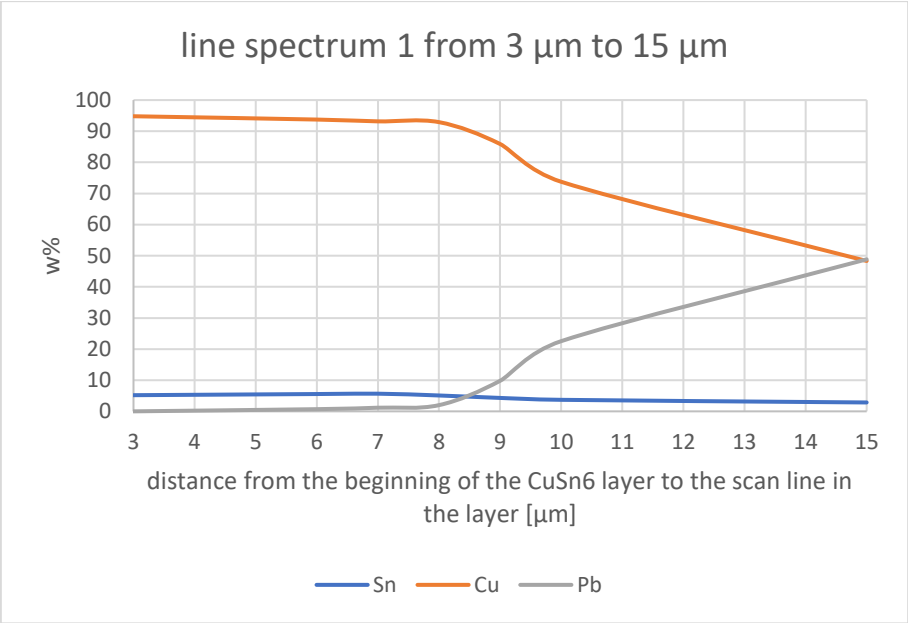

Figure 157 – HTC-877 (Method 1). This diagram exhibits the measurement results of quantification with EDS of HTC-877 (Method 2) at different positions. It shows how the concentrations of Sn, Cu and Pb changes along a horizontal line with 20 µm (Fig. 158). Measurements were carried out at 15 keV.

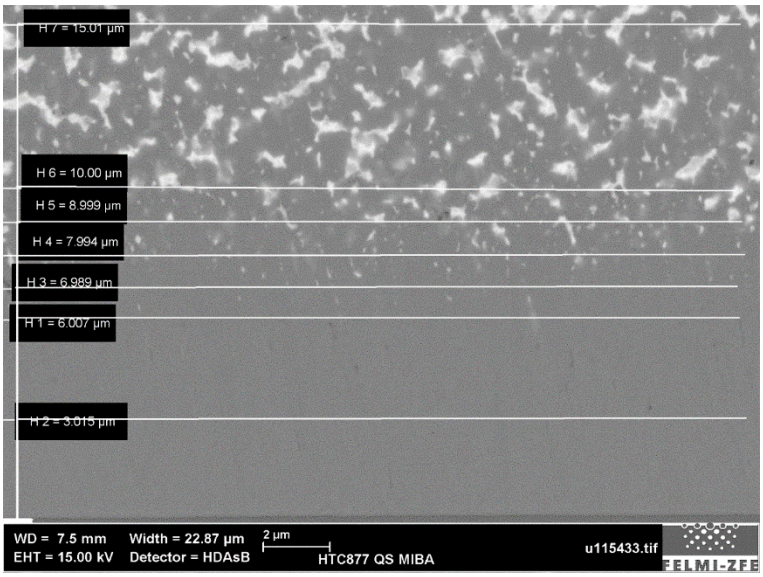

Figure 158 – HTC-877 (Method 1). This picture illustrates the positions of the lines, which were quantitative analyzed for the line spectra.

A second line spectra was recorded with 15 keV at a totally different position of the multi-layer system. The length of the lines was 20 µm.

This diagram in Figure 159 shows that the curve of tin is almost identical to those shown above in Figure 157. Also the curve progression of copper and lead resembles the first line spectra and confirms that the lead content increases, and the copper content decreases between 6 and 10 µm from the top edge of the steel substrate. It also clearly illustrates that the amount of Cu and Pb within the CuPb23Sn3 varies along the line. The line at 15 µm with a length of 20 µm has the approximately desired composition of the CuPb23Sn3 film in layer system HTC-877.

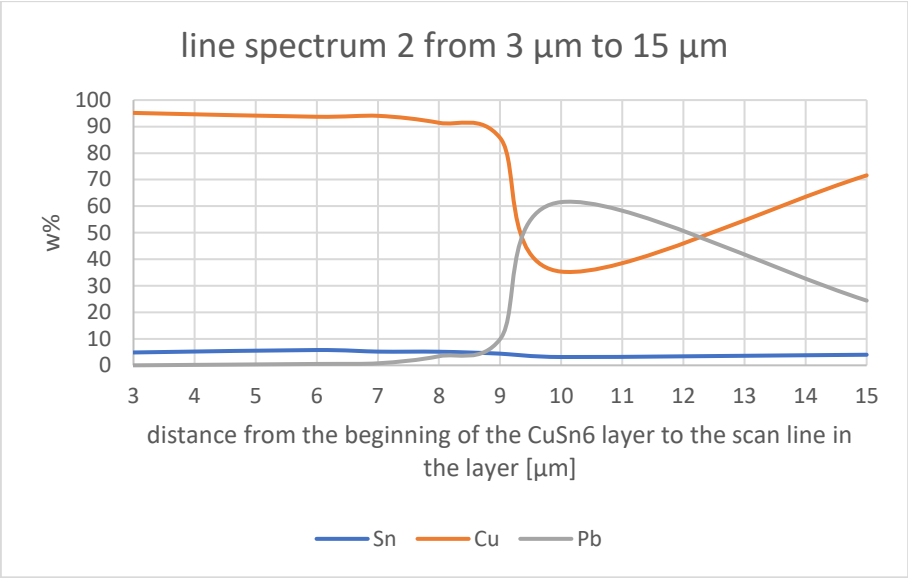

Figure 159 - HTC-877 (Method 1). This diagram exhibits the measurement results of quantification with EDS at different positions. It shows how the concentrations changes along a horizontal line with 20 µm at a totally different position of the multi-layer system. Measurement was performed at 15 keV.

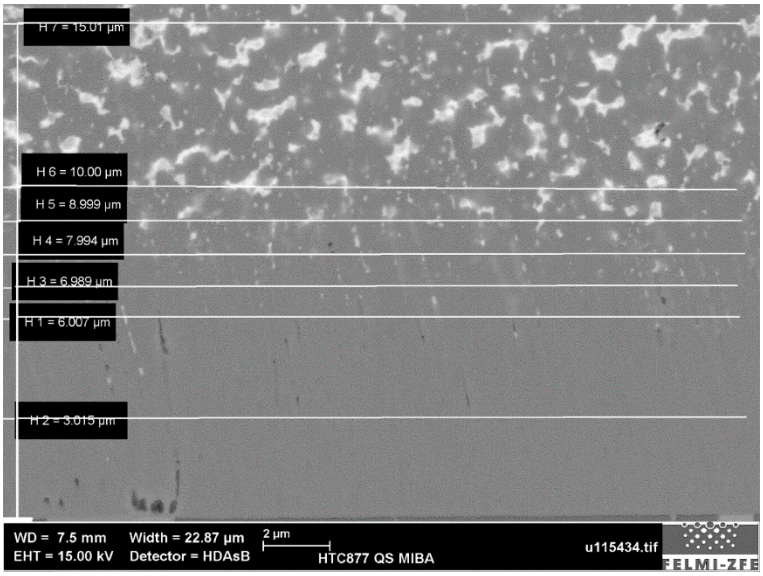

Figure 160 – HTC-877 (Method 1). This picture illustrates the positions of the lines, which were quantitative analyzed for the line spectra.

Further line spectra of 3 lines placed in the CuPb23Sn3 layer at the position of 10 µm, 20 µm, 30 µm and 40 µm above the beginning of the CuSn6 film was recorded at 15 keV (Fig. 162). This time the scanned lines are 70 µm long instead of 20 µm. Moreover, the areas between the lines were scanned and quantitative analyzed.

The following diagram (Fig. 161) shows that the average composition of the layer varies less than compared to the spectra of Figure 157 and 159 due to the larger area of investigation. The amount of tin remains relatively constant as usually. Nevertheless, the copper and lead content vary more or less from line to line. If the amount of Cu decreases, the amount of Pb increases. This again confirms that the complex structure of the film and the insolubility of copper and lead at this process conditions.

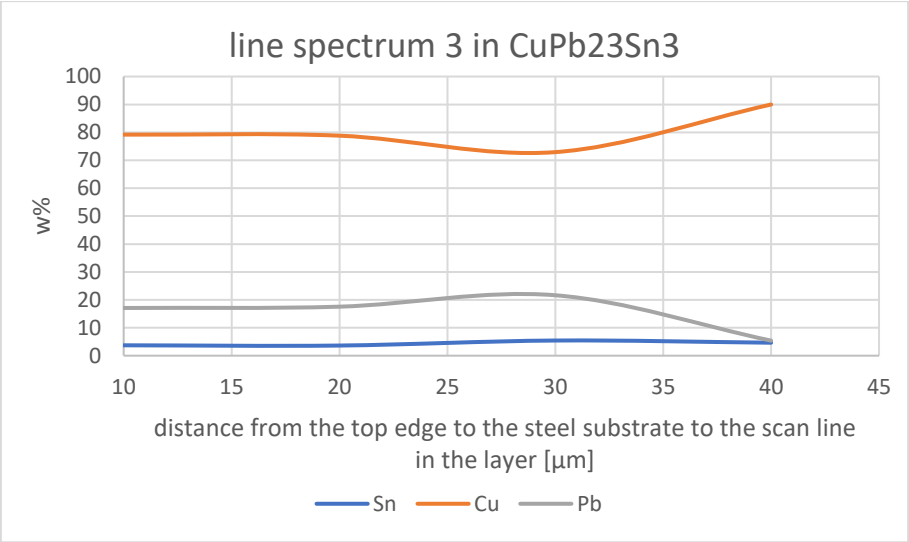

Figure 161 – HTC-877 (Method 1). This diagram illustrates the line spectra within the CuPb23Sn3 layer of HTC-877.

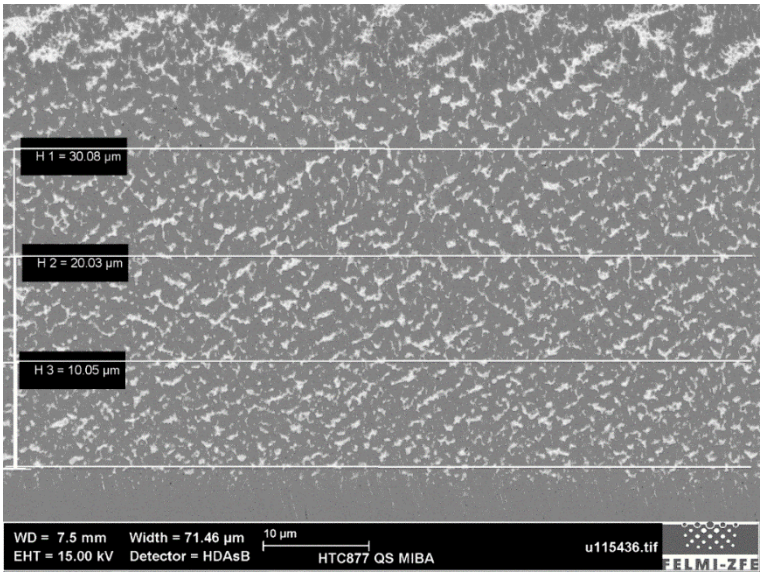

Figure 162 – HTC-877 (Method 1.) The selected positions of the quantitative analysis for the line spectra of the CuPb23Sn3 layer.

The following table (Table 41) exhibits the results of the quantitative analysis of the areas between the lines shown Figure 162. The amount of tin in these three measured areas varies only slightly. The average composition of the area between 10 µm and 20 µm corresponds with the desired composition. The other two analyzed regions resemble each other but the amount of Pb is strongly undervalued.

Table 41 – The results of the determination of the average composition of the areas between the lines shown in Figure 162.

Position	*Area between line x and line y*	*Sn [wt%]*	*Cu [wt%]*	*Pb [wt%]*
1	10 µm and 20 µm	4.03	72.29	23.68
2	20 µm and 30 µm	4.28	79.16	16.56
3	30 µm and 40 µm	4.42	79.91	15.67

This detailed investigations of the CuPb23Sn3 layer illustrate again that the determination of the average composition is very difficult due to the complex and partially inhomogeneous structure of the film and the immiscibility of copper and lead at this process conditions.

7 Conclusion

A characterization method for *metallic single (CuPb23Sn3, Cu9Pb, CuSn6 and CuPb27) and multilayer structures* was developed. With *scanning electron microscopy* in combination with *energy dispersive spectroscopy* the single layer systems and the multilayer (graduated) layer system were investigated. On the one hand, the untreated surface of the single alloy layers was investigated. It shows that the strong absorption of electrons of the heavy metal lead (matrix effects) and the partially extremely rough surfaces of the films lead to problems in quantification of Pb.

On the other hand, the single layers were studied in polished cross-section. Therefore, two different polishing methods and a broad-ion-beam-cut method were used to compare the results of various preparation techniques. It shows that both polishing methods leave scratches and smear the soft Pb across the whole samples and, therefore, artifacts in appearance of the films and concentration of elements probably occur. However, the broad-ion-beam method uncovers the real structure of the film and avoids smearing of soft components but re-depositions after the BIB-cut cannot be completely excluded. In general, the quantitative analysis with SEM-EDS of the single layers in polished cross-section deviates less from the AAS reference values than the analysis of the untreated surface due to reduced geometry influences (roughness of untreated surface). Even the preparation with BIB-cut, which avoids smearing, shows at the CuPb25 film deviations in the average composition from the AAS results. At this point it might be useful to recall the principle that a chemical analysis is the attempt to get a value that is as near as possible at the true value, which will always remain unknown. The very inhomogeneous distribution of lead within the film may lead to inaccuracies of the EDS measurements and possibly also of the AAS analysis. Moreover, the portion of lead can still pose problems due to undesired absorption of electrons, which can be only solved by the optimization of the EDS system based on suitable reference values.

The multilayer structures were investigated in polished cross-section prepared by two different polishing methods. Specified areas within the single layers of the graduated layer system were selected and scanned. The results of each area within a layer in the multilayer system are similar to those of investigated single film. Pb is mostly undervalued due to matrix effects of lead, but the quantification of the CuSn6 layer corresponds well to those of the AAS analysis and the expected composition. The explanation of these phenomenon is, that tin is soluble in copper, but lead and copper are not miscible at the applied sputter conditions.

The line spectra recorded at certain distances between CuSn6 and CuPb23Sn3 illustrate that the equilibrium concentration of the CuPb23Sn3 film is only achieved after a few nm (4 nm from the end of the previous CuSn6 film). This must be also considered for the quantitative analysis of the single layers within the multilayer system. This examination also supports the assumption that diffusion is negligible in the multilayer system.

All in all, the experiments show that the investigation of polished cross-sections with SEM-EDS is appropriate for the characterization and quantification of the single and multilayer structures. The

investigation of the untreated surface just gives a rough estimation of the composition. However, it is necessary to improve the polishing process to get flat surfaces without artifacts like smearing or pull-out. Moreover, trustful reference values for the composition of the single layers should enable the development of individual correction modes of the EDS system like k-factor optimization in order to reduce the systematic error of the determination of the lead concentration due to matrix effects. Therefore, probably further quantitative investigation methods like ICP-MS and XRD measurements are necessary. With these improvements an economic and accurate serial monitoring to ensure a high quality of such multilayer systems is possible.

8 References

[1] Handbook of Physical Vapor deposition (PVD) Processing, Donald M. Mattox, *second edition*, Elsevier **2010**, p. 1-164.

[2] Kelly, P.J., Arnell R.D., Magnetron sputtering: a review of recent developments and applications, *Vacuum*, 56 **(2000)** 160-161.

[3] Handbook of Sputter Deposition Technology, Fundamentals and Applications for Functional Thin Films, Nanomaterials, and MEMS, Kiyotaka Wasa, Isaku Kanno, Hidetoshi Kotera, *second edition*, Elsevier **2012**, p. 106.

[4] Handbook of Thin Film Process Technology, Glocker D., Shah S., first edition, CRC Press **1995**.

[5] Suryanarayanan R., The co-evaporation technique-a potential tool for basic and applied research, *Thin film solids, 50* **(1978)** 349- 350.

[6] Sputtering by particle bombardment II, Sputtering of Alloys and Compounds, Electron and Neutron Sputtering, Surface Topography, Behrish R., *first edition*, Springer- Verlag Berlin Heidelberg **1983**, p.1-18.

[7] The Foundations of Vacuum Coating Technology, Mattox Donald M., *first edition*, Springer-Verlag Berlin Heidelberg **2003**, p.34-36.

[8] Multilayer PVD coatings for wear protection, Holleck H. and Schier V., *Surface and Coatings Technology*, 76-77 **(1995)** 329-330.

[9] Scanning electron microscopy and x-ray microanalysis, Goldstein J, Newbury D., Joy D., Lyman C., Echlin P., Lifshin E., Sawyer L. and Michael J., *third edition*, Springer- Verlag Berlin Heidelberg **2007**, p.1-553.

[10] Scanning electron microscopy, Physics of image formation and microanalysis, Reimer L., *second edition*, Springer- Verlag Berlin Heidelberg **1998**, p.3-15.

[11] Carl Zeiss Microscopy GmbH, [cited: August 13,2018], https://www.zeiss.de/mikroskopie/produkte/rasterelektronenmikroskope/geminisem.html#gemini-und-seine-neuheiten.

[12] Carl Zeiss Microscopy GmbH, [cited: November 22, 2018], http://www.tssmicroscopy.com/wp-content/uploads/2017/06/ULTRA_Brochure.pdf.

[13] Scanning electron microscopy and x-ray microanalysis, Goldstein J.I., Newbury D.E., Michael J.R., Ritchie N.W.M., Scott J.H.J., Joy D.C., *fourth edition*, Springer- Verlag Berlin Heidelberg **2018**, p. 9-211.

[14] Handbook of sample preparation for scanning electron microscopy and x-ray microanalysis, Echlin P., *first edition*, Springer US **2009**, p.87.

[15] Constitution of binary alloys, Hansen M., *second edition*, McGraw- Hill Education **1958**, p. 609-634.

[16] Technologie der Werkstoffe, Ruge J., Wohlfahrt H., *9. Auflage*, Springer Vieweg **2013**, p.76-77.

[17] Deutsches Kupferinstitut Auskunfts- und Beratungsstelle für die Verwendung von Kupfer und Kupferlegierungen, Kupfer-Zinn Knetlegierungen (Zinnbronzen), *Auflage 7*, **2004,** p.4.

[18] Periodic Table of Elements and X-ray Energies, Bruker, [cited: June 13, 2018], www.bruker.com/hhxrf.